이학박사학위논문

Effects of In-Cloud Turbulence on Clouds and Precipitation

구름 내 난류가 구름과 강수에 미치는 영향

2016년 2월

서울대학교 대학원

지구환경과학부

이 현 호

Effects of In-Cloud Turbulence on Clouds and Precipitation

By
Hyunho Lee

A Dissertation Submitted to the Faculty of the Graduate School of Seoul National University in Partial Fulfillment of the Requirements for the Degree of Doctor of Philosophy

February 2016

Advisory Committee:
Professor In-Sik Kang, Chair
Professor Jong-Jin Baik, Advisor
Professor Yign Noh
Professor Song-You Hong
Professor Seok-Woo Son

ABSTRACT

During the recent decades, it has been known that in-cloud turbulence has significant impacts on the cloud development and precipitation, especially on the collision between cloud particles. The effects of turbulence-induced collision enhancement (TICE) on warm clouds and precipitation are investigated by changing the cloud condensation nuclei (CCN) concentration using a two-dimensional dynamic model with bin microphysics. TICE is determined according to the Taylor microscale Reynolds number and the turbulent dissipation rate. The thermodynamic sounding used in this study is characterized by a warm and humid atmosphere with a capping inversion layer, which is suitable for simulating warm clouds. For all CCN concentrations, TICE slightly reduces the liquid water path during the early stage of cloud development and accelerates the onset of surface precipitation. However, changes in the rainwater path and in the amount of surface precipitation that are caused by TICE depend on the CCN concentrations. For high CCN concentrations, the mean cloud drop number concentration (CDNC) decreases and the mean effective radius increases due to TICE. These changes cause an increase in the amount of surface precipitation. However, for low CCN concentrations, changes in the mean CDNC and in the mean effective radius induced by TICE are small and the amount of surface precipitation decreases slightly due to TICE. A decrease in condensation due to the accelerated coalescence between droplets explains the surface precipitation decrease. In addition, an increase in the CCN concentration can lead to an increase in the

amount of surface precipitation and TICE affects the relationship between the CCN concentration and the amount of surface precipitation. It is shown that these results depend on the atmospheric relative humidity.

The effects of TICE on mixed-phase deep convective clouds are numerically investigated using the 2-D cloud model with bin microphysics that considers TICE for drop-drop collisions and drop-ice collisions. Two basic-state wind profiles and two aerosol concentrations are considered. In all simulation cases, graupel particles account for the most part of the clouds. In the uniform basic-state wind cases, graupel particles with moderate sizes occupy some portion of graupel mass in the cases with TICE, whereas graupel particles with large sizes occupy a significant portion of graupel mass in the cases without TICE. This is because the growth of ice crystals into small graupel particles is enhanced due to TICE. The changes in the size distributions of graupel particles by TICE result in a decrease in the mass-averaged mean terminal velocity of graupel particles. Therefore, the downward flux of graupel mass, and thus the melting of graupel particles, is reduced by TICE, leading to a decrease in the amount of surface precipitation. Moreover, under the low aerosol concentration, TICE increases the sublimation of ice particles, consequently playing a partial role in reducing the amount of surface precipitation. The effects of TICE are less pronounced in the sheared basic-state wind cases than in the uniform basic-state wind cases because the number of ice crystals is much smaller than in the uniform basic-state wind cases. Thus, the size distributions of graupel particles in the cases with and without TICE show little difference.

Using the large-eddy simulation version of the Weather Research and

Forecasting (WRF) model coupled with the detailed bin microphysics scheme, the effects of TICE on the properties of precipitating warm clouds, such as surface precipitation, cloud fraction, cloud optical thickness, and cloud albedo, are investigated. As in previous studies, the enhanced droplet collision results in the increased mean drop size, which accelerates the onset of surface precipitation and increases the amount of surface precipitation. The initially unimodal drop size distribution becomes bimodal due to the turbulence effects, which is different from the aerosol effects that shift the peak position in the unimodal drop size distribution. Evaporation is reduced as the drop size increases, and the cloud fraction increases due to the decreased evaporation. Moreover, as the atmosphere becomes more stable due to the decreased evaporative cooling, the mean and variability of vertical motion decreases and the decrease results in a decrease in turbulent kinetic energy (TKE) by decreasing shear production of TKE. The decrease in TKE due to the TICE can be interpreted as a negative feedback, although the change is generally small. The increased mean drop size induces decreases in cloud optical thickness and cloud-averaged albedo, but these decreases are largely offset by the increased cloud fraction when considering the domain-averaged cloud albedo. Turbulence-induced differences in precipitation have relatively small effects on the cloud structures because of the small differences in precipitation or small precipitation amounts.

The effects of TICE on a heavy precipitation event that occurred on 21 September 2010 over the middle Korean Peninsula are examined using the WRF model coupled with the bin microphysics model. The numerical simulation captures well the important features of observed surface precipitation and radar

reflectivity, as well as synoptic conditions. The mean surface precipitation amount averaged over the middle Korean Peninsula increases due to TICE. In particular, the maximum surface precipitation rate in Seoul and its nearby area increases by up to 35% due to TICE, which is closer to the observation. The frequency of high radar reflectivity near the surface also becomes higher due to TICE. TICE accelerates the coalescence between small cloud droplets, which induces a decrease in condensation and an increase in water vapor transported upward following the front. This causes an increase in relative humidity with respect to ice at high altitudes, hence increasing the depositional growth of ice crystal and snow particles. Therefore, the snow mass increases due to TICE and this increase induces the increase in surface precipitation amount. The rimed fraction of snow is reduced by TICE because of the decreased small droplets aloft. However, the TICE-induced increase in ice mass via depositional growth causes an increase in riming. Peak radius in the snow size distribution is little changed, whereas the snow number concentration increases in almost the entire snow radius range.

A new autoconversion parameterization that considers TICE is developed based on the analytic integration and the collection efficiencies obtained by a particle model and a turbulence statistical model. The box model results show that the developed autoconversion parameterization improves the calculation accuracy of the process considerably, both for the time to convert cloud droplet to raindrop and the number concentration of cloud droplets. The developed autoconversion parameterization is implemented into the Thompson microphysics scheme and the WRF model and examined with an idealized deep convective cloud case and a realistic heavy precipitation case. In the idealized deep convective cloud case, the

number concentration of raindrops is much larger with the developed autoconversion parameterization than that with the traditional autoconversion parameterization, which causes a delay of the surface precipitation onset and a decrease in surface precipitation amount. In the real heavy precipitation case, the effects of developed autoconversion parameterization are limited. However, turbulence clearly increases the surface precipitation at the particular area of interest, which is because the turbulence accelerates the coalescence of small droplets and this accelerated growth of droplets decreases the condensation. More water vapor induced by this decrease in condensation is transported upward and increases the ice particle mixing ratio, hence increasing surface precipitation via melting.

Keywords: cloud microphysics, turbulence effects, bin microphysics model, clouds, precipitation, autoconversion process

Student Number: 2011-30119

CONTENTS

LIST OF FIGURES

LIST OF TABLES

1. Introduction

1.1. Review of previous studies

1.1.1. Effects of turbulence on collisions between cloud droplets

It is known that inside clouds are highly turbulent zones. Turbulence affects not only cloud microphysical processes, such as the collision process and the diffusional processes (condensation, evaporation, deposition, and sublimation), but also mixing and entrainment (Grabowski and Wang 2013 and references therein). However, due to the inherent complexity, the effects of turbulence on clouds and precipitation remain an unresolved problem in cloud physics. Observation techniques have not been sufficiently developed to identify the detailed spatio-temporal variability of in-cloud turbulence. It is also challenging to simulate interactions between clouds and turbulent flows in numerical models because turbulent motions have spatial scales as small as a few millimeters, so simulations that simultaneously consider both turbulent eddies and cloud systems require large computing resources. Therefore, attempts have been made to parameterize the effects of turbulence in numerical cloud models. Some recent reviews have provided the current status of this topic (e.g., Khain et al. 2007; Devenish et al. 2012; Grabowski and Wang 2013).

It is known that turbulence substantially enhances the collisions of cloud particles. After the Arenberg's trailblazing work (Arenberg 1939), numerous studies have been tried to investigate the effects of turbulence on the collisions of

cloud particles. Saffman and Turner (1956) developed a theoretical formulation for the enhanced relative motion by turbulence on collision rates, applicable to weak-inertia droplets. Reuter et al. (1988) introduced a stochastic model and showed that turbulent fluctuations could enhance the geometric collision kernel. Over the past decades, an increasing number of studies have been reported in both the engineering and atmospheric field concerning the collision rate of inertial particles in a turbulent flow using very accurate numerical models.

Direct numerical simulation (e.g., Zhou et al. 2001; Franklin et al. 2005; Ayala et al. 2008; Wang and Grabowski 2009) and simulations using turbulent statistical models (e.g., Pinsky et al. 2008) have shown that turbulence increases the collision rate between drops by a few times compared with the collision rate when only considering gravitational collection, which can result in accelerated and increased surface precipitation. By solving the stochastic collection equation, Franklin (2008) demonstrated that turbulence substantially affects the evolution of the drop size distribution and can shorten the time required for raindrop formation. Riechelmann et al. (2012) developed a new Lagrangian warm cloud model coupled with an LES model and showed that droplets grow more quickly when the effects of turbulence are included.

While previous studies have focused on the effects of turbulence on warm clouds, few studies have examined the effects of turbulence on ice particles because of the complexity of these particles. Some studies have shown that turbulence also enhances the rate of collision including ice particles, especially the riming rate (Pinsky and Khain, 1998; Pinsky et al., 1998). Because precipitation from the melting of ice particles is dominant in mixed-phase clouds, the collision

enhancement with respect to ice particles would be important when the cloud development and precipitation in mixed-phase clouds are tried to be investigated.

1.1.2. Effects of turbulence on clouds and precipitation

In contrast to a relative long history of investigating the effects of turbulence on the collisions of cloud particles, few studies have been focused on how such enhanced collisions affect the cloud development and precipitation. Using a large-eddy simulation (LES) model with bulk cloud microphysics, Seifert et al. (2010) showed that turbulence leads to a substantial enhancement in surface precipitation in warm clouds. Wyszogrodzki et al. (2013), followed by Grabowski et al. (2015), examined the effects of turbulence-induced collision enhancement under a specific range of aerosol concentrations in warm clouds using an LES model with bin microphysics and showed an increase in surface precipitation due to turbulence effects. Lee et al. (2014) also showed that precipitation starts earlier and the amount of surface precipitation increases due to turbulence-induce collision enhancement using an LES model with Lagrangian cloud model. These numerical studies suggest that in-cloud turbulence plays important roles in clouds and precipitation.

Compared with the effects of turbulence on warm clouds, the effects of turbulence on mixed-phase clouds have been less focused and start later. Using a 2-D cloud model with bin microphysics, Benmoshe et al. (2012) and Benmoshe and Khain (2014) investigated the effects of turbulence on mixed-phase deep convective clouds with varying aerosol concentrations. Benmoshe et al. (2012) showed that the effects of turbulence decrease surface precipitation and are

somewhat opposite to the effects of aerosol particles: turbulence-induced collision enhancement accelerates the formation of the first raindrops while leading to a decrease in the net amount of accumulated surface precipitation in mixed-phase clouds. However, Benmoshe and Khain (2014) shows that the effects of turbulence on macrophysical properties of the mixed-phase clouds are comparatively small.

1.2. Aim of this study

The fundamental aim of this study is to examine the effects of turbulence on clouds and precipitation with various environmental conditions and cloud types. At first, this study aims to investigate whether the effects of turbulence on clouds and precipitation differ as the aerosol concentration varies, focusing on a single warm cloud (Section 3). For the purpose, this study adopts the 2-D cloud model with bin microphysics that was used in Benmoshe et al. (2012) and Benmoshe and Khain (2014).

After then, this study aims to examine the effects of turbulence-induced collision enhancement on mixed-phase deep convective clouds under different basic-state winds and aerosol concentrations (Section 4). The two factors (basic-state wind and aerosol concentration) are known to affect the development of deep convective clouds (e.g., Weisman and Klemp 1982; Fan et al. 2009; Han et al. 2012).

As the extension of the studies on the idealized environmental conditions, the effects of turbulence on more realistic environmental conditions are investigated (Section 5 and 6). For the purpose, a mesoscale numerical weather

model coupled with the bin microphysics scheme is used. With the model, the effects of turbulence on clouds and precipitation are investigated considering more realistic conditions and more complex atmospheric physical processes. This examination is expected to provide a better understanding of cloud-aerosol interactions and the effects of turbulence on clouds and precipitation.

Because the bin microphysics model needs huge computing resources, it is required to include the turbulence effects into the bulk microphysics model. For the purpose, a newly developed autoconversion parameterization based on the elaborate particle model results and analytic calculation is proposed and validated (Section 7). Moreover, the turbulence effects on the autoconversion process is included in the developed parameterization and examined for an idealized deep convective cloud and a realistic heavy precipitation case.

2. Model descriptions

The numerical model mainly used in this study is HUCM (Hebrew University Cloud Model). A detailed description is provided by Khain and Sednev (1996), Khain et al. (2000, 2004, 2008, 2011).

2.1. Dynamic process

HUCM adopts a two-dimensional anelastic, nonhydrostatic frame to solve a dynamic equation system. This model solves a vorticity equation which combines the equations of the perturbation wind velocities u and w with the continuity equation, which is derived as:

$$\begin{aligned}&\frac{\partial \overline{\rho}_a \eta}{\partial t} + \frac{\partial \overline{\rho}_a U \eta}{\partial x} + \frac{\partial \overline{\rho}_a W \eta}{\partial z} = \\ &\quad \overline{\rho}_a^2 g \left(\frac{1}{\theta_0} \frac{\partial \theta}{\partial x} + 0.608 \frac{\partial q_v}{\partial x} - \frac{\partial q_h}{\partial x} \right) \\ &\quad + 2w \frac{\partial \overline{\rho}_a}{\partial z} \left(\eta + u \frac{\partial \overline{\rho}_a}{\partial z} \right) - \overline{\rho}_a uw \frac{\partial^2 \overline{\rho}_a}{\partial z^2} + D(\eta),\end{aligned} \tag{2.1}$$

where $\overline{\rho}_a$ is the reference density of air depending only on the height, η is the vorticity, U and W are the total wind velocities of x and z direction, respectively, θ is the potential temperature, θ_0 is 300 K, g is the gravitational constant, q_v is the mixing ratio of vapor, and q_h is the mixing ratio of hydrometeors. From the

calculated vorticity, the perturbation wind velocities u and w are calculated as:

$$\nabla^2\psi = \eta, \tag{2.2}$$

$$u = -\frac{1}{\bar{\rho}_a}\frac{\partial\psi}{\partial z}, \tag{2.3}$$

$$w = \frac{1}{\bar{\rho}_a}\frac{\partial\psi}{\partial x}, \tag{2.4}$$

where ψ is the stream function.

In Eq. (2.1), $D(\eta)$ corresponds to the diffusion. It is represented by

$$D(\eta) = \bar{\rho}_a\left[\frac{\partial}{\partial x}\left(K_h\frac{\partial\eta}{\partial x}\right)+\frac{\partial}{\partial z}\left(K_h\frac{\partial\eta}{\partial z}\right)\right], \tag{2.5}$$

where K_h is the diffusion coefficient, which is calculated using the turbulent kinetic energy (TKE) k,

$$\frac{dk}{dt} = K_h\left[2\left(\frac{\partial U}{\partial x}\right)^2+2\left(\frac{\partial W}{\partial z}\right)^2+\left(\frac{\partial U}{\partial z}+\frac{\partial W}{\partial x}\right)^2-\frac{1}{\mathrm{Pr}}\frac{g}{\theta_0}\frac{\partial\theta}{\partial z}\right]-\varepsilon, \tag{2.6}$$

$$K_h = C_k l k^{1/2}, \tag{2.7}$$

$$\varepsilon = \frac{Ck^{3/2}}{l}, \tag{2.8}$$

$$l = \begin{cases} \sqrt{\Delta x \Delta z} & \text{if } N^2 \le 0 \\ \min\left(\sqrt{\Delta x \Delta z}, 0.76 \dfrac{\sqrt{k}}{N} \right) & \text{if } N^2 > 0 \end{cases}, \tag{2.9}$$

$$C = 1.9 C_k + \frac{(0.93 - 1.9 C_k) l}{\sqrt{\Delta x \Delta z}}, \tag{2.10}$$

where ε is the turbulent dissipation rate, Δx and Δz are the grid sizes of x and z direction, respectively, and l is the mixing length. The Prandtl Number Pr and the Smagorinski constant C_k is set to 3 and 0.2, respectively. N is the Brunt-Väisälä frequency.

To calculate the advection terms in Eq. (2.1), the Arakawa method (Arakawa 1966) is used.

2.2. Microphysical process

HUCM uses a bin microphysics to represent the hydrometeor and aerosol size distributions. The model considers seven hydrometeor types [liquid water, three types of ice crystals (column, plate, and dendrite), snow, graupel, and hail]. To treat the size distribution of each hydrometeor type, the model uses 43 mass-doubling bins. The smallest hydrometeor mass considered in the model is 3.351×10^{-14} kg, which corresponds to the drop mass whose radius is 2 μm. For aerosol, the largest aerosol radius considered in the model is equal to the smallest drop radius. The model take the nucleation, condensation, evaporation, deposition, sublimation, freezing, melting, collision, and breakup process into account. The liquid fraction of snow, graupel, and hail is calculated at every model grid point

and at every time step so that the time-dependent melting rates can be calculated more precisely. The rimed fraction of snow is calculated to estimate the density and terminal velocity of snow particles more precisely. The density and terminal velocity of a cloud particle depend on its radius, type, liquid fraction, and rimed fraction. Detailed descriptions of the model are provided in Khain et al. (2011).

2.2.1. Nucleation process

To calculate the nucleation of cloud droplets, the Köhler equation (Köhler 1936) is used. For a given ambient supersaturation with respect to water S_w, the critical aerosol radius r_N is calculated as:

$$r_N = \frac{a}{3}\left(\frac{4}{bS_w^2}\right)^{1/3}, \tag{2.11}$$

where a is a temperature-dependent coefficient that is related to the curvature effect, and b is a constant that is related to the solution effect. For a given S_w, all aerosol particles that have the radii larger than r_N are activated. It is assumed that if an aerosol particle has the radius less than 0.4 μm, the radius of activated droplet is 2 μm; if an aerosol particle has the radius larger than 0.4 mm, the radius of activated droplet is the five times of the aerosol particle (Khain 2000).

For the ice nucleation, among several processes, only deposition process proposed by Meyer et al. (1992) is considered. The number of ice nuclei is

$$N_i = N_{i0}\exp(a + bS_i), \tag{2.12}$$

where N_i is the number of ice nuclei, S_i is the supersaturation with respect to ice, $N_{i0} = 10^3$ m^{-3}, $a = -0.639$, and $b = 12.96$. The ice nucleation process is deactivated when the air temperature is lower than –45℃. The supersaturation in Eq. (2.12) is limited to be smaller than 30%. The number of newly activated ice particles is calculated by the Lagrangian expression of Eq. (2.12):

$$dN_i = \begin{cases} bN_i dS_i & \text{if } dS_i > 0 \\ 0 & \text{if } dS_i \le 0 \end{cases}, \tag{2.13}$$

where dS_i is calculated as:

$$dS_i = \left(\frac{\partial S_i}{\partial t} + U \frac{\partial S_i}{\partial x} + W \frac{\partial S_i}{\partial z} \right) dt, \tag{2.14}$$

The shape of ice nuclei is determined according to the temperature, following Takahashi et al. (1991), is shown in Fig. 2.1.

2.2.2. Diffusional process

All vapor diffusional processes (condensation, evaporation, deposition, and sublimation) are calculated using the following expression, which is obtained from the vapor diffusion equation and by ignoring the curvature effect and the solution effect:

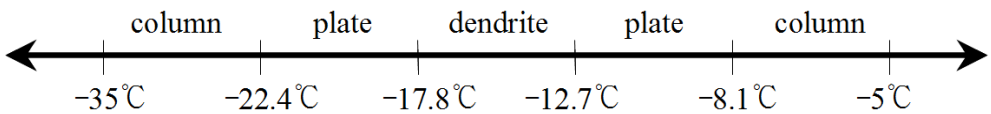

Figure 2.1 The shapes of ice crystals with respect to the air temperature. (From Takahashi et al. 1991)

$$\frac{dm}{dt} = \frac{4\pi CSv_f}{F_d + F_k}, \tag{2.15}$$

where m is the mass of the particle, C is the capacitance of the particle, v_f is the ventilation coefficient of vapor depending on the Reynolds number, and F_d and F_k are coefficients that are related to the vapor diffusivity and air thermal conductivity, respectively. If a particle is water, the capacitance of the particle is the same as its radius. Therefore, Eq. (2.15) can be integrated exactly, which is expressed as:

$$m' = \left(m^{2/3} + \frac{2}{3} \frac{4\pi r v_f}{F_d + F_k} \frac{Sdt}{m^{1/3}} \right)^{3/2}, \tag{2.16}$$

where m' is the particle mass after dt.

If the particle mass is changed by the vapor diffusion, the number of the corresponding particle should be redistributed due to the fixed mass bin in the model. Khain et al. (2008) proposed a new remapping method to conserve additional moments of the particle size distribution and the method is adopted in the model. Moreover, a very small time step (less than 1 s) is generally required to integrate Eq. (2.15) because the supersaturation shows a high variability during the vapor diffusional processes. A new method to calculate the changed particle mass with relatively longer time step was proposed in Khain et al. (2008) and is used in the model.

2.2.3. Freezing process

Two types of freezing are considered. One was proposed by Vali (1975), which provides the number of ice particles as a function of air temperature. This method is applied when temperature is higher than –30℃. It has the form as:

$$N_f = N_{f0}\left[0.1\left(T_0 - T\right)^{\gamma}\right], \tag{2.17}$$

where N_f is the number of freezing particles, N_{f0} = 1.0^7 m^{-3}, T is the air temperature, γ = 4.4, T_0 = 0℃. Eq. (2.17) is converted using the Lagrangian expression, similar with Eq. (2.12),

$$dN_f = \begin{cases} -0.1\gamma N_{f0}\left(T_0 - T\right)^{\gamma-1} dT & \text{if } dT < 0 \\ 0 & \text{if } dT \geq 0 \end{cases}, \tag{2.18}$$

The derivative of temperature is calculated and applied to calculate the number of newly freezing drops, which is the similar with Eq. (2.14).

When the temperature is lower than –30℃, the stochastic freezing, which was proposed by Biggs (1953), is applied. The probability of freezing P_f is

$$P_f = 1 - \exp\{-ma\exp[-b(T - T_0)dt]\}, \tag{2.19}$$

where a = 0.1 and b = 0.66. If the temperature is less than –38℃, P_f is closed to 1 regardless of the mass of drop. Therefore, all drops are assumed to freeze

simultaneously. If the mass of drop is less than 2×10^{-9} kg, the hydrometeor type of the freezing particle is set to be column; otherwise, hail.

2.2.4. Melting process

Gradual time-dependent melting, which was proposed by Phllips et al. (2007), is adopted in the model. The liquid water fraction of an ice particle increases by the melting. The change in the liquid water fraction by the melting for ice crystals and snow is provided as:

$$\frac{dm_l}{dt} = -\left(\frac{4\pi C v_f}{L_m}\right)\left[k_a(T-T_0)+\left(\frac{D_v L_e}{R_v}\right)\left(\frac{e}{T}-\frac{e_{sw}(T_0)}{T_0}\right)\right], \qquad (2.20)$$

where m_l is the liquid mass of the ice particle, L_m is the latent heat release rate by melting, k_a is the thermal conductivity of air, T_0 is the surface temperature of the ice particle (assumed to be 0℃), D_v is the diffusivity of vapor, L_e is the latent heat release rate by evaporation, R_v is the gas constant for vapor, e is the vapor pressure, and $e_{sw}(T_0)$ is the saturation vapor pressure with respect to water at T_0. For graupel and hail, the change in the liquid water fraction by the melting is provided as:

$$\frac{dm_m}{dt} = -\left(\frac{4\pi C v_f}{L_m}\right)\left[k_a\left(T-T_0\right)\frac{v_h}{v_f}+\left(\frac{D_v L_e}{R_v}\right)\left(\frac{e}{T}-\frac{e_{sw}(T_0)}{T_0}\right)\right], \qquad (2.21)$$

where v_h is the ventilation coefficient of heat. The impacts of this gradual melting on the cloud development and precipitation were exhibited in Phllips et al. (2007).

2.2.5. Collision process

Collisions of cloud particles are calculated using a stochastic collision equation (e.g., Pruppacher and Klett 1997), which has the form as:

$$\frac{df(m)}{dt} = \int_0^{m/2} f(m-m')K(m',m-m')f(m')dm' - \int_0^{\infty} f(m)K(m,m')f(m')dm', \tag{2.22}$$

where $f(m)$ is the size distribution function of hydrometeors and K is the collision kernel, which is expressed by

$$K(m,m') = \pi(r+r')^2 \left|V - V'\right| \eta, \tag{2.23}$$

where r and r' are the radii of cloud particles whose masses are m and m', respectively, V and V' are the terminal velocities of cloud particles whose radii are r and r', respectively, and η is the collision efficiency including hydrodynamic collection efficiency, coalescence efficiency, and turbulence-induced collision enhancement factor. Moreover, it is known that the collision efficiencies depend on the pressure (Pinsky et al. 2001). Therefore, the collision kernels on three different pressure levels (1000, 750, 500 hPa for water-water collision and 750, 500, 300 hPa otherwise) are included in the model and calculated at every grid point and every time step via interpolation.

After the collisions in the bin microphysics model, a remapping algorithm

is needed, which is similar with the vapor diffusional processes. If cloud particles whose masses are m_i and m_j collide, the resultant particles are distributed in the k^{th} bin where k is determined by

$$m_k \le m_i + m_j < m_{k+1}, \tag{2.24}$$

Moreover, partitioning of the increased size distribution is determined by assuming the size distribution function has the form of an exponential function. Detailed calculation of the partitioning was described in Bott (2000).

There are some uncertainties on the type determination of the created particles after the collisions. In the model, the following rules are applied to determine the types of the created particles. Note that collisions including ice crystals are allowed only $T < 0$℃.

a. water-water : water

b. water-ice crystal : graupel ($m_{\text{water}} > m_{\text{ice crystal}}$),
ice crystal ($m_{\text{water}} < m_{\text{ice crystal}}$)

c. water-snow : graupel ($m_{\text{water}} > m_{\text{snow}}$), snow ($m_{\text{water}} < m_{\text{snow}}$)

d. water-graupel : graupel

e. water-hail : hail

f. ice crystal-ice crystal : snow

g. ice crystal-snow : snow

h. snow-snow : snow

i. snow-graupel : snow ($m_{\text{snow}} > m_{\text{graupel}}$), graupel ($m_{\text{snow}} < m_{\text{graupel}}$)

2.3. Turbulence-induced collision enhancement

The equation of motion for a drop in a turbulent flow can be written as follows (Pinsky et al. 2006):

$$\frac{d\mathbf{v}}{dt} = -\frac{1}{\tau}\left(\mathbf{v} - \mathbf{W}\right) + g\mathbf{k}, \tag{2.25}$$

where **v** is the drop velocity, τ is the characteristic relaxation time of the drop that is related with the terminal velocity V_t as $V_t = g\tau$, **k** is the unit vector directed downward, and **W** is the flow velocity. By defining the relative drop velocity **u** = **v** – **W** – g**k**, Eq. (2.25) can be rewritten as:

$$\frac{d\mathbf{u}}{dt} = -\frac{1}{\tau}\mathbf{u} - \left[\mathbf{A} + \left(\mathbf{u}\cdot\nabla\right)\mathbf{W} + V_t\frac{\partial \mathbf{W}}{\partial z}\right], \tag{2.26}$$

where **A** is the Lagrangian acceleration of the flow that is expressed by $\mathbf{A} = \partial\mathbf{W}/\partial t + \mathbf{W}\cdot\nabla\mathbf{W}$. Eq. (2.26) can be rewritten using the tensor notation:

$$\frac{du_i}{dt} = -u_j\left(\frac{1}{\tau}\delta_{ij} + S_{ij}\right) - \left(A_i + V_t S_{i3}\right), \tag{2.27}$$

where δ_{ij} is the kronecker delta and S_{ij} is the turbulent shear $\partial W_i/\partial x_j$. Therefore, the equation of motion for the drop can be determined by the statistics of the Lagrangian acceleration of the flow and the turbulent shear. For the Lagrangian

acceleration of the flow, according to La Porta et al. (2001), the probability density function of the Lagrangian acceleration normalized by its standard deviation a^* is approximated at the high Taylor microscale Reynolds number Re_λ by the following function:

$$P_A(a^*) = C\exp\left[-\frac{a^{*2}}{s^2\left(1+\beta\left|a^*\right|^r\right)}\right], \tag{2.26}$$

where C = 0.7854, γ = 1.588, s = 0.508, and β = 1.099. Moreover, the variance of the Lagrangian acceleration tends to be the value,

$$\sigma^2 = a_0\varepsilon^{3/2}\nu^{-1/2}, \tag{2.27}$$

where ε is the turbulent dissipation rate, ν is the kinematic air viscosity. The constant a_0 was set to be 1 in Monin and Yaglom (1975). However, it is known to increase as Re_λ increases. Hill (2002) presented the result that a_0 can be expressed as a function of Re_λ:

$$a_0 = \frac{1}{3}\left(2.5\mathrm{Re}_\lambda^{0.25} + 0.08\mathrm{Re}_\lambda^{0.11}\right). \tag{2.28}$$

The series of the Lagrangian acceleration of the flow A_k is generated as:

$$\eta_k = \int_{-\infty}^{A_k} P_A(u)du, \tag{2.29}$$

where η_k is random numbers uniformly distributed within the interval [0,1].

The series of nine components of turbulent shear is also generated using the similar method with that of the Lagrangian acceleration of the flow. For the turbulent shear, a four-parameric Pearson probability density function is used:

$$P_S(S) = C\left|b_0 + 2b_1 S + b_2 S^2\right|^{1/2b_2} \exp\left(\frac{a_0 - b_1/b_2}{\sqrt{b_0 b_2 - b_1^2}} \arctan\frac{b_1 + b_2 S}{\sqrt{b_0 b_2 - b_1^2}}\right), \tag{2.30}$$

where

$$a_0 = \frac{1}{2}\frac{Sk(Fl+3)}{5Fl - 9 - 6Sk^2}, \tag{2.31}$$

$$b_0 = -\frac{1}{2}\frac{4Fl - 3Sk^2}{5Fl - 9 - 6Sk^2}, \tag{2.32}$$

$$b_1 = -\frac{1}{2}a_0, \tag{2.33}$$

$$b_2 = -\frac{1}{2}\frac{2Fl - 3Sk^2 - 6}{5Fl - 9 - 6Sk^2}, \tag{2.34}$$

and the skewness *Sk* and the flatness *Fl* are obtained experimentally as:

$$Sk = -0.27\,\mathrm{Re}_{\lambda}^{0.11}, \tag{2.35}$$

$$Fl = 1.33\,\mathrm{Re}_{\lambda}^{0.32}. \tag{2.36}$$

Therefore, by considering Eqs. (2.26) – (2.36), calculating collision efficiency is reduced to calculate Re_{λ} and ε for a given turbulent flow. (Pinsky et al. 2004, 2006).

Re_{λ} is defined as (Frisch 1995):

$$\mathrm{Re}_{\lambda} \equiv \frac{u_{rms}\lambda}{\nu}, \tag{2.37}$$

where u_{rms} is the root-mean-square velocity fluctuation, and λ is the Taylor microscale length scale calculated as (Monin and Yaglom 1975):

$$\lambda = u_{rms}\sqrt{\frac{15\nu}{\varepsilon}}, \tag{2.38}$$

The root-mean-square velocity fluctuation is calculated as (Frisch 1995)

$$u_{rms} = \sqrt{\frac{2}{3}E_{tot}}, \tag{2.39}$$

where E_{tot} is the total turbulent kinetic energy of the flow which does not depend on grid size. E_{tot} is defined as (Pope 2000)

$$E_{tot} = (\varepsilon L)^{2/3} \tag{2.40}$$

where L is the external turbulence scale. Therefore, we need to evaluate L to determine the Taylor microscale Reynolds number. In the model, L is determined as $L = L_{cl} / 15$, where L_{cl} is the linear cloud size which is calculated as $L_{cl} = S_{cl}^{1/2}$; S_{cl} is the cloud area in which the total hydrometeor mass content exceeds a threshold value. The method applied in the model differs from those were used by previous studies (Franklin 2008; Seifert et al. 2010). However, simulation results shows that the orders of the magnitudes of ε and Re_{λ} are close each other (Benmoshe et al. 2012).

2.4. The Weather Research and Forecasting (WRF) model

For cloud simulations in large eddy simulations (LES) or realistic environmental conditions, the Weather Research and Forecasting (WRF) model is incorporated in this study. The WRF model provides both idealized and realistic numerical experiment conditions. A detailed description is provided in Skamarock et al. (2008). In this study, the WRF model v3.6.1 coupled with HUCM is used.

The LES version of the WRF model is used to simulate idealized warm clouds and precipitation in Section 5. Only the warm microphysics part of HUCM is implemented into the WRF model. So the prognostic variables are the drop and aerosol number concentrations of each bin, and the condensation, evaporation, collision, breakup, and sedimentation processes are considered.

The WRF model with realistic environmental conditions is used to simulate a heavy precipitation case in Section 6. For the initial and boundary atmospheric conditions, National Centers for Environmental Prediction (NCEP) Final (FNL) analysis data with 1°×1° spatial resolution and 6-h interval are used. In addition to the warm microphysics part of HUCM, the ice microphysics part is also implemented into the WRF model. The added prognostic variables are the plate-, column-, and dendrite-shape ice crystals, snow, graupel, and hail number concentration of each bin. Also, deposition, sublimation, freezing, melting, and ice multiplication processes are considered.

More on the number concentration of each bin of each hydrometeor, this full microphysics scheme predicts the rimed fraction of snow and the liquid water fractions of snow, graupel, and hail. It is regarded that a snow particle consists of aggregated, rimed, and liquid parts and that the increased mass due to collection with a supercooled drop is regarded as rimed mass. The rimed fraction of snow (the ratio of rimed mass to the total mass of a snow particle) is used to update the density and terminal velocity of snow particles at every time step and every grid point (Khain et al. 2011), assuming that the rimed part of the snow particle has the same properties as those of a hail particle. The liquid water fractions of snow, graupel, and hail are used to calculate a time-dependent gradual melting process (Phillips et al. 2007), which replaces a classical melting process that allows all ice particles to be melted all at once at the freezing level. The effects of liquid water fractions were discussed in Phillips et al. (2007) and Iguchi et al. (2014).

3. Effects of turbulence on warm clouds and precipitation

3.1. Experimental setup

The thermodynamic sounding used by Ogura and Takahashi (1973) is adopted to simulate a single warm shallow cloud (Fig. 3.1). One important feature of this sounding is the existence of a strong inversion layer between z = 3 and z = 3.4 km, which prevents the growth of clouds above this layer. Another important characteristic is a humid atmosphere compared to that of previous studies (e.g., Xue et al., 2008; vanZanten et al., 2011). The water vapor mixing ratio at the surface is 17.4 g kg^{-1}, and the water vapor mixing ratio averaged over the lowest 1 km is 14.8 g kg^{-1}. The horizontal wind speed is set to zero at the surface and increases linearly with height to 5 m s^{-1} at z = 4 km. The wind speed remains constant above 4 km. The temperature at the bottom of the inversion layer is 5.3℃ (Fig. 3.1); thus, only warm clouds are simulated in this study.

It is assumed that all aerosols can serve as cloud condensation nuclei (CCN) according to their radii and the ambient supersaturation. The aerosol concentration is constant below z = 2 km and decreases exponentially with height above 2 km; the e-folding depth is 2 km. Following Khain et al. (2000), the aerosol size distribution $N(r_a)$ is formulated using the Köhler equation (Köhler, 1936; Pruppacher and Klett, 1997) and the Twomey equation (Twomey, 1959), which is given by

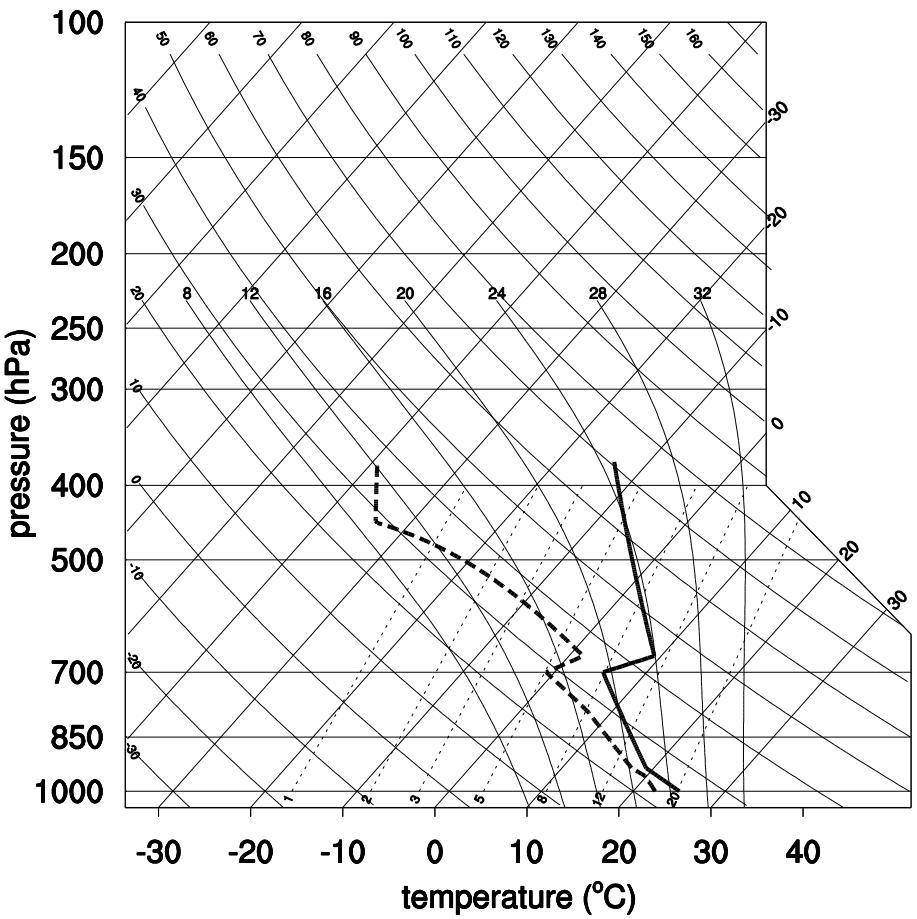

Figure 3.1 Thermodynamic sounding used in this study, which is adopted from Ogura and Takahashi (1973). Thick solid and dashed lines indicate the air temperature and dew point temperature, respectively.

$$\frac{dN}{d\ln r_a} = \frac{3}{2} N_0 k \left(\frac{4A^3}{27Br_a^3} \right)^{k/2}, \qquad (3.1)$$

where r_a is the aerosol particle radius, N_0 is he CCN concentration at 1% supersaturation, k is a constant, A is a temperature-dependent coefficient that is related to the curvature effect, and B is a constant that is related to the solution effect. The value of k is specified as 0.5. The numerical experiments are performed for aerosol concentrations of N_0 = 30, 100, 300, 1000, and 3000 cm^{-3}.

The domain size is 51.2 km in the horizontal and 8 km in the vertical. A damping layer is included from z = 5 km to the top of the model domain. The horizontal and vertical grid spacing is 50 m. The time step is 1 s except for the diffusional processes (0.1 s). The integration time is 2 h. Convection is initiated using a specified low-level heating of 0.1 K s^{-1} for the first 100 s of the simulations. Additional numerical experiments are performed by varying the intensity of the initial heating rate to obtain an ensemble. Although the number of numerical experiments is small, the results (not shown) show that the overall structures of the simulated clouds are not substantially altered due to changes in the low-level heating. Therefore, only the results from the reference heating intensity (0.1 K s^{-1}) are shown in the following sections.

3.2. Macroscopic structures

Figure 3.2 depicts the liquid water path (LWP, calculated using both cloud droplets and raindrops), rainwater path (RWP), surface precipitation rate, and the amount of accumulated surface precipitation time series for N_0 = 30, 100, 300,

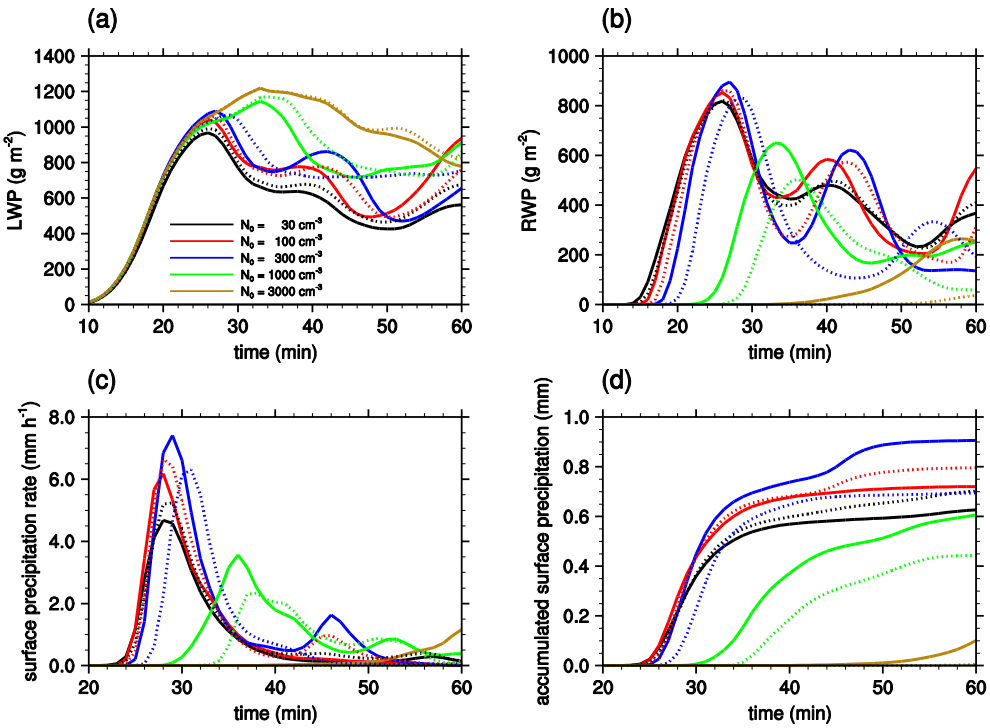

Figure 3.2 (a) Liquid water path (LWP) (g m^{-2}), (b) rainwater path (RWP) (g m^{-2}), (c) surface precipitation rate (mm h^{-1}), and (d) the amount of accumulated surface precipitation (mm) time series averaged over x = 13–23 km for N_0 = 30, 100, 300, 1000, and 3000 cm^{-3}. Solid and dashed lines correspond to the cases with and without TICE, respectively.

1000, and 3000 cm^{-3} with and without TICE. Because all liquid drops are represented in one hydrometeor category in the model, drops with a radius smaller than 0.1 mm are considered to be cloud droplets; larger drops are considered to be raindrops. The LWP, RWP, surface precipitation rate, and the amount of accumulated surface precipitation are averaged over x = 13–23 km, which encompasses the simulated cloud in each simulation. Although the model is integrated for 2 h, only the growth and decay of the initial clouds are foci of this analysis; clouds that appear after the decaying of the initial cloud are excluded in the analysis.

The LWP time series demonstrates that TICE and changes in the CCN concentration alter the LWP after approximately 20 min. An increase in CCN concentration tends to increase the LWP. Although the difference in the LWP induced by TICE is generally less than that induced by changes in the CCN concentration, TICE tends to decrease the LWP during the early stage of cloud development. One reason for this LWP decrease is that TICE enhances coalescence between small droplets, which accelerates the formation of large drops, ultimately increasing the fallout of drops. Another reason for this LWP decrease is that the enhanced coalescence between small droplets reduces the bulk condensation due to the reduced sum of the drop radii.

The RWP and surface precipitation rate exhibit more variance than the LWP with respect to changes in the CCN concentration and TICE (Figs. 3.2b–3.2d). A few previous studies have shown that the RWP and surface precipitation rate are more sensitive than the LWP to model configurations and environmental conditions (e.g., Arabas and Shima, 2013). TICE produces an earlier onset of

raindrop formation and surface precipitation. The effect of TICE on the onset of surface precipitation becomes larger as the CCN concentration increases. Specifically, the onset of surface precipitation is accelerated by 1 min for N_0 = 30 cm^{-3} and 17 min for N_0 = 3000 cm^{-3}. The CCN concentration is also known to affect the onset of surface precipitation (e.g., Albrecht, 1989; Han et al., 2012). In this study, surface precipitation begins 19 min earlier for N_0 = 30 cm^{-3} than for N_0 = 3000 cm^{-3} in the cases that include TICE. Under the conditions considered in this study, the acceleration in the onset of surface precipitation due to TICE (17 min) is comparable to the acceleration caused by a decrease in the CCN concentration (19 min).

Interestingly, TICE causes an increase in the RWP and the amount of surface precipitation only when $N_0 \geq 300$ cm^{-3}. Previous studies have shown that TICE always increases the amount of surface precipitation in warm clouds, i.e., even for $N_0 < 300$ cm^{-3}, due to the accelerated collisions between small droplets (e.g., Seifert et al., 2010; Wyszogrodzki et al., 2013). However, in this study, the effect of TICE on the amount of accumulated surface precipitation depends on the CCN concentration, which differs from the results of previous studies. When N_0 = 3000 cm^{-3}, an average of 0.2 mm and 0.05 mm of surface precipitation falls over the first hour of the simulations in the cases with and without TICE, respectively. However, when N_0 = 30 cm^{-3}, TICE decreases the amount of surface precipitation by 11%. This decrease for N_0 = 30 cm^{-3} is small compared with the increase for N_0 = 3000 cm^{-3} (a factor of four). The mechanism that causes these differences is examined in a later section.

3.3. Microscopic structures

The vertical distribution of the mean effective radius r_e, which is defined as

$$r_e = \frac{\int_0^\infty r^3 f(r) dr}{\int_0^\infty r^2 f(r) dr}, \tag{3.2}$$

where r is the drop radius and $f(r)$ is the drop size distribution, is presented in Fig. 3.3. In the following analysis, only grid points at which the cloud drop number concentration (CDNC) ≥ 20 cm^{-3} (except for N_0 = 30 cm^{-3}, in which CDNC ≥ 15 cm^{-3}) are used for averaging (e.g., Benmoshe et al., 2012; Arabas and Shima, 2013). Although several studies have used only small droplets for calculating r_e to directly compare with observations obtained using, e.g., forward scattering spectrometer probe (e.g., Brenguier et al., 1998; Arabas and Shima, 2013), this study uses all drops to calculate r_e because the effect of TICE on the growth of small droplets into large drops is explicitly analyzed. Therefore, the mean effective radius presented in this study is slightly larger than that reported in previous studies.

The mean effective radius increases with height and exhibits a maximum directly below the cloud top, which largely agrees with previous studies (e.g., Arabas and Shima, 2013). The height at which the mean effective radius reaches its maximum depends on the specific cases; however, the maximum typically occurs between z = 2 km and z = 3 km. The maximum mean effective radius is approximately 130 μm when N_0 = 30 cm^{-3} and decreases as N_0 increases.

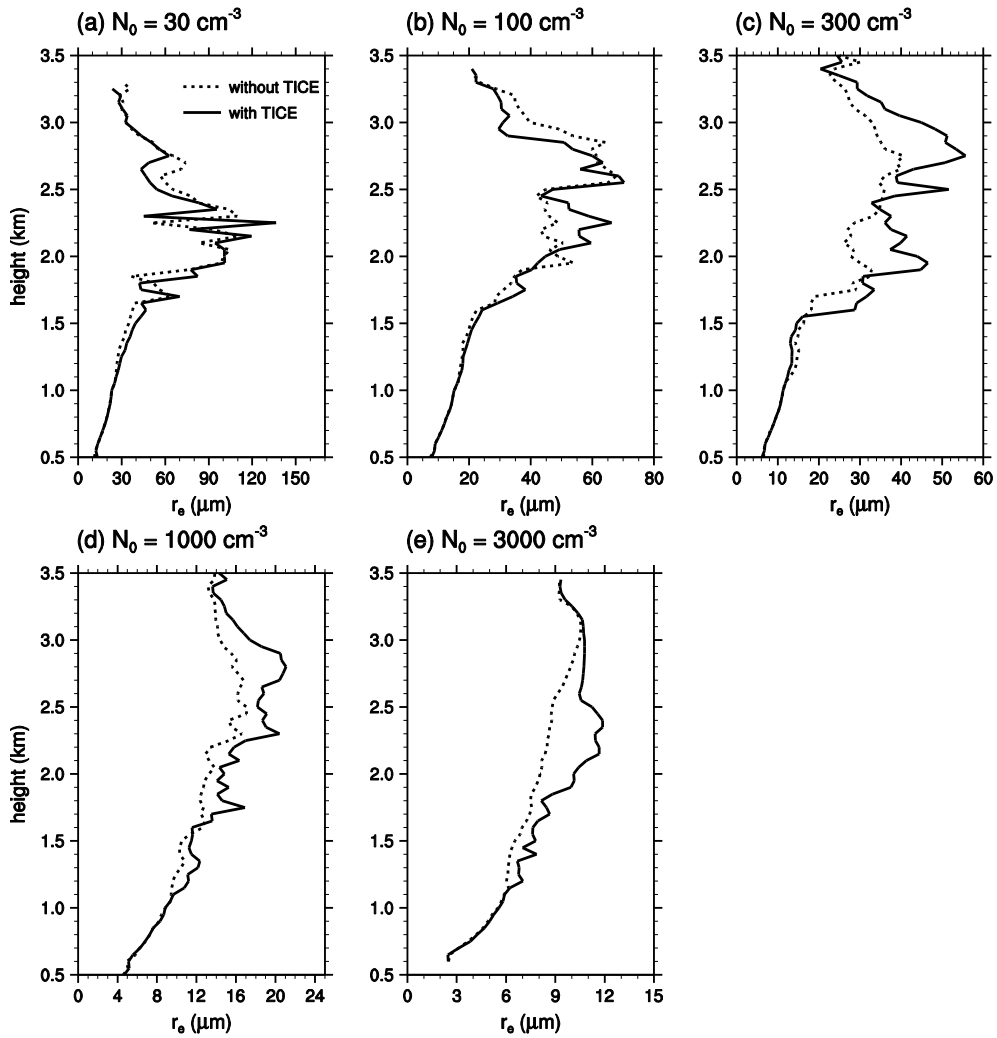

Figure 3.3 Vertical distribution of mean effective radius r_e (μm) averaged over the grid points at which the cloud drop number concentration (CDNC) ≥ 20 cm^{-3} except for N_0 = 30 cm^{-3} (CDNC ≥ 15 cm^{-3}) for N_0 = (a) 30, (b) 100, (c) 300, (d) 1000, and (e) 3000 cm^{-3}. r_e is averaged over t = (a), (b), and (c) 10–30 min, (d) 15–35 min, and (e) 35–55 min. Solid and dotted lines correspond to the cases with and without TICE, respectively.

Moreover, the maximum mean effective radius is less than 20 μm when N_0 is greater than 1000 cm^{-3}.

TICE is expected to increase the drop sizes due to the accelerated collisions between small droplets. However, when N_0 = 30 and 100 cm^{-3}, the changes in the mean effective radius that are caused by TICE are not distinct. When N_0 = 30 cm^{-3}, the mean effective radius is slightly larger only near z = 1–2 km when TICE is included compared with the case without TICE; for N_0 = 100 cm^{-3}, the same is true only near z =1.5–2.5 km (Figs. 3a and 3b). However, the increase in the mean effective radius becomes smaller or even completely diminishes above these layers. Generally, the enlarged drop radius that is caused by TICE is more pronounced as the CCN concentration increases. When N_0 = 3000 cm^{-3}, the mean effective radius is enlarged by nearly 50% for z = 2–2.5 km as a result of TICE. Although the model is designed such that TICE always accelerates the coalescence of droplets, the enlarged drop radius that is caused by TICE is only well pronounced for high CCN concentrations, i.e., $N_0 \geq 300$ cm^{-3} in this study. The effect is not certain for low CCN concentrations.

Figure 3.4 shows the vertical distribution of the mean CDNC for various CCN concentrations. Except when N_0 = 30 cm^{-3}, the mean CDNC tends to decrease with height. TICE is expected to reduce the mean CDNC due to the accelerated coalescence of droplets. However, TICE produces only a very small changes in CDNC when N_0 = 30 cm^{-3} and the change in the CDNC caused by TICE depends on height when N_0 = 100 cm^{-3}. The reduction in the CDNC is more pronounced when $N_0 \geq 300$ cm^{-3}.

By analyzing the mean effective radius and the CDNC, it is concluded that

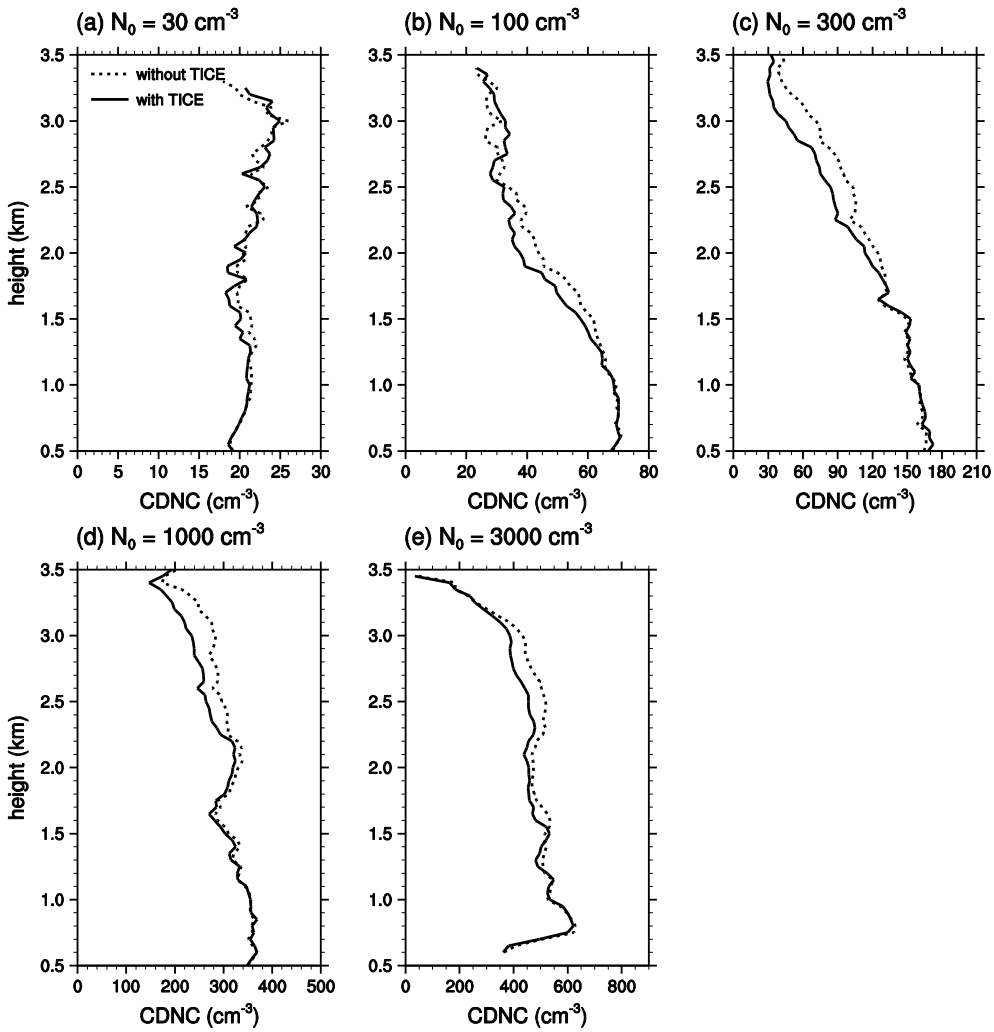

Figure 3.4 As in Fig. 3 but for CDNC (cm^{-3}).

TICE exhibits only a small effect on acceleration in the growth of droplets by coalescence for low CCN concentrations. Because TICE affects the coalescence of relatively small droplets, if droplets are capable of growing via vapor diffusion to sizes that are sufficient for coalescence without TICE, the coalescence acceleration caused by TICE becomes small. Due to the humid atmosphere that is considered in this study, the diffusional growth of small droplets is sufficiently vigorous such that the droplets grow to sizes at which coalescence is effective even without TICE for low CCN concentrations. Therefore, the differences in the mean effective radius and in the mean CDNC between the cases with and without TICE are small.

To evaluate the model suitability for investigating the effects of TICE, the instantaneous fields for the turbulent dissipation rate ε, Taylor microscale Reynolds number Re_λ, liquid water content (LWC) at t = 15 min for N_0 = 100 cm^{-3}, and the time series of the turbulent dissipation rate are presented in Fig. 3.5. Observational studies have revealed that a typical Re_λ is ~10^4 and a typical ε is in the range 10^{-4}–10^{-2} m^{-2} s^{-3} for shallow convective clouds or cumuli (Jonas, 1996; Pruppacher and Klett, 1997; Siebert et al., 2006, 2010). However, Re_λ and ε have been known to exhibit a very high temporal and spatial variability (Shaw, 2003; Benmoshe et al., 2012). In this study, the instantaneous fields of ε and Re_λ also exhibit a high spatial variability (Figs. 3.5a and 3.5b). Comparatively high values of ε appear near the cloud top, where the wind shear is large. Figures 3.5a and 3.5c show the collocation of regions in which large ε and LWC appear. This result agrees with the results of previous studies (e.g., Seifert et al., 2010; Benmoshe et al., 2012; Khain et al., 2013) and suggests that TICE is generally large in areas

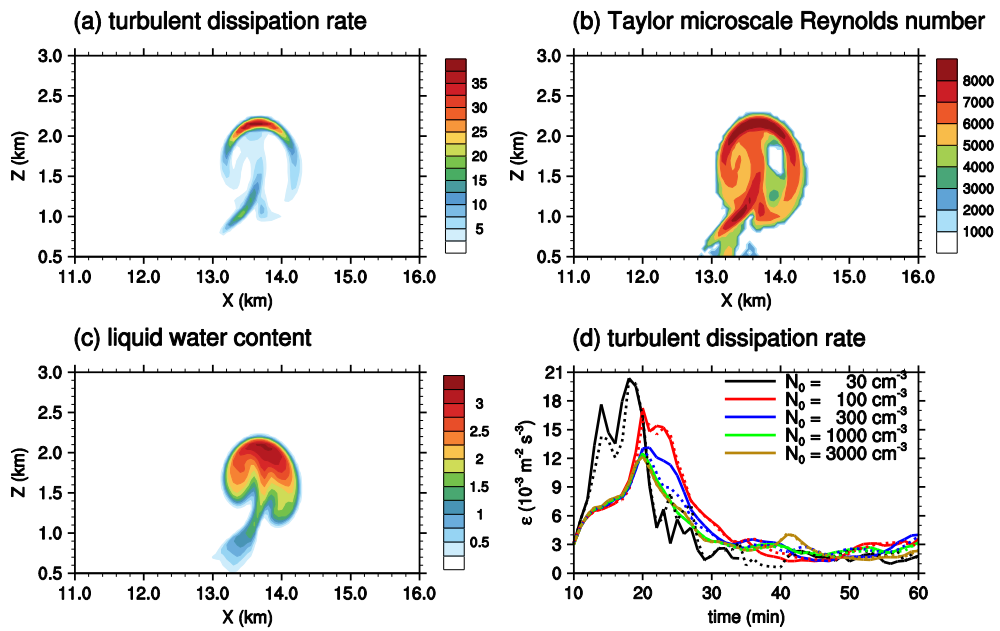

Figure 3.5 (a) Turbulent dissipation rate (10^{-3} m^{-2} s^{-3}), (b) Taylor microscale Reynolds number, (c) liquid water content (g m^{-3}) fields at t = 15 min for N_0 = 100 cm^{-3} when TICE is included, and (d) averaged turbulent dissipation rate time series. Solid and dashed lines in (d) correspond to the cases with and without TICE, respectively.

with high drop concentrations. Therefore, TICE efficiently affects the coalescence of small droplets. Figure 3.5d indicates that the turbulent dissipation rate is not largely affected by the CCN concentration and TICE. The turbulent dissipation rate increases to ~10^{-2} m^{-2} s^{-3} during the early stage of cloud development and then decreases before remaining at ~10^{-3} m^{-2} s^{-3} after the decay of the initial cloud in each simulation, which is within the range suggested in previous studies.

3.4. Effects of TICE on surface precipitation

Figure 3.2d shows that TICE increases the amount of surface precipitation when $N_0 \geq 300$ cm^{-3}, whereas TICE decreases the amount of surface precipitation when $N_0 \leq 100$ cm^{-3}. Therefore, the cases in which $N_0 = 1000$ cm^{-3} and $N_0 = 100$ cm^{-3} are chosen to further investigate the different effects of TICE on the amount of surface precipitation. The case of $N_0 = 1000$ cm^{-3} represents the relatively high CCN concentration cases, and the case of $N_0 = 100$ cm^{-3} represents the relatively low CCN concentration cases.

Previous studies have suggested that the rapid growth of cloud droplets to raindrops is the primary mechanism by which TICE increases the amount of surface precipitation (e.g., Franklin, 2008). Therefore, the cloud water content and rainwater content are examined to determine how TICE contributes to the increase in the amount of surface precipitation for high CCN concentrations. Figures 3.6 and 3.7 show the cloud water content and rainwater content fields at $t = 27$ min and $t = 32$ min for $N_0 = 1000$ cm^{-3}, respectively. At $t = 27$ min, the cloud water content is smaller and the rainwater content is larger in the case with TICE compared with the case without TICE. This result is simply related to the

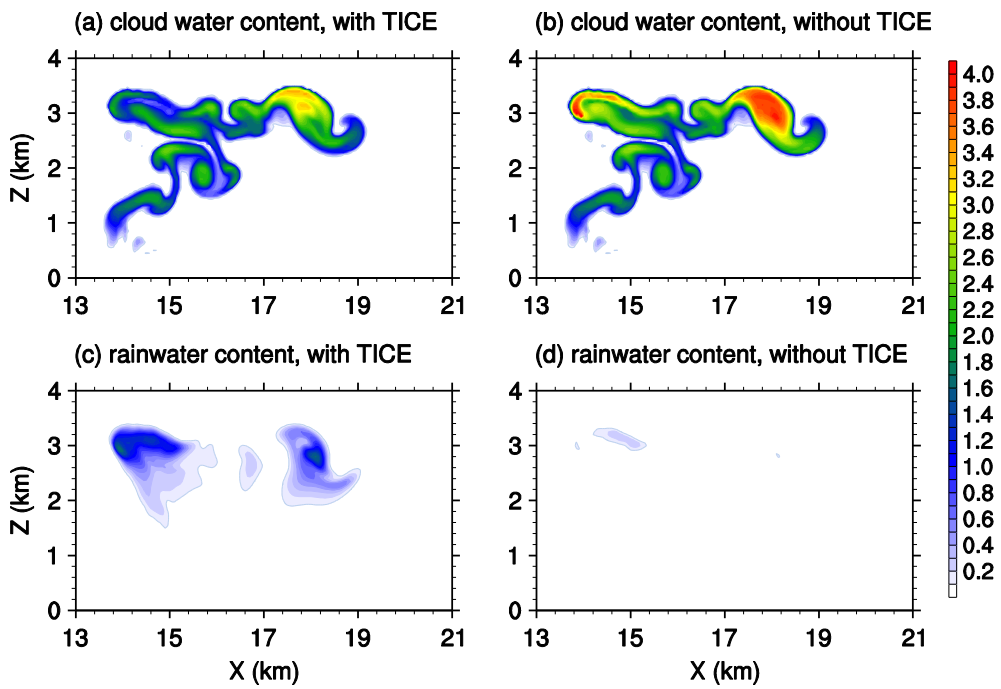

Figure 3.6 (a) Cloud water content (g m^{-3}) and (c) rainwater content (g m^{-3}) fields at t = 27 min for N_0 = 1000 cm^{-3} when TICE is included. (b) and (d) are the same as (a) and (c), respectively, but when TICE is not included

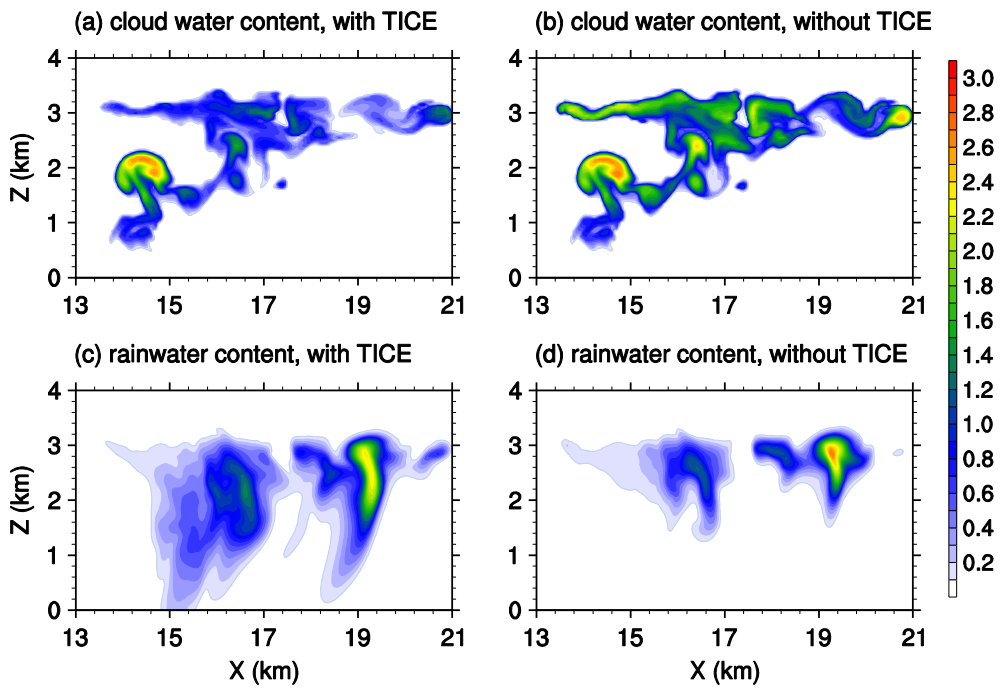

Figure 3.7 As in Fig. 3.6 but at t = 32 min.

enhanced coalescence between cloud droplets, resulting in the more rapid growth of cloud droplets into raindrops. At t = 32 min, the cloud water content remains smaller and the rainwater content remains larger in the case with TICE compared with the case without TICE (Fig. 3.7). Because cloud droplets are quite small for high CCN concentrations, the droplets are less likely to coalesce into raindrops when only gravitational collisions are represented. However, in the case with TICE, cloud droplets coalesce and grow into raindrops more easily. Consequently, the rainwater content and the amount of surface precipitation increase.

Figure 3.8 shows the rainwater fraction time series for the cases with and without TICE for N_0 = 1000 cm^{-3}. Here, the rainwater fraction is defined as the ratio of the total rainwater content to the total liquid water content (i.e., the cloud water content plus rainwater content) in the entire domain. The maximum rainwater fraction is 0.57 at t = 34 min in the case with TICE; a smaller maximum value (0.44 at t = 37 min) is observed in the case without TICE. This result demonstrates that the growth of cloud droplets into raindrops is both delayed and suppressed in the case without TICE for N_0 = 1000 cm^{-3}.

In contrast to the high CCN concentration results, TICE slightly decreases the amount of surface precipitation for low CCN concentrations. To examine how TICE decreases the amount of surface precipitation for low CCN concentrations, the cloud water content and rainwater content fields at t = 20 min and t = 25 min for N_0 = 100 cm^{-3} are depicted in Figs. 3.9 and 3.10, respectively. Because of the accelerated onset of surface precipitation that is caused by a reduction in the CCN concentration, the time instants are different from those selected for the N_0 = 1000 cm^{-3} analysis (Figs. 3.2c and 3.2d).

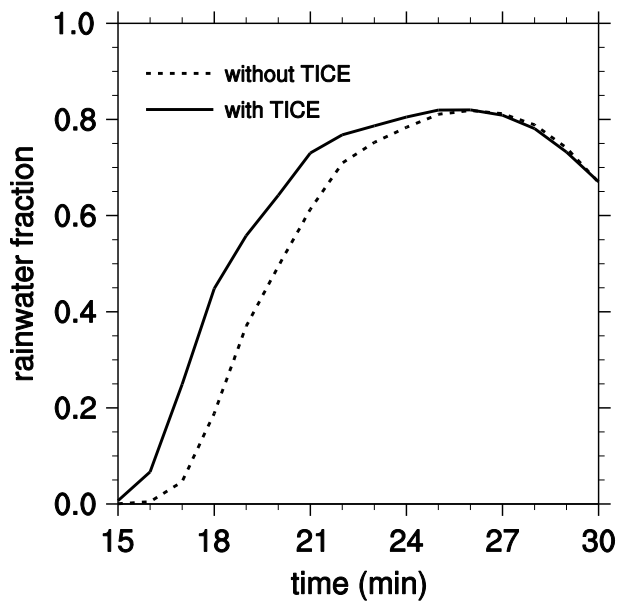

Figure 3.8 The rainwater fraction time series in the cases with and without TICE for N_0 = 1000 cm^{-3}.

At t = 20 min (Fig. 3.9), the cloud water content is smaller and the rainwater content is larger in the case with TICE compared with the case without TICE; this result is the same as for N_0 = 1000 cm^{-3}. However, at t = 25 min (Fig. 3.10), the cloud water content and rainwater content differences between the two cases are small. The rainwater content in the case with TICE is larger only below z ~ 1.6 km (Figs. 3.10e and 3.10f). Above z ~ 1.6 km, the rainwater content in the case with TICE is smaller than that in the case without TICE. These changes are because raindrops in the case with TICE fall into the lower layer, while cloud droplets in the case without TICE coalesce into raindrops in the upper layer at t = 20–25 min.

Figure 3.11 shows the rainwater fraction time series for N_0 = 100 cm^{-3}. Rainwater is produced approximately 1 min earlier in the case with TICE compared to the case without TICE and the rainwater fraction is larger until t = 26 min in the case with TICE. However, the rate at which the rainwater fraction increases is similar in the two cases. The rainwater fractions are nearly the same after t = 26 min. The decrease in the rainwater fraction after t = 26 min is primarily due to the fallout of raindrops to the surface. The maximum rainwater fraction in the case with TICE (0.82) is approximately the same as in the case without TICE.

The amount of accumulated surface precipitation is slightly smaller in the cases with TICE than in the cases without TICE for low CCN concentrations despite the accelerated formation of raindrops and the subsequent earlier onset of surface precipitation. To explain this result, the diffusional processes are examined because the collision-coalescence process and the breakup process do not affect

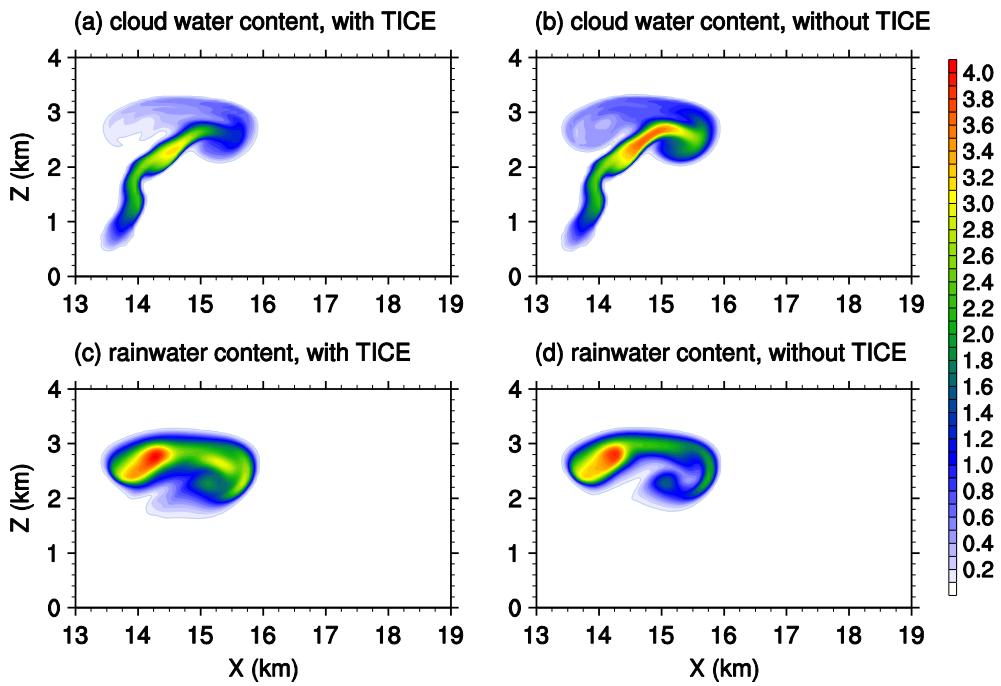

Figure 3.9 (a) Cloud water content (g m^{-3}) and (c) rainwater content (g m^{-3}) fields at t = 20 min for N_0 = 100 cm^{-3} when TICE is included. (b) and (d) are the same as (a) and (c), respectively, but when TICE is not included.

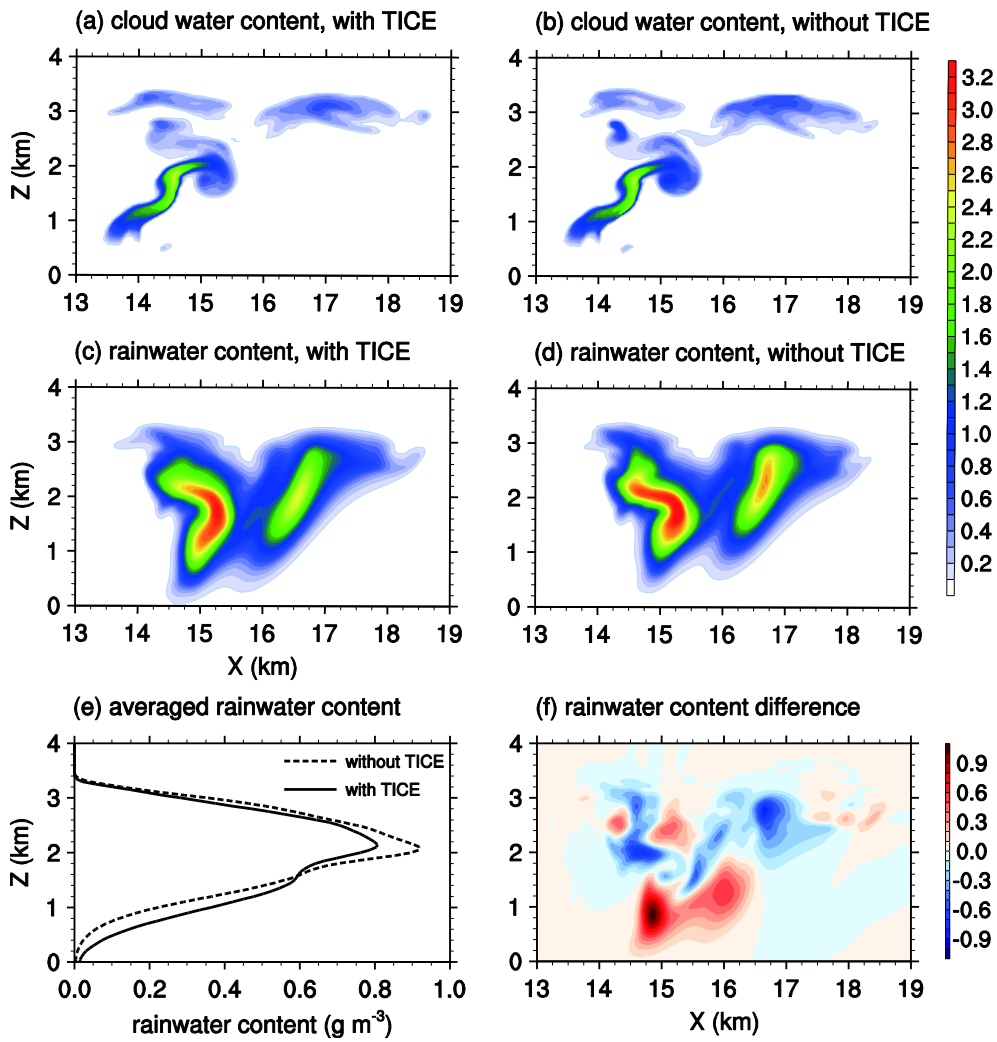

Figure 3.10 (a)–(d) as in Fig. 3.9 but at t = 25 min, (e) vertical profiles of rainwater content (g m–3) averaged over x = 13–19 km, and (f) the difference in rainwater content due to TICE at t = 25 min for N_0 = 100 cm^{-3}.

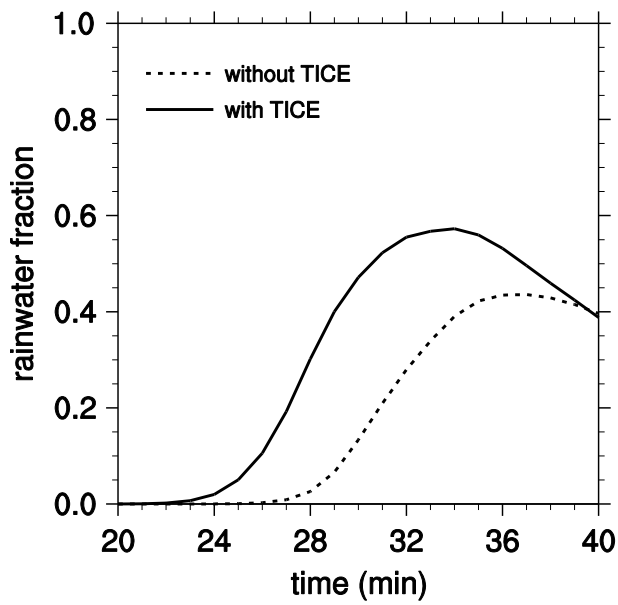

Figure 3.11 The rainwater fraction time series in the cases with and without TICE for N_0 = 100 cm^{-3}.

the total water content. A comparison between condensation and evaporation shows that the condensation process dominates the evaporation process during the developing stage of the cloud in the individual cases (not shown). Therefore, the differences in the total liquid water mass primarily originate from the condensation process.

The vertical profile of the horizontally averaged condensational heating rate for t = 20–25 min and N_0 = 100 cm^{-3} is plotted in Fig. 3.12a. This figure shows that the condensation rate in the case with TICE is smaller than in the case without TICE. This difference is most noticeable for z = 2–3 km, where most cloud droplets are concentrated (see Fig. 3.9). The rapid decrease in the condensation rate above z = 3 km is due to the existence of the inversion layer and the resultant constraint on upward motion. Figure 3.12b shows the domain-averaged condensational heating rate time series. The condensation rate in the case with TICE is smaller than that in the case without TICE. The total condensation for t = 0–25 min, which is calculated by integrating the condensation rate over the period, is smaller in the case with TICE than in the case without TICE by 2.6%. This decrease in the total condensation due to TICE is caused by the early coalescence of small droplets. Accelerated collisions between small droplets increase the mean drop radius and decrease the sum of the drop radii if the total liquid water content is assumed to be constant. Therefore, the total condensation decreases, because it is proportional to the sum of the drop radii.

The decrease in the total condensation may also be caused by the reduced liquid water content because TICE decreases the liquid water content via the

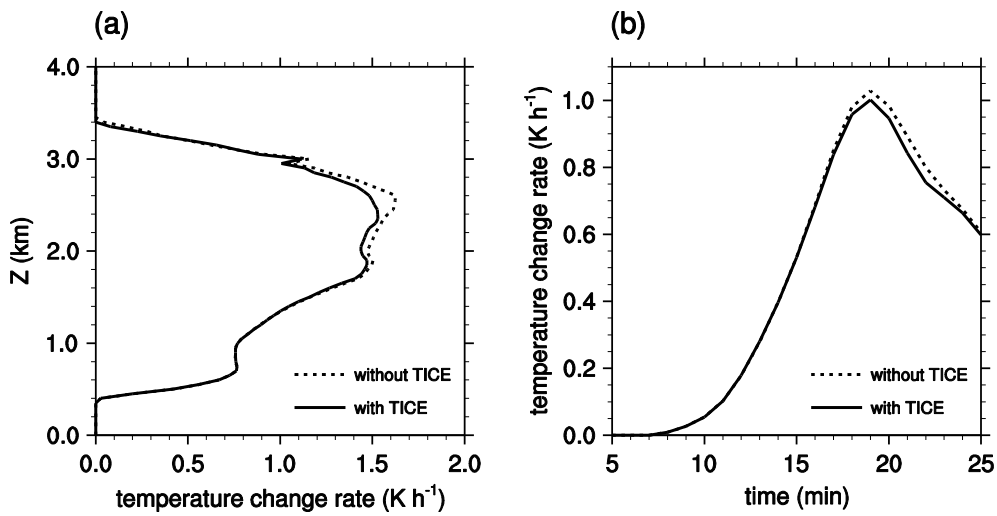

Figure 3.12 (a) Vertical profile of the horizontally averaged condensational heating rate (K h^{-1}) for t = 20–25 min and (b) the domain-averaged condensational heating rate time series in the cases with and without TICE for N_0 = 100 cm^{-3}.

accelerated coalescence and fallout of drops during the early stage of cloud development. By comparing the total condensation per unit liquid water content, it is revealed that the decrease in the sum of the drop radii has a larger effect than the liquid water content decrease on the reduced total condensation (not shown). However, it is certain that the reduced liquid water content plays a partial role in reducing the total condensation. The reduced liquid water content, which is caused by the accelerated fallout of large drops, should be considered together with the decrease in the sum of the drop radii to account for the reduction in the total condensation due to TICE.

Figure 3.13 shows the drop size distributions for N_0 = 100 and 1000 cm^{-3}. The distributions are derived in the rain shaft area, i.e., where the rainwater mixing ratio $\geq$ 0.5 g kg^{-1} and z < 0.5 km, following previous observational studies (e.g., Baker et al., 2009). The time instant is selected to approximately coincide with the surface precipitation rate maximum in each case. When N_0 = 100 cm^{-3}, although the difference in the two cases is very small, the number concentration of large drops (r > 600 μm) is smaller in the case with TICE than in the case without TICE. However, when N_0 = 1000 cm^{-3}, the number concentration of large drops is 10–1000 times higher in the case with TICE than in the case without TICE. The number concentration of small droplets is also higher in the case with TICE than in the case without TICE.

Thus far, our analysis has focused on the cloud microphysical properties. It is known that differences in the amount of surface precipitation also arise from differences in cloud dynamical properties, such as updraft intensity or cloud top height (e.g., Han et al., 2012; Wyszogrodzki et al., 2013). To investigate the

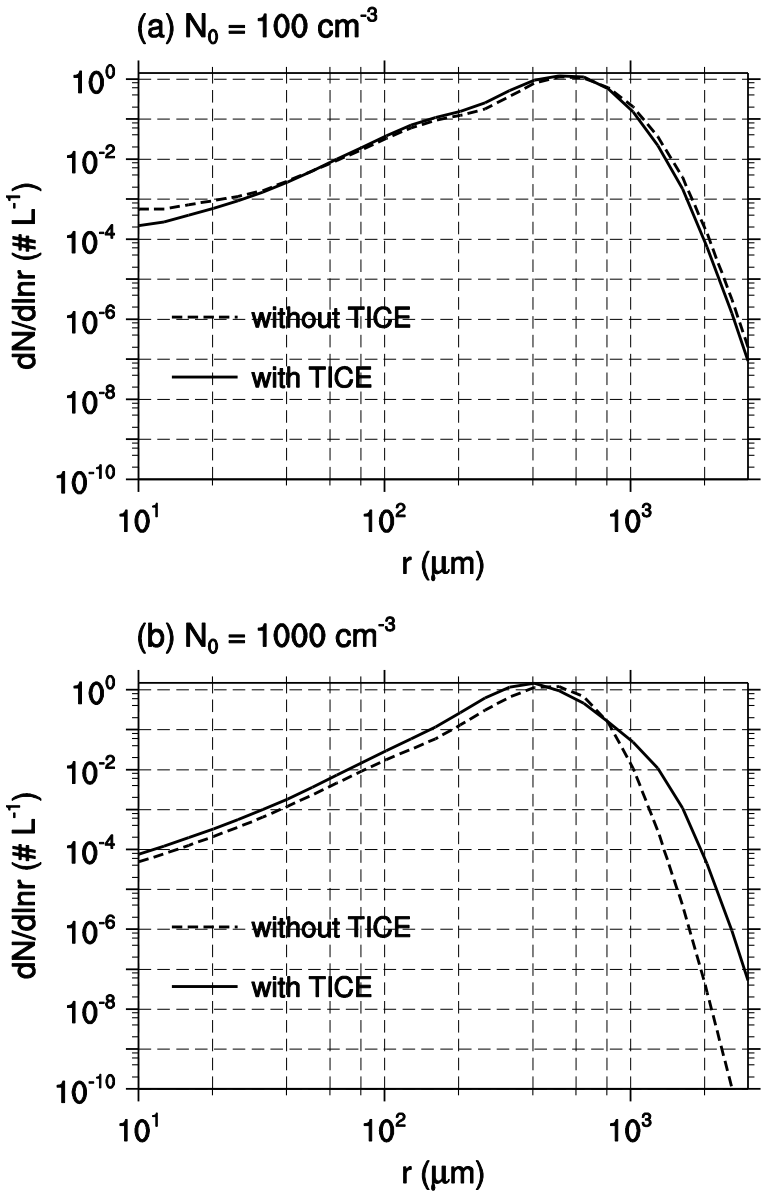

Figure 3.13 Drop size distributions (L^{-1}) in the area where rainwater mixing ratio ≥ 0.5 g kg^{-1} and $z < 0.5$ km (a) for $N_0 = 100$ cm^{-3} at $t = 30$ min and (b) for $N_0 = 1000$ cm^{-3} at $t = 40$ min.

effects of TICE on cloud dynamical properties, the vertical wind velocity is analyzed. The vertical distribution of the mean vertical wind velocity is displayed in Fig. 3.14. Referring to Figs. 3.4b and 3.4c, when N_0 = 100 cm^{-3} and N_0 = 300 cm^{-3}, the mean vertical wind velocity appears to be related to the CDNC because a decrease in the CDNC decreases the condensational heat release. However, such a relationship is not applicable for the other CCN concentrations. Moreover, the mean vertical wind velocity near the cloud base, which is an important dynamical property, is not altered by TICE. Because of the strong inversion layer between z = 3 km and z = 3.4 km, the difference in the mean vertical wind velocity cannot alter the cloud top height. The importance of this result was previously noted by Wyszogrodzki et al. (2013). These results indicate that the differences in cloud microphysical properties exert a large control on changes in the amount of surface precipitation in this study and that the vertical wind velocity differences appear to have a relatively small role. However, this conclusion may originate from the numerical method used in this study because convection is initiated by an externally imposed heating. Further detailed studies are required to investigate the effects of TICE on cloud dynamical properties.

3.5. Comparisons with results of previous studies

A few recent studies (e.g., Seifert et al., 2010; Wyszogrodski et al., 2013) have also investigated the effects of TICE on clouds, especially on warm clouds. These studies concluded that the amount of surface precipitation always increases due to TICE. However, in this study, changes in the amount of surface precipitation depend on the CCN concentration. The amount of surface precipitation decreased

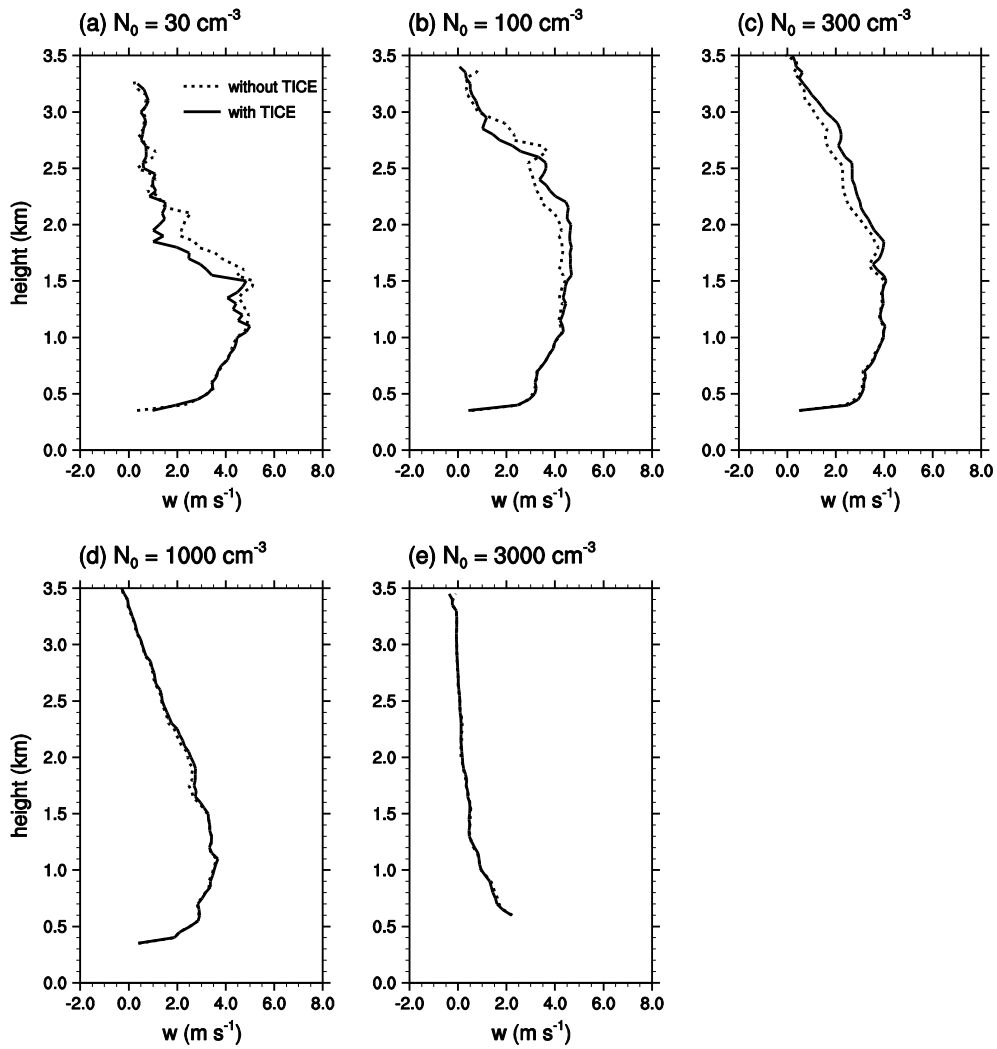

Figure 3.14 Vertical distribution of vertical velocity (m s^{-1}) averaged over the grid points at which the cloud drop number concentration (CDNC) ≥ 20 cm^{-3} except for N_0 = 30 cm^{-3} (CDNC ≥ 15 cm^{-3}) for N_0 = (a) 30, (b) 100, (c) 300, (d) 1000, and (e) 3000 cm^{-3}. The vertical velocity is averaged over t = (a), (b), and (c) 10–30 min, (d) 15–35 min, and (e) 35–55 min. Solid and dotted lines correspond to the cases with and without TICE, respectively.

slightly due to TICE for low CCN concentrations.

The numerical models used in the individual studies are different. Wyszogrodski et al. (2013) used an LES model with bin microphysics in which the bin resolution (mass-doubling every three bins) is higher than that used in this study (mass-doubling every one bin). They obtained the same conclusions, which shows that the amount of surface precipitation always increases due to TICE, for both an idealized 2-D and a realistic 3-D setup. Seifert et al. (2010) used another LES model with bulk microphysics and obtained nearly the same conclusions. Therefore, it seems that the number of spatial dimensions and the model complexity for treating the drop size distribution have only a small effect on the conclusions.

To investigate potential causes for the different results of this study compared with previous studies, additional numerical experiments are performed. The relative humidity is set to 70% at the surface and 77% near the cloud base, which is 15% lower relative to the original environmental conditions. The water vapor mixing ratio at the surface is 14.4 g kg^{-1}, and the water vapor mixing ratio averaged over the lowest 1 km is 12.2 g kg^{-1}.

The surface precipitation rate time series for the modified environmental conditions and N_0 = 30, 100, 300, 1000, and 3000 cm^{-3} are depicted in Fig. 3.15. The amount of surface precipitation is considerably smaller compared with the simulations performed with the original environmental conditions, i.e., the amount of surface precipitation is strongly affected by humidity. For example, the maximum surface precipitation rate decreases by more than 90% compared with the simulations performed using the original environmental conditions for N_0 = 30

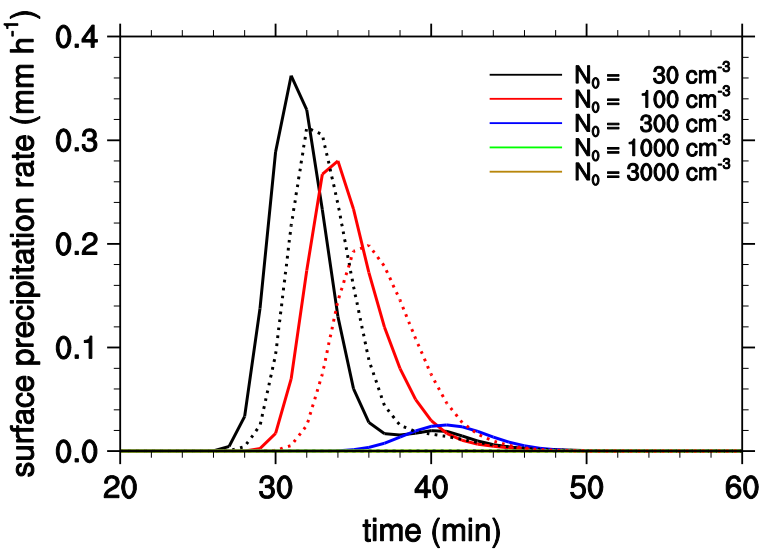

Figure 3.15 Surface precipitation rate time series (mm h^{-1}) averaged over x = 13–23 km in drier environmental conditions (a relative humidity of 70 % at the surface) for N_0 = 30, 100, 300, 1000, and 3000 cm^{-3}. Solid and dashed lines correspond to the cases with and without TICE, respectively.

cm^{-3}, and the extent of the decrease increases rapidly as N_0 increases. Moreover, even in the cases with TICE, there is no surface precipitation when $N_0 \geq 1000$ cm^{-3}.

The amount of surface precipitation always increases due to TICE under the modified environmental conditions; this conclusion corresponds to the findings of the previous studies. In the original environmental conditions of this study, the amount of surface precipitation decreases due to TICE for low CCN concentrations because the small droplets can grow via vapor diffusion such that they efficiently coalesce without TICE. In drier environmental conditions, such growth of small droplets by vapor diffusion is suppressed. Therefore, the decreased surface precipitation due to TICE does not appear.

Another important aspect of this study is that the amount of surface precipitation increases with increasing CCN concentration for low CCN concentrations (when N_0 is less than 300 cm^{-3} with TICE and less than 100 cm^{-3} without TICE) under the original environmental conditions. The increased surface precipitation with increasing aerosol concentration does not appear in the simulations performed with the modified drier environmental conditions.

It is widely accepted that an increase in aerosol concentration suppresses the amount of surface precipitation in warm clouds (e.g., Albrecht, 1989; Rosenfeld, 1999; Xue and Feingold, 2006; Xue et al., 2008). Although an increase in aerosol concentration reduces surface precipitation due to reduced droplet sizes in warm clouds is regarded as “conventional wisdom”, it is frequently found that an increase in the aerosol concentration increases the surface precipitation up to a certain aerosol concentration (e.g., Givati and Rosenfeld, 2004; Seifert and

Beheng, 2006; Fan et al., 2009; Carrió et al., 2010; Carrió and Cotton, 2011; Lakshmana et al., 2012) or monotonically increases the surface precipitation (e.g., Lee et al., 2010; Han et al., 2012; Lee and Feingold, 2013) in deep convective clouds. Khain (2009) reviewed the relationships between aerosol concentration and the amount of surface precipitation and showed that the decrease in the amount of surface precipitation with increasing aerosol concentration generally occurs in dry and continental environments or in warm and shallow cumuli. This study suggests that even in warm clouds, the relationship between aerosol concentration and surface precipitation also depends on the humidity of the atmosphere.

The results of this study largely agree with those of Benmoshe et al. (2012), which show that the effects of TICE on surface precipitation are opposite to the effects of increasing aerosol concentration on surface precipitation. In this study, surface precipitation decreases (increases) due to TICE when the aerosol concentration is with the range in which an increase in the aerosol concentration increases (decreases) the surface precipitation.

4. Effects of turbulence on mixed-phase deep convective clouds and precipitation

4.1. Experimental setup

To simulate mixed-phase deep convective clouds, the thermodynamic sounding used in Weisman and Klemp (1982) is adopted (Fig. 4.1). Two basic-state wind profiles are used: one is expressed by a tangent hyperbolic function $U = U_s \tanh(z/z_s)$ with $U_s = 15$ m s^{-1} and $z_s = 3$ km, while the other is a uniform wind with a speed of 3 m s^{-1}. In this study, for simplicity, all aerosol particles are assumed to serve as cloud condensation nuclei (CCN) according to supersaturation and aerosol particle size. Following Khain et al. (2000), the initial aerosol size distribution is determined using the Twomey equation (Twomey, 1959) and the Köhler equation (Köhler, 1936). The aerosol size distribution $N(r_a)$ is expressed by

$$\frac{dN}{d\ln r_a} = \frac{3}{2} N_0 k \left(\frac{4A^3}{27Br_a^3} \right)^{k/2}, \tag{4.1}$$

where r_a is the radius of aerosol, N_0 is the CCN concentration at 1% supersaturation, k is a constant, A is a temperature-dependent coefficient that is related to the curvature effect, and B is a constant that is related to the solution effect. The value of k is specified as 0.5. To examine the effects of TICE with

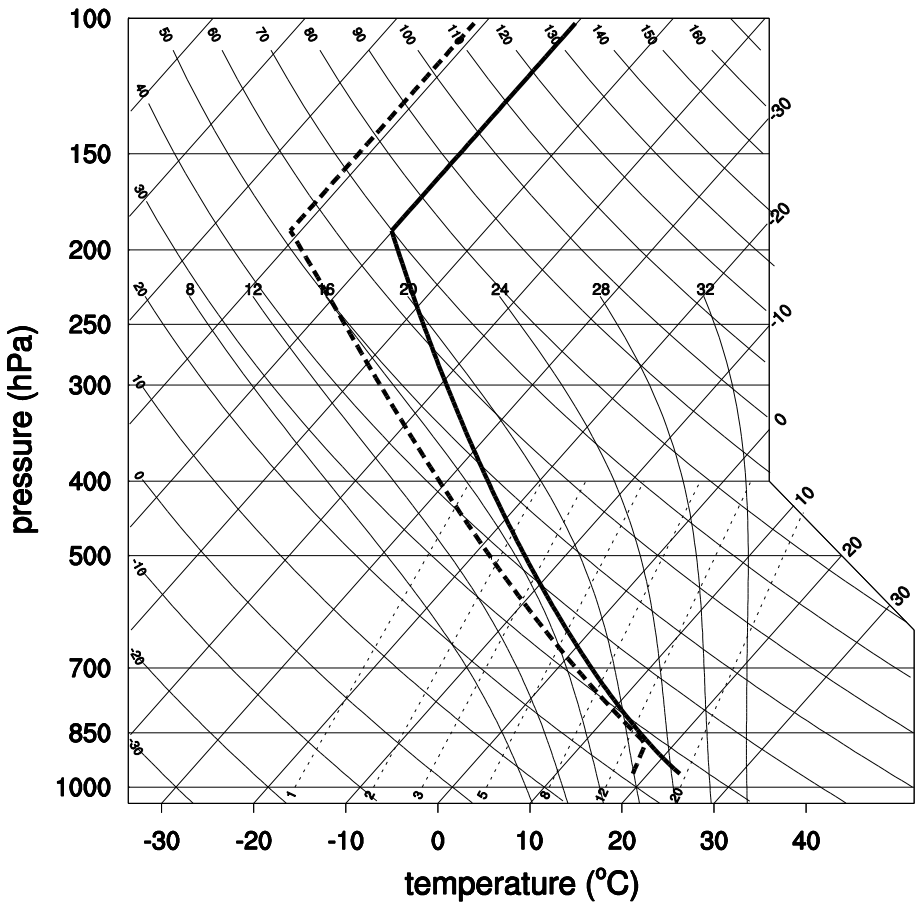

Figure 4.1 Thermodynamic sounding used in this study, which is adopted from Weisman and Klemp (1982). Thick solid and dashed lines indicate the air temperature and dew point temperature, respectively.

different aerosol concentrations, 500 cm^{-3} and 4000 cm^{-3} are used for N_0.

Table 4.1 lists the names and settings of the eight simulations performed for this study. The domain size is 256 km in the horizontal and 18 km in the vertical. A damping layer is included from z = 14 km to the model top height. The grid size is 250 m in the horizontal and 125 m in the vertical. The time step is 4 s except for the diffusional process (0.4 s), and the integration time is 4 h. Convection is initiated by the specified low-level heating.

4.2. Uniform basic-state wind cases

The vertical profiles of mass distribution of each hydrometeor type for the uniform basic-state wind cases are depicted in Figs. 4.2 and 4.3. Figure 4.2 is for TU500 and GU500, while Fig. 4.3 is for TU4000 and GU4000. Despite the different CCN concentrations, the effects of TICE appear to be similar. For t = 80–100 min, although the differences are small, the most significant change by TICE is a decrease in cloud water mass and an increase in rainwater mass. This is simply due to the accelerated coalescence between small droplets. Almost all ice particles consist of graupel particles during this period, and TICE increases graupel mass. TICE causes the produced graupel particles to grow more quickly because of the enhanced collision between graupel particles and droplets. Hail mass also increases by TICE, but the increased mass is small. These changes are more pronounced under the high CCN concentration than under the low CCN concentration.

Also, for t = 130–150 min, the main features of the mass distributions of the hydrometeor types commonly appear under both the low and the high CCN

Table 4.1 Names and settings of eight simulations performed for this study.

	Collision kernel	Basic-state wind	CCN concentration at S_w = 1% (cm^{-3})
TU500	turbulence	uniform	500
GU500	gravitation	uniform	500
TU4000	turbulence	uniform	4000
GU4000	gravitation	uniform	4000
TS500	turbulence	sheared	500
GS500	gravitation	sheared	500
TS4000	turbulence	sheared	4000
GS4000	gravitation	sheared	4000

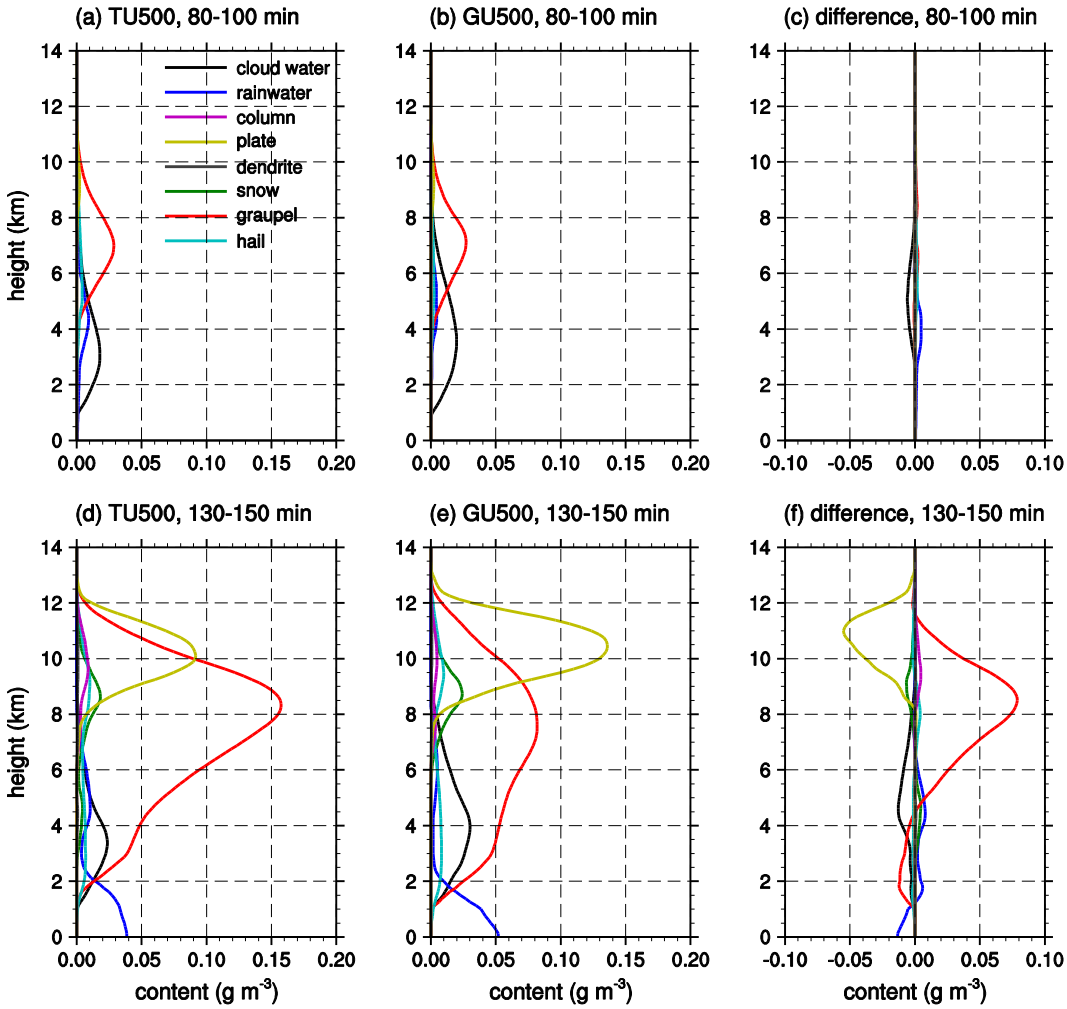

Figure 4.2 Vertical profiles of mass distribution of each hydrometeor type averaged for t = 80–100 min in (a) TU500 and (b) GU500. (c) is the difference between (a) and (b). (d)–(f) are the same as (a)–(c) but averaged for t = 130–150 min.

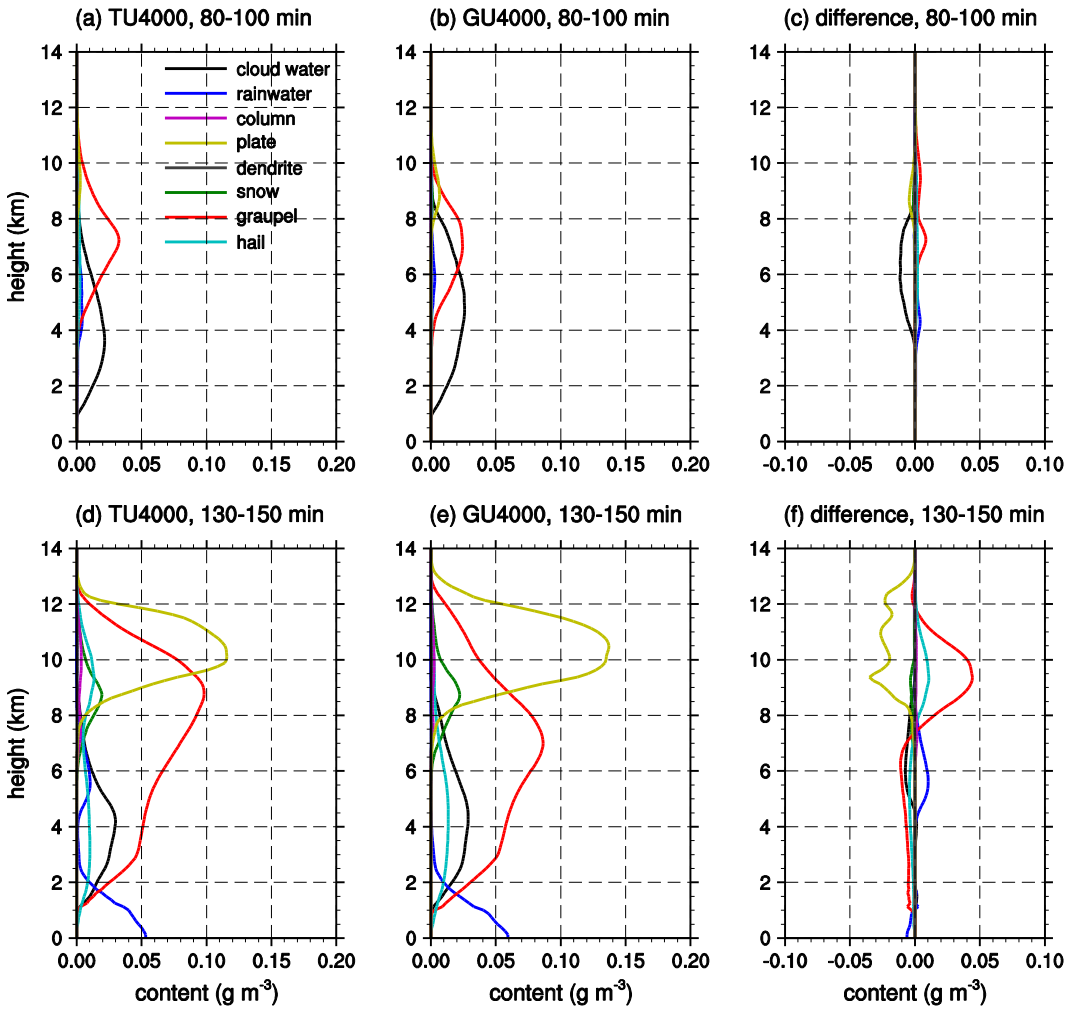

Figure 4.3 As in Fig. 4.2 but for TU4000 and GU4000.

concentration. Cloud water mass in TU500 and TU4000 is still smaller than that in GU500 and GU4000, respectively. It is seen that most of the cloud mass consists of ice particles, in particular plate-type ice crystals and graupel particles. Most of the ice crystals, which are mainly plate-type ice crystals, are present in the layer z > 8 km. By TICE, plate-type ice crystal mass decreases and graupel mass in the upper layer (z > 5 km in TU500 and GU500 and z > 7 km in TU4000 and GU4000) increases. This shows that the growth from ice crystals to graupel particles becomes more rapid by TICE. When TICE is considered, however, graupel mass in the lower layer and rainwater mass in the layer z < 1 km decrease. The amount of surface precipitation (rainwater mass at the surface) is then reduced by TICE during this period.

Previous studies have shown that surface precipitation from mixed-phase deep convective clouds is mainly contributed by the melting of ice particles, in particular when the freezing level is relatively low (e.g., Khain et al., 2011). Figures 4.2f and 4.3f also seem to suggest that it is the decrease in graupel mass in the lower layer that leads to the decrease in surface precipitation. This is examined with the spatial distribution fields of graupel mass averaged for t = 130–150 min (Fig. 4.4). Under both the low and the high CCN concentration, graupel particles in the upper layer (z > 8 km) are distributed more widely when TICE is included. Graupel mass along the narrow shaft area in the lower layer (x ~ 70 km and z < 6 km) is smaller in TU500 and in TU4000 than in GU500 and GU4000, respectively. This decrease in graupel mass in the lower layer is consistent with the results shown in Figs. 4.2 and 4.3.

Small graupel particles do not have enough terminal velocities to penetrate

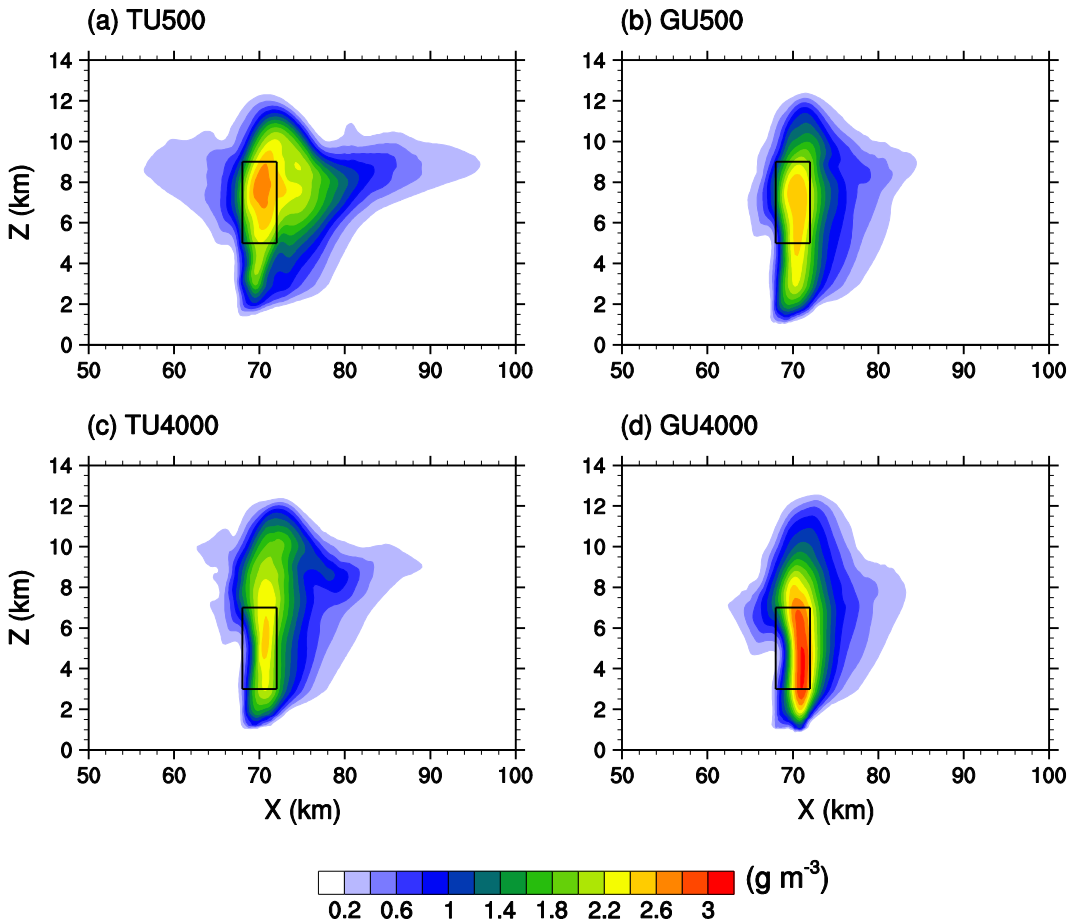

Figure 4.4 Spatial distribution fields of graupel mass averaged for t = 130–150 min in (a) TU500, (b) GU500, (c) TU4000, and (d) GU4000. The rectangular box indicates the cloud core area.

the strong updraft zone in the cloud, so they tend to remain aloft and to be advected by winds. On the other hand, large graupel particles have large terminal velocities, so they can fall toward the ground. The broader spatial distribution of graupel mass in the high altitudes and the decrease in graupel mass in the low altitudes when TICE is considered imply that TICE reduces the size of graupel particles. Because TICE accelerates drop-drop collisions, the droplet number concentration decreases and the supersaturation increases. This makes ice crystals grow quickly by deposition and collide with supercooled drops efficiently, which results in the enhanced formation of small graupel particles, as proposed in Khain et al. (2011). The rapid transition from ice crystals to small graupel particles is also reflected in Figs. 4.2 and 4.3.

Figure 4.5 shows the size distributions of graupel particles in the cloud core area in TU500, GU500, TU4000, and GU4000. One interesting aspect of the size distributions is that the number size distribution is very different from the mass size distribution. In the number size distribution, the radii of most graupel particles range between 10 μm and 1 mm. The number concentration of graupel particles whose radii are larger than ~300 μm increases by TICE. Also, the number-averaged radius of graupel particles increases by TICE (34% in TU500 and 73% in TU4000). In the mass size distribution, however, almost all graupel mass is concentrated in large graupel particles, and this feature is more pronounced under the high CCN concentration than under the low CCN concentration. By TICE, although the number-averaged mean radius of graupel particles increases, the mass-averaged mean radius of graupel particles decreases (42% in TU500 and 15% in TU4000). The portion of the total graupel mass

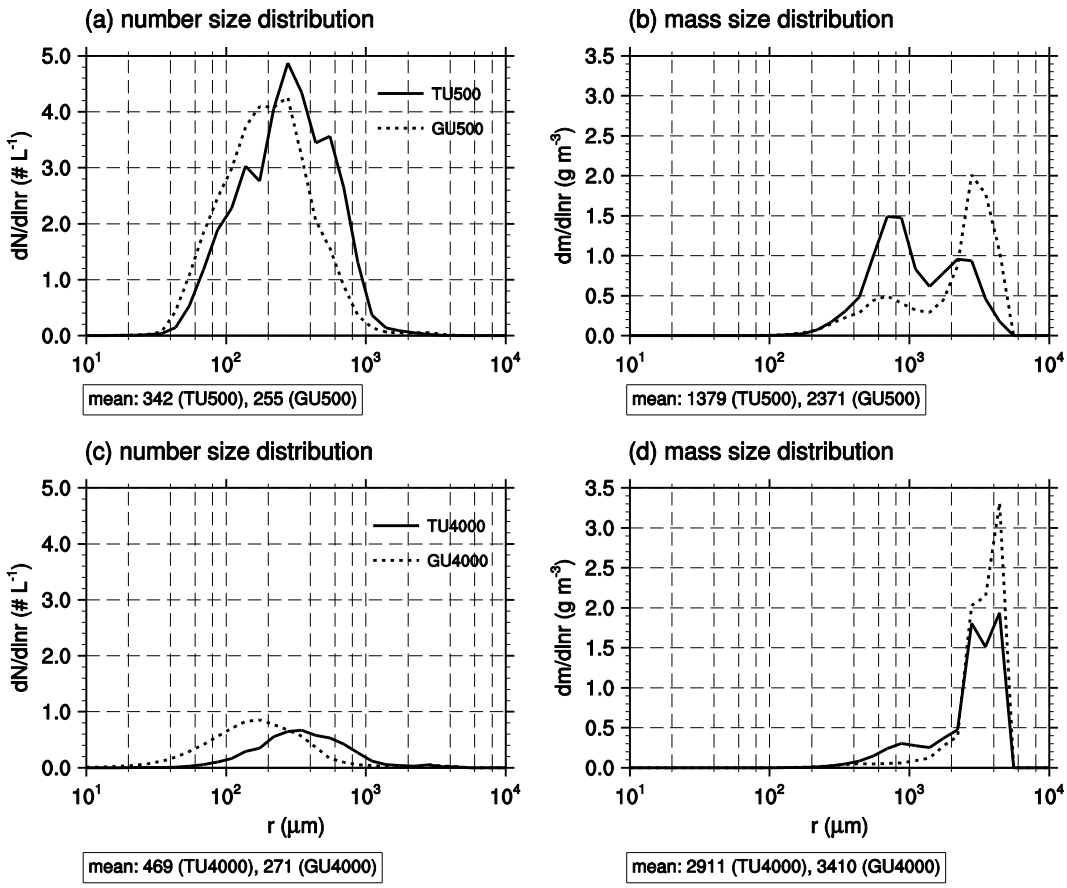

Figure 4.5 (a) Number size distributions and (b) mass size distributions of graupel particles averaged over the cloud core area (marked with the rectangular box in Fig. 4) for t = 130–150 min in TU500 and GU500. (c) and (d) are the same as (a) and (b) but for TU4000 and GU4000. The number- or mass-averaged mean radius of the graupel particles is given in each figure.

occupied by very large graupel particles with radii larger than 2 mm decreases significantly when TICE is considered. This means that when TICE is not considered, a very small number of large graupel particles occupy almost all the total graupel mass. However, when TICE is considered, small graupel particles also occupy some portion of the total graupel mass. The decrease in the mass-averaged mean radius of graupel particles is more marked under the low CCN concentration. This is because under the low CCN concentration, the supersaturation is higher so the increase in the number of small graupel particles by TICE is greater.

Figure 4.6 shows the vertical profiles of vertical flux of graupel mass, mass-averaged mean terminal velocity of graupel particles, and vertical wind velocity averaged for t = 130–150 min in TU500, GU500, TU4000, and GU4000. The vertical flux of graupel mass is affected by graupel terminal velocity, vertical wind velocity, and graupel mass. In all cases, the averaged vertical wind velocity is negative (toward the ground) in the layer z < 4.5 km. Also, the vertical flux of graupel mass is downward in the layer z < 7 km, and TICE decreases the downward flux of graupel mass. It is seen that the difference in vertical wind velocity in the lower layer between the cases with and without TICE is small, so it can make little difference in vertical flux of graupel mass. In TU500 and GU500, the large decrease in mass-averaged mean radius of graupel particles by TICE (Fig. 4.5b) results in a decrease in terminal velocity of graupel particle and thus the decrease in downward flux of graupel mass. In TU4000 and GU4000, however, the decrease in mass-averaged mean terminal velocity by TICE is comparatively small because the decrease in mass-averaged mean radius of graupel particles is

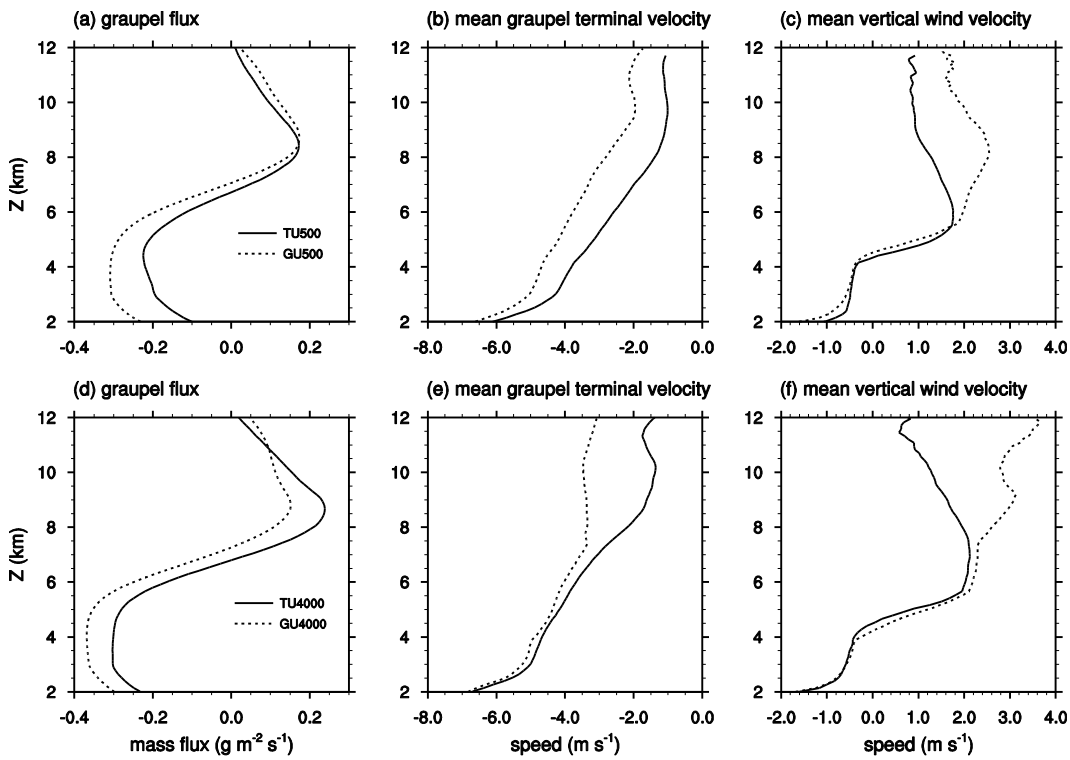

Figure 4.6 Vertical profiles of (a) vertical flux of graupel mass, (b) mass-averaged mean terminal velocity of graupel particles, and (c) vertical wind velocity averaged for t = 130–150 min in TU500 and GU500. The terminal velocity and the vertical wind velocity are averaged over the region where the graupel mass is larger than 0.1 g m^{-3}. (d)–(f) are the same as (a)–(c) but for TU4000 and GU4000. Positive and negative values mean upward and downward, respectively.

small (Fig. 4.5d).

Figure 4.7 shows the vertical profiles of temperature change rate due to the latent heat from sublimation, riming, and melting averaged for t = 130–150 min in TU500, GU500, TU4000, and GU4000. Figure 4.7a indicates that under the low CCN concentration, the sublimation of ice particles increases by TICE. Although an increase in ice particle mass due to riming is also seen in Fig. 4.7b, the decrease in ice particle mass due to sublimation is larger than the increase in ice particle mass due to riming. However, such an increase in sublimation is not seen under the high CCN concentration (Fig. 4.7d). Therefore, it can be concluded that the decrease in graupel mass in the low altitudes when TICE is considered is more likely to come from the decrease in downward flux of graupel mass, rather than from the increase in sublimation. The melting of ice particles decreases by TICE regardless of the CCN concentration.

4.3. Sheared basic-state wind cases

Analyses similar to those for the uniform basic-state wind cases are conducted for the sheared basic-state wind cases. The vertical profiles of mass distribution of each hydrometeor type for the sheared basic-state wind cases are shown in Figs. 4.8 and 4.9. The important features also appear in the sheared basic-state wind cases. TICE accelerates collisions between small droplets, so cloud water mass decreases and rainwater mass increases in the early stage (t = 100–120 min). For t = 160–180 min, as that in the uniform basic-state wind cases, graupel particles comprise a large portion of clouds, followed by rainwater and plate-type ice crystals. By comparing TS500 to GS500, it is seen that graupel mass in the layer

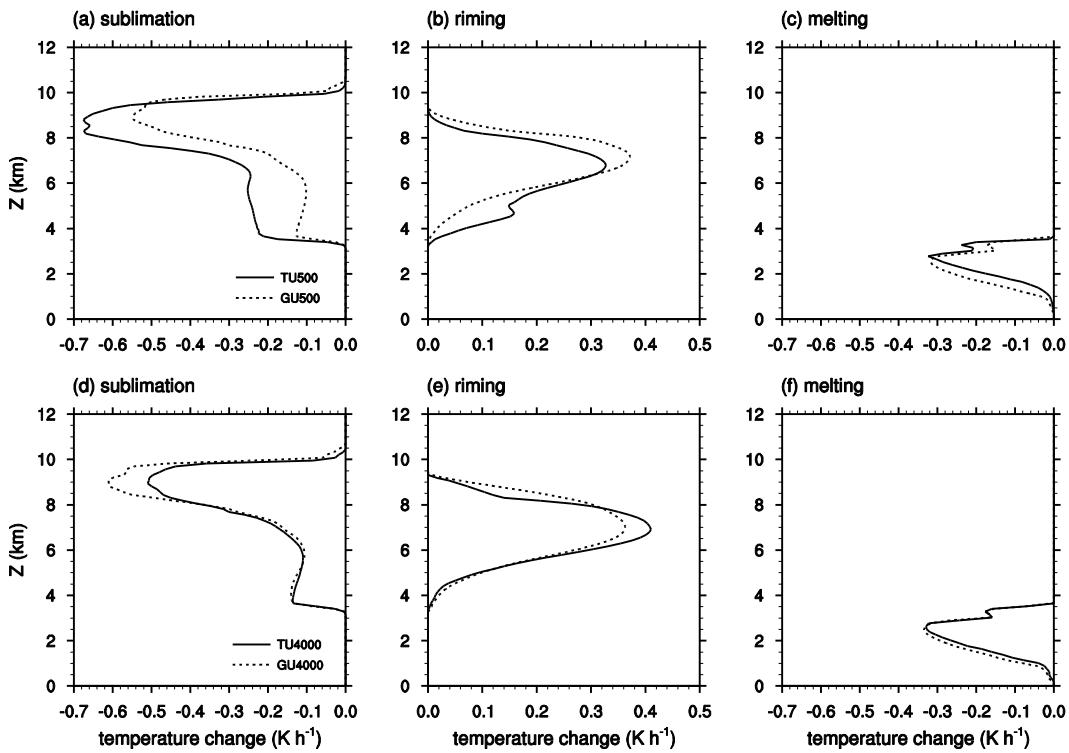

Figure 4.7 Vertical profiles of temperature change rate due to the latent heat from (a) sublimation, (b) riming, and (c) melting averaged over the domain for t = 130–150 min in TU500 and GU500. (d)–(f) are the same as (a)–(c) but for TU4000 and GU4000.

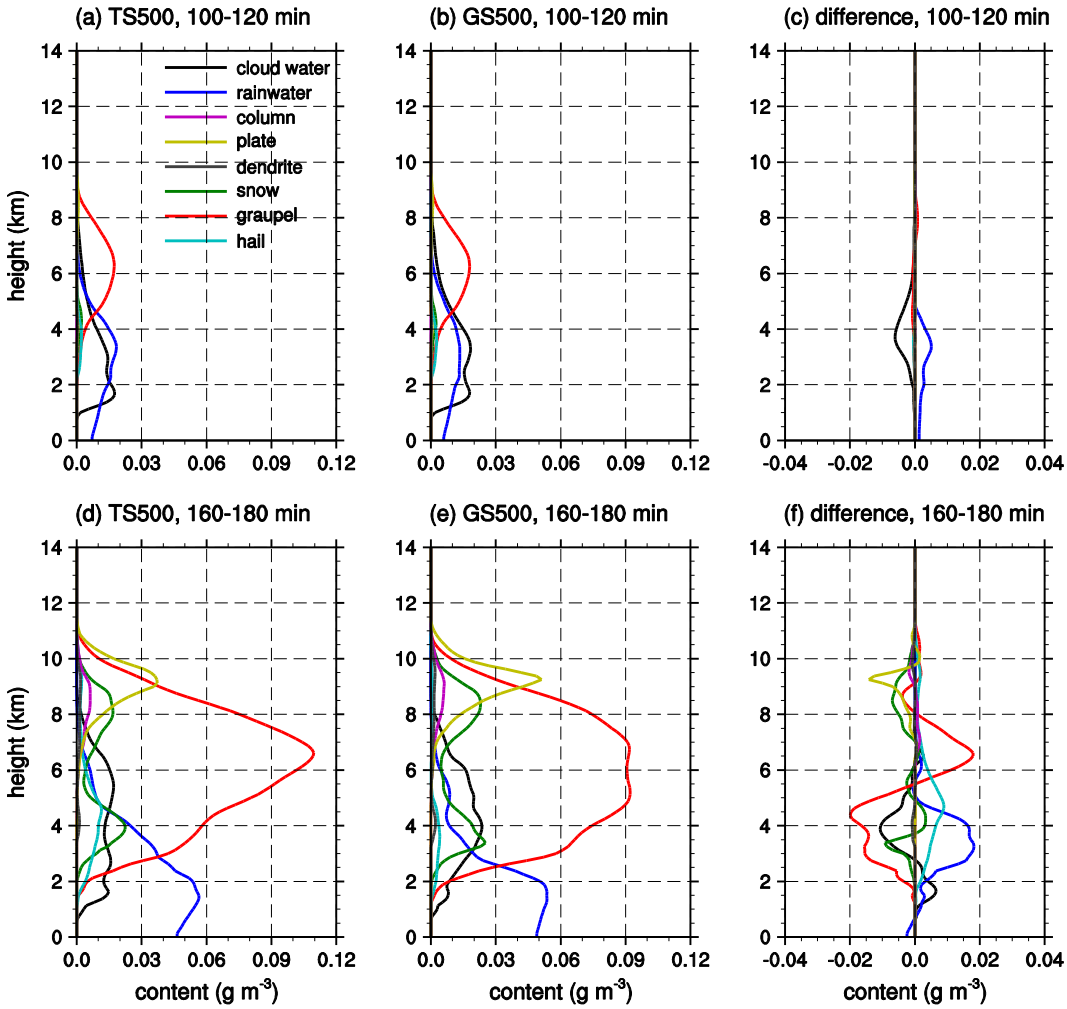

Figure 4.8 Vertical profiles of mass distribution of each hydrometeor type averaged for t = 100–120 min in (a) TS500 and (b) GS500. (c) is the difference between (a) and (b). (d)–(f) are the same as (a)–(c) but averaged for t = 160–180 min.

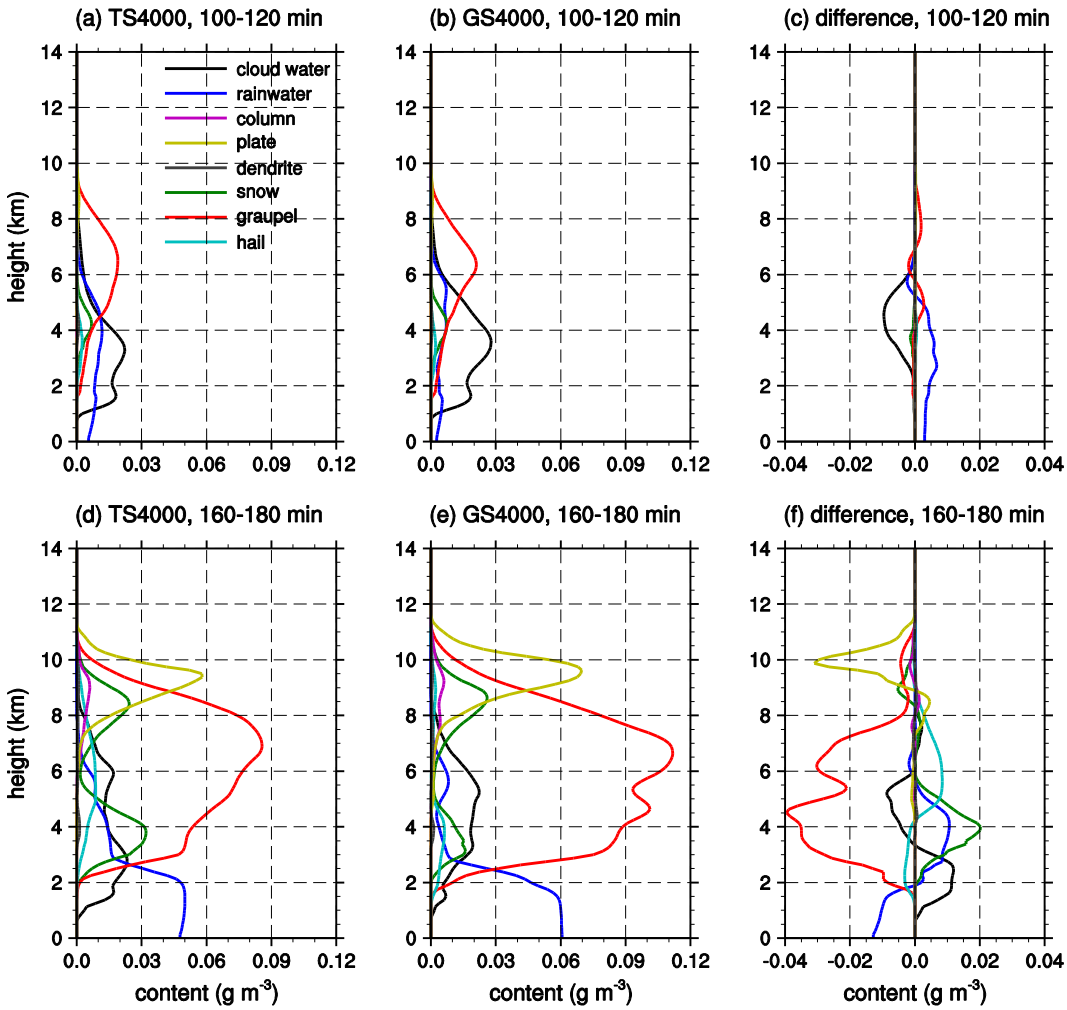

Figure 4.9 As in Fig. 4.8 but for TS4000 and GS4000.

z > 5.5 km increases, but graupel mass in the layer z < 5.5 km decreases (Fig. 4.8f). The decrease in graupel mass appears differently in TS4000 and GS4000: graupel mass reduces in the entire layer by TICE (Fig. 4.9f). A decrease in rainwater mass in the layer z < ~1 km is seen under both the low and the high CCN concentration.

There are also some noticeable differences in the distribution when compared to that in the uniform basic-state wind cases. One of these is a decrease in ice crystal mass near the cloud top. Strong vertical wind shear enhances mixing of the cloud with the surrounding dry air. The amount of cloud water and water vapor decrease, and updraft velocity weakens by the enhanced mixing in the early stage of cloud development. Therefore, the growth of ice crystals in the high altitudes slows. Snow mass is not negligible in the sheared basic-state wind cases. This is also one of the differences compared to the uniform basic-state wind cases. Strong wind shear can advect small droplets to unsaturated areas, so the droplets are more likely to evaporate. This decrease in cloud droplets (Figs. 4.8 and 4.9 compared to Figs. 4.2 and 4.3) gives rise to the lack of necessary sources for growing ice crystals into ice particles with relatively high densities. Thus, graupel mass decreases, whereas snow mass increases.

The spatial distribution fields of graupel mass averaged for t = 160–180 min in TS500, GS500, TS4000, and GS4000 are shown in Fig. 4.10. Comparing to the spatial distribution fields of graupel mass in the uniform basic-state wind cases, graupel mass in the cloud core area decreases by about half, and graupel particles spread across a far wider area. Although Figs. 4.8f and 4.9f also show a decrease in graupel mass by TICE in the low altitudes, distribution patterns are different: the narrow shaft area that is seen in the uniform basic-state wind cases

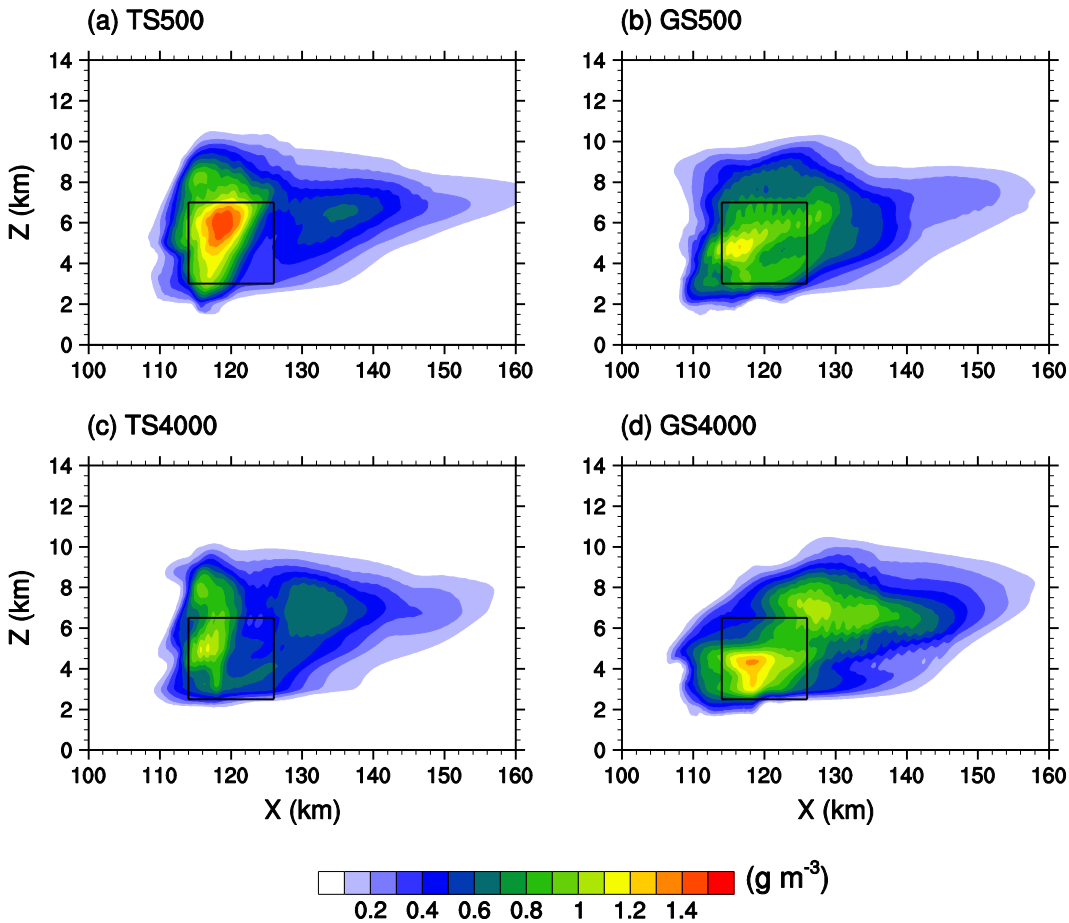

Figure 4.10 Spatial distribution fields of graupel mass averaged for t = 160–180 min in (a) TS500, (b) GS500, (c) TS4000, and (d) GS4000. The rectangular box indicates the cloud core area.

(Figs. 4.4b and 4.4d) does not appear in Figs. 4.10b and 4.10d. Rather, graupel mass in the cloud core area is distributed more uniformly when TICE is not considered.

The number and mass size distributions of graupel particles in the cloud core area in TS500, GS500, TS4000, and GS4000 are plotted in Fig. 4.11. This figure shows some features that are different from those in the uniform basic-state wind cases. In the number size distribution, the range of the radii of graupel particles is almost the same and it is only the concentration that changes by TICE, whereas a shift is seen in the uniform basic-state wind cases. In the mass size distribution, the mass-averaged mean radius of graupel particles increases slightly when TICE is considered. This is opposite to the behavior in the uniform basic-state wind cases. The difference in the mass size distributions between the cases with and without TICE is very small. In the uniform basic-state wind cases, the faster growth of ice crystals into small graupel particles by TICE is the key to the differences in the number and mass size distributions of graupel particles. In the sheared basic-state wind cases, however, the number of ice crystals is much smaller than in the uniform basic-state wind cases, so the size distributions in the cases with and without TICE show little difference.

Figure 4.12 shows the vertical profiles of vertical flux of graupel mass, mass-averaged mean terminal velocity of graupel particles, and vertical wind velocity averaged for t = 160–180 min in TS500, GS500, TS4000, and GS4000. The overall difference in downward flux of graupel mass in the lower layer between the cases with and without TICE is small compared to that in the uniform basic-state wind cases. Comparing TS500 to GS500, a small decrease in mass-

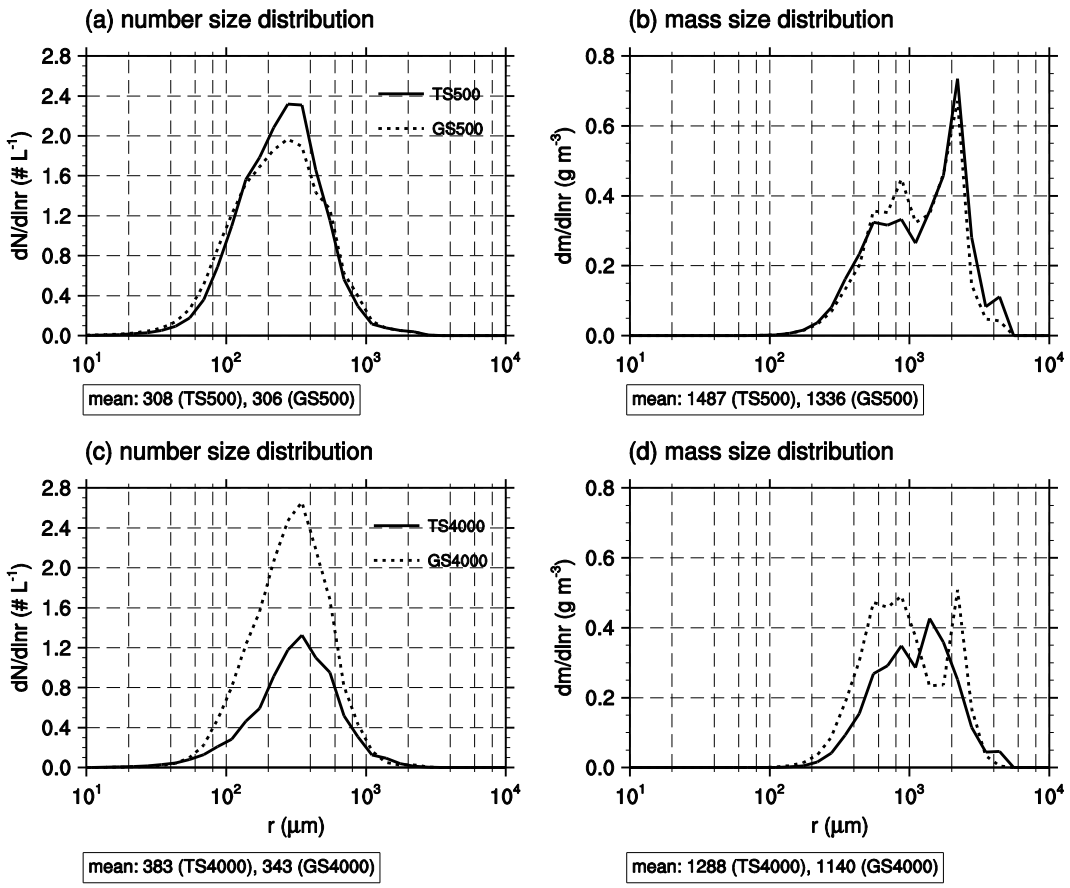

Figure 4.11 (a) Number size distributions and (b) mass size distributions of graupel particles averaged over the cloud core area (marked with the rectangular box in Fig. 4.10) for t = 160–180 min in TS500 and GS500. (c) and (d) are the same as (a) and (b) but for TS4000 and GS4000. The number- or mass-averaged mean radius of the graupel particles is given in each figure.

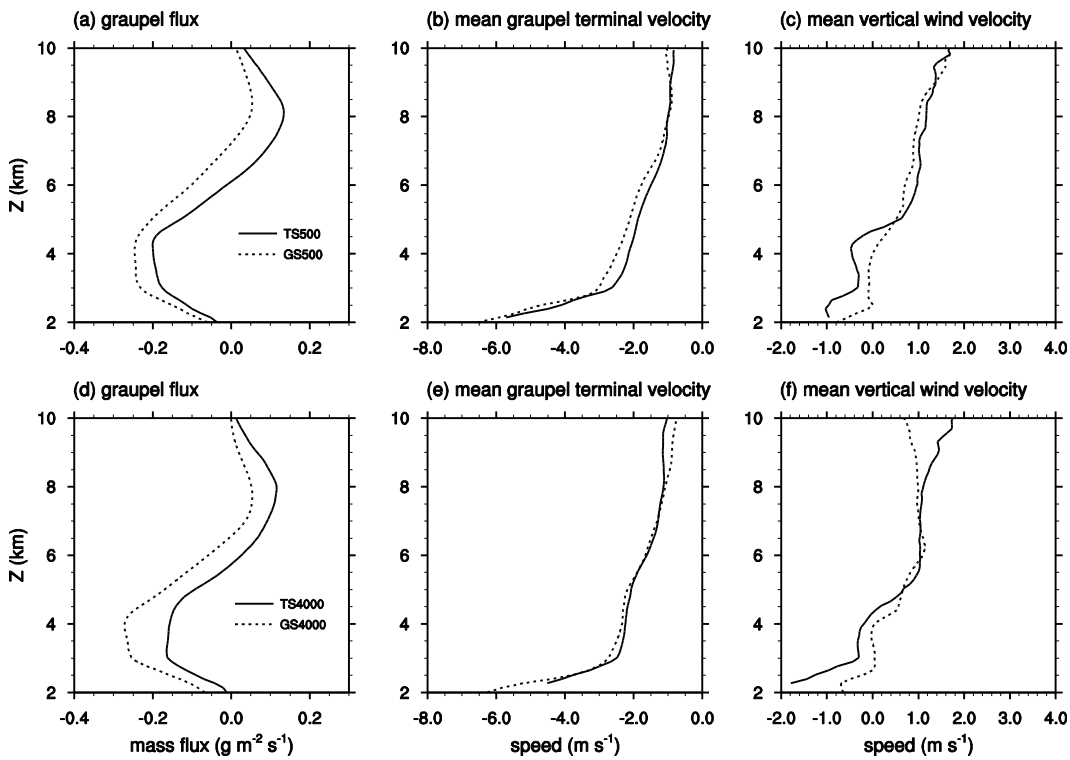

Figure 4.12 Vertical profiles of (a) vertical flux of the graupel mass, (b) mass-averaged mean terminal velocity of graupel particles, and (c) vertical wind velocity averaged for t = 160–180 min in TS500 and GS500. The terminal velocity and the vertical wind velocity are averaged over the region where the graupel mass is larger than 0.1 g m^{-3}. (d)–(f) are the same as (a)–(c) but for TS4000 and GS4000. Positive and negative values mean upward and downward, respectively.

averaged mean terminal velocity of graupel particles is seen. However, this would be cancelled out by the enhanced downdraft. Similar to the uniform basic-state wind cases, the difference in mean terminal velocity between the cases with and without TICE is smaller under the high CCN concentration than under the low CCN concentration. The mean terminal velocities of graupel particles in TS4000 and GS4000 are very similar. The decrease in vertical flux of graupel mass might come from the decrease in graupel mass (Fig. 4.9).

Figure 4.13 shows the vertical profiles of temperature change rate due to the latent heat from sublimation, riming, and melting averaged for t = 160–180 min in TS500, GS500, TS4000, and GS4000. The most striking difference compared to that in the uniform basic-state wind cases is an increase in sublimation of ice particles in the layer 4 km < z < 6 km. In this layer, ice sublimation in the sheared basic-state wind cases increases more than two times than that in the uniform basic-state wind cases. Strong wind shear makes more ice particles fall into unsaturated areas. Increased ice sublimation compared to that in the uniform basic-state wind cases is seen in all the periods of the numerical simulations, not only for t = 160–180 min.

4.4. Surface precipitation

Time series for the surface precipitation rate and the amount of accumulated surface precipitation in all simulation cases are depicted in Fig. 4.14. Surface precipitation is strongly affected by the vertical wind shear. The amount of accumulated surface precipitation in the sheared basic-state wind cases reduces by about 35% compared to that in the uniform basic-state wind cases, which is

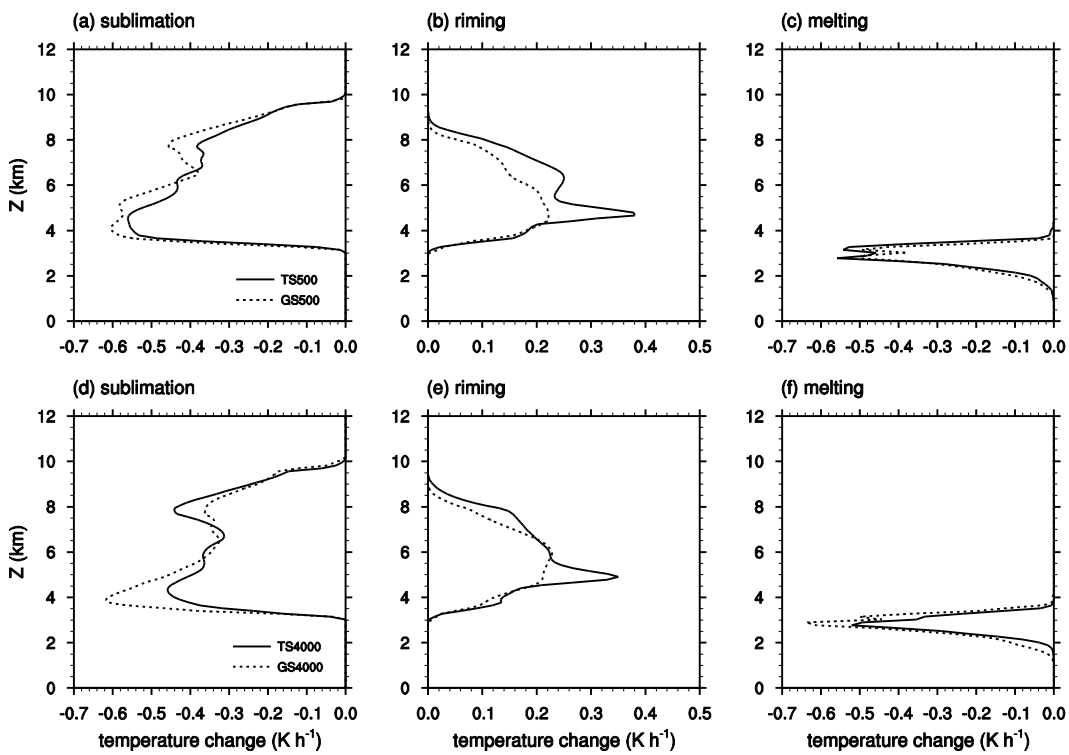

Figure 4.13 Vertical profiles of temperature change rate due to the latent heat from (a) sublimation, (b) riming, and (c) melting averaged over the domain for t = 160–180 min in TS500 and GS500. (d)–(f) are the same as (a)–(c) but for TS4000 and GS4000.

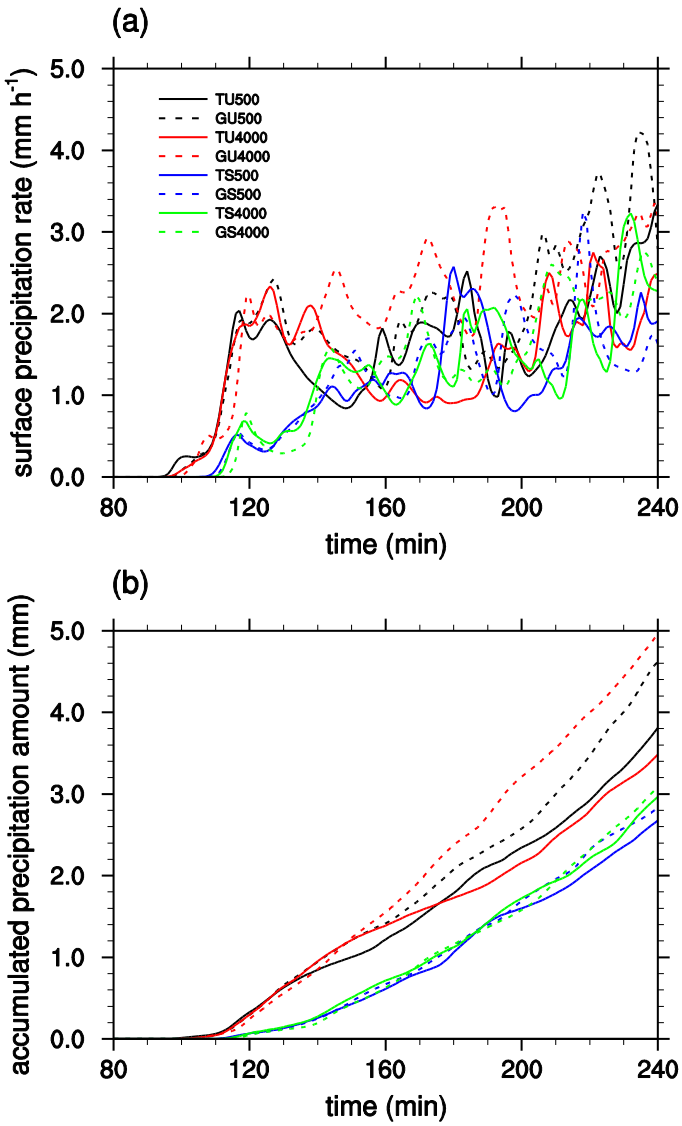

Figure 4.14 Time series for (a) the surface precipitation rate and (b) the amount of accumulated surface precipitation averaged over the domain in all simulation cases.

expected to be the result of the increased ice sublimation (Figs. 4.13a and 4.13d). By TICE, surface precipitation starts about 5 min earlier in all cases, which is a well-known TICE effect (Seifert et al., 2010; Benmoshe et al., 2012; Wyszogrodzki et al., 2013). In spite of the accelerated onset of surface precipitation, however, the amount of accumulated surface precipitation decreases by TICE in all cases. For example, the amount of accumulated surface precipitation decreases by 18% in TU500 compared to GU500 during the simulation period. This result largely agrees with the result of Benmoshe et al. (2012) in which the amount of surface precipitation always decreases regardless of aerosol concentrations. The decrease in the amount of surface precipitation is larger in the uniform basic-state wind cases than in the sheared basic-state wind cases. This is mainly because of the changes in the size distributions of graupel particles. This is examined in Section 4.2. In the uniform basic-state wind cases, the decrease in the amount of surface precipitation is larger under the high CCN concentration than under the low CCN concentration. Although the decrease is also seen in the sheared basic-state wind cases, it is so small that the comparison between the low and the high CCN concentration case seems unnecessary. Note that in the uniform basic-state wind cases, the amount of accumulated surface precipitation over the simulation period increases with increasing CCN concentration when TICE is not considered, whereas the opposite trend appears when TICE is considered.

5. Effects of turbulence on warm cloud properties

5.1. Experimental setup

The thermodynamic sounding in Ogura and Takahashi (1973) is adopted in this study with slight modifications above the inversion layer (Fig. 1). A strong temperature inversion layer is lain on z = 3–3.4 km, where the temperature is ~ 6℃. The basic-state wind is set to be calm in the entire model domain to track the simulated clouds more easily (Wang and Feingold, 2009). A constant surface heat flux of 1.2×10^{-2} K m s^{-1} and a constant surface water vapor flux of 3.4×10^{-5} m s^{-1} (approximately 15 and 100 W m^{-2}, respectively) are applied for bottom boundary conditions. The surface friction velocity is set to 0.25 m s^{-1}. Large-scale subsidence is provided at each model level using a uniform horizontal divergence of 3.75×10^{-6} s^{-1} multiplied by the altitude (Wang and Feingold, 2009). The subsidence velocity at higher altitudes is limited to 0.5 m s^{-1} (vanZanten et al., 2011). A random perturbation of [–0.3 K, 0.3 K] is added to the initial potential temperature field at the lowest 4 levels of the model domain. The Coriolis parameter is 10^{-4} s^{-1}.

The initial aerosol size distribution is set to follow the Twomey equation (Twomey, 1959), the same as in Khain et al. (2000) and Section 3. The aerosol number concentration is set for the CCN number concentration at 1% supersaturation (N_0) to be 30, 300, and 3000 cm^{-3}. Six numerical experiments (T30, G30, T300, G300, T3000, and G3000) are conducted according to the collision kernel type (‘T’ and ‘G’ denote the turbulent and gravitational collision

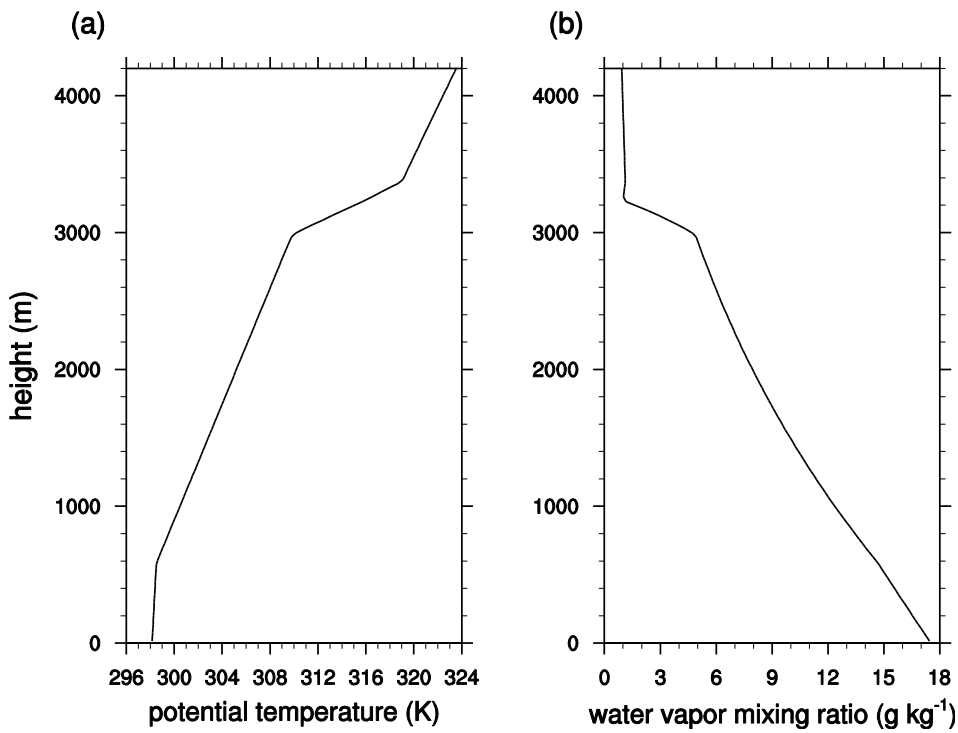

Figure 5.1 Vertical profiles of the initial (a) potential temperature and (b) water vapor mixing ratio used in this study, which are slightly modified from those of Ogura and Takahashi (1973).

kernel, respectively.) and the aerosol number concentration (N_0 of 30, 300, and 3000 cm^{-3}). The aerosol number concentration is constant below z = 2 km and decreases exponentially with height above z = 2 km with an e-folding depth of 2 km. The aerosol replenishment scheme proposed by Jiang and Wang (2014) is adopted with a time scale of 1 h.

The domain size is 18 × 18 × 4.2 km^3. Periodic boundary conditions are applied in both the x and y directions. The grid size is 100 m in the horizontal and 30 m in the vertical. The horizontal grid size might be considered somewhat larger than that used in typical LES studies. However, some studies have shown that the properties of shallow clouds and the effects of turbulence on the clouds are well captured with this grid size or even larger grid sizes (Wang and Feingold, 2009; Feingold et al., 2010; Seifert et al., 2010; Franklin, 2014). The integration period is 12 h, from 6 p.m. to 6 a.m. of the next day. The time step is 1 s except for the vapor diffusion process (0.5 s).

5.2. Precipitation

Figure 5.2 shows the time series of liquid water path (LWP), rainwater path (RWP), accumulated surface precipitation, and surface precipitation rate for all simulation cases. LWP and RWP are averaged over cloudy columns where LWP > 10 g m^{-2}, and the quantities related to precipitation are averaged over the entire domain. Cloud droplets and raindrops are distinguished using a radius threshold of 50 μm.

First, the aerosol effects on LWP are seen in Fig. 5.2a. Increasing the aerosol concentration tends to increase LWP mainly due to the suppressed

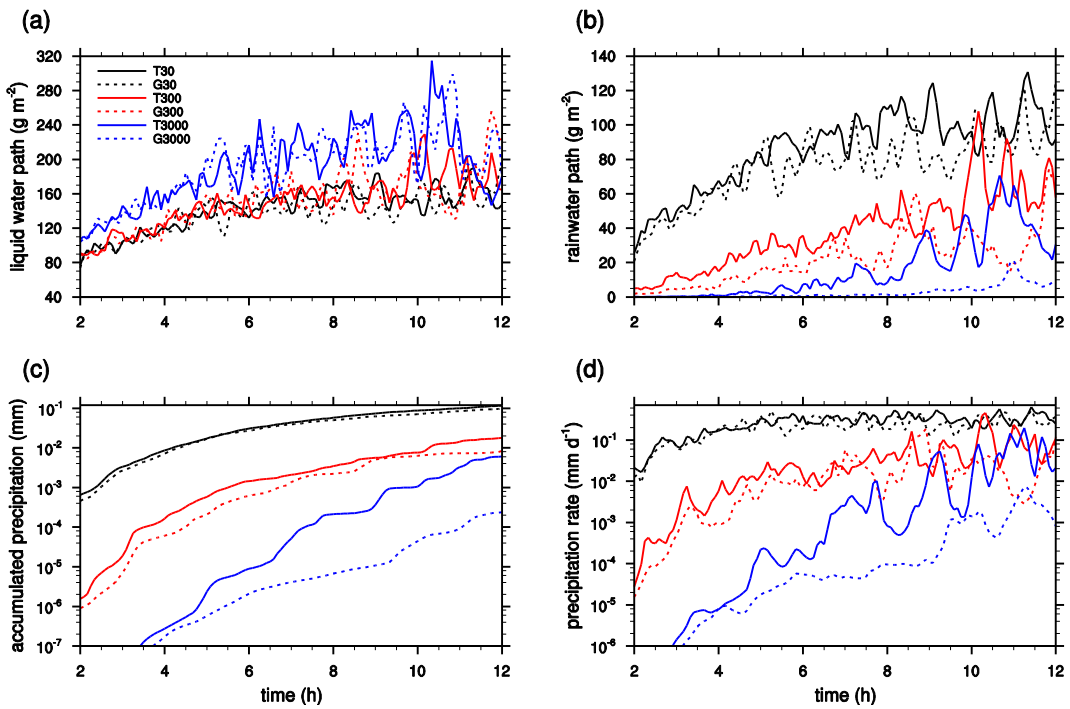

Figure 5.2 Time series of (a) cloud-averaged liquid water path, (b) cloud-averaged rainwater path, (c) domain-averaged accumulated surface precipitation, and (d) domain-averaged surface precipitation rate. Cloudy columns are defined using a liquid water path threshold of 10 g m^{-2}.

precipitation and increased condensation. These contributions of suppressed precipitation and increased condensation to LWP dominate over a probable decrease in cloud water due to the increased evaporation caused by decreased drop size. The effects of TICE on LWP are smaller than those of aerosols, so they are hard to clarify. These small changes in LWP due to TICE largely agree with those of previous studies (e.g., Seifert et al. 2010; Section 3 of this study).

In contrast to LWP, TICE clearly impacts on RWP and precipitation. TICE increases RWP by approximately 10–20 g m^{-2} for all aerosol concentrations (Fig. 5.2b) simply because TICE enhances the growth of small droplets to large drops. This increase in RWP tends to be apparent after a few hours (approximately 4–6 hours) of model integration. This distinct increase in RWP due to TICE, in contrast to the negligible changes in LWP, implies that TICE mainly changes the fractions of cloud droplets and raindrops in the clouds, but the total amount of liquid water in the clouds is not largely affected by TICE.

The surface precipitation increases and its onset is accelerated due to TICE for all aerosol concentrations (Figs. 5.2c and 5.2d), which is in line with the increase in RWP. However, the increase in surface precipitation for N_0 = 30 cm^{-3} is not statistically significant. The increase in surface precipitation, as well as the acceleration of the first onset of surface precipitation becomes larger as the aerosol concentration increases. This is consistent with the result in Section 3, in which the involved mechanism is suggested as follows: when the aerosol concentration is relatively small and the environment is humid, small droplets can grow to large size via vapor diffusion in a rich pool of water vapor. However, turbulence effectively enhances the collision only between small droplets (e.g.,

Grabowski and Wang, 2013), whose radii are less than 20 μm in this model. Therefore, the difference in the amount of precipitation due to TICE is comparatively small. However, when the aerosol concentration is relatively large, small droplets are difficult to grow to sufficiently large drops, and further growth via collision is restrained. Under this condition, TICE can efficiently work so the surface precipitation is enhanced due to TICE. In RWP and surface precipitation, the effects of TICE tend to be opposite to the effects of aerosols, which agrees with the results of Benmoshe et al. (2012) and Section 3 of this study.

Figure 5.3 depicts the vertical distributions of cloud droplet radius, cloud droplet number concentration, rainwater content, and rainwater flux averaged over the last 3 h of the integration and over the cloudy grid points where liquid water content (LWC) > 0.01 g kg^{-1}. This figure shows more detail regarding the effects of TICE on the growth of small droplets to large drops. In the vertical distribution of mean cloud droplet radius, the mean radius tends to increase with height in all cases mainly due to the particularly significant activation process near the cloud base, which is commonly found in observational and modeling studies (e.g., Arabas and Shima, 2013). This feature becomes more apparent with higher aerosol concentration because the droplet radius near the cloud base decreases as the aerosol concentration increases. TICE is definitely effective in increasing the mean cloud droplet radius, and the effect is more pronounced with higher aerosol concentration. When N_0 = 30 cm^{-3}, the mean cloud droplet radius above z ~ 1 km reaches approximately 20 μm in the case without TICE. Therefore, the effects of TICE, which acts on the small droplets whose radii are less than 20 μm, become small. In contrast, when N_0 = 3000 cm^{-3}, the mean cloud droplet radius at z ~ 2.5

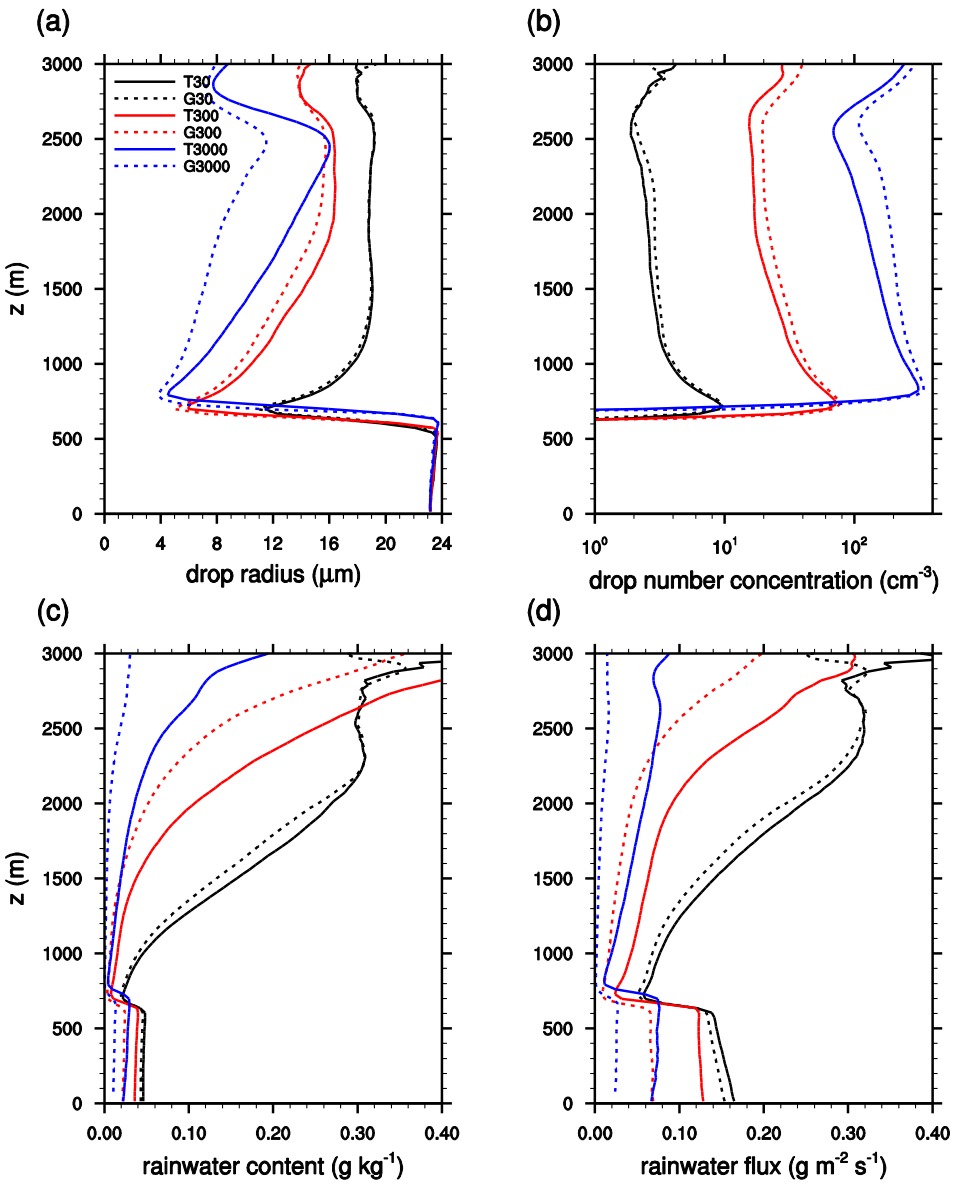

Figure 5.3 Vertical profiles of (a) cloud droplet radius, (b) cloud droplet number concentration, (c) rainwater content, and (d) rainwater flux averaged over cloudy grids, where liquid water content exceeds 0.01 g kg^{-1}, and the last 3 h.

km is ~ 11 μm in the case without TICE but it increase by approximately 50% (up to ~ 16 μm) due to TICE. The vertical distribution of cloud droplet number concentration also supports the same conclusion as that of the cloud droplet radius. TICE decreases the mean cloud droplet number concentration because the accelerated collision decreases the cloud droplet number concentration more rapidly. These effects are also more distinct with higher aerosol concentration.

TICE increases the rainwater content in all cases. The increase in rainwater content is comparatively small when N_0 = 30 cm^{-3}, and the increase becomes larger as the aerosol concentration increases. The differences in rainwater content in the cloud layer are large, while the absolute values and the differences in rainwater content in the sub-cloud layer are relatively small mainly due to evaporation. In the sub-cloud layer, differences in rainwater flux (product of the rainwater content and the raindrop terminal velocity) are larger than those in rainwater content. Therefore, this shows that the terminal velocity, which increases with increasing raindrop radius, also increases due to TICE, and the increase in surface precipitation induced by TICE depends not only on the increase in rainwater content but also on the increase in raindrop radius and terminal velocity.

Drop size distributions at certain selected levels are shown in Fig. 5.4. The effects of TICE on the drop size distribution are easily observed at all levels. The differences due to TICE become smaller as the altitude is closer to the cloud base because the clouds at this level consist mainly of nucleated small droplets and the turbulence intensity is relatively weak near the cloud base (Fig. 5.7; Seifert et al., 2010; Section 3 of this study). When N_0 = 30 cm^{-3}, the effects of TICE on the

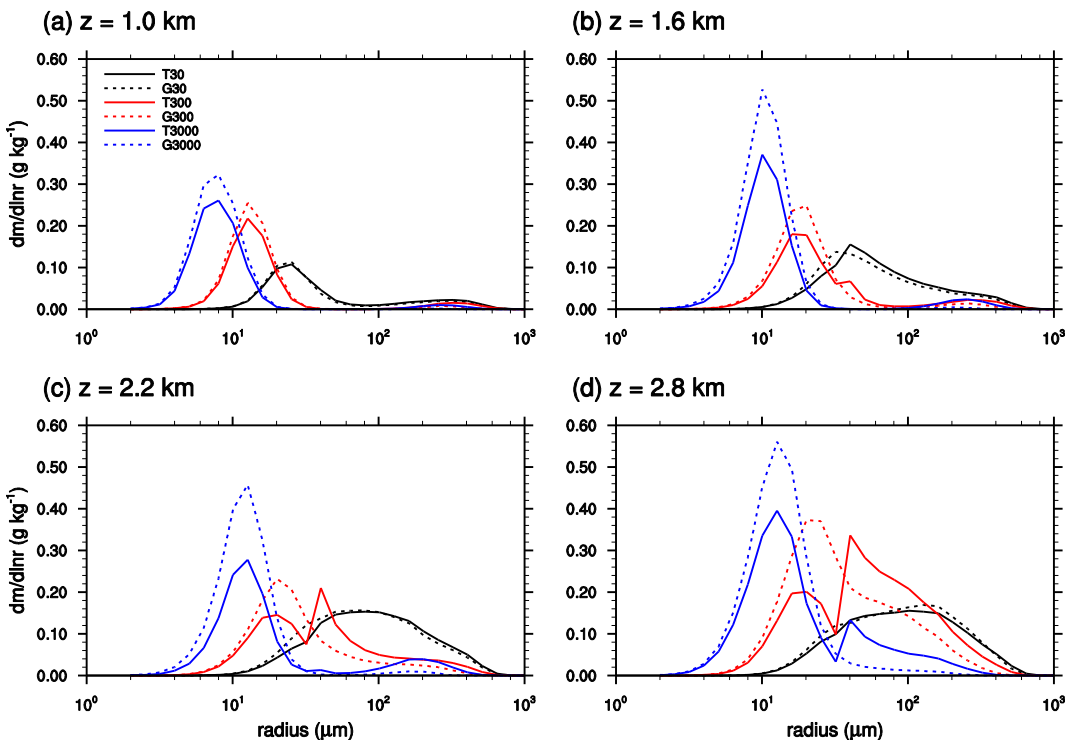

Figure 5.4 Drop size distributions at z = (a) 1.0, (b) 1.6, (c) 2.2, and (d) 2.8 km averaged over cloudy grids and the last 3 h.

drop size distribution is relatively small. When N_0 = 300 and 3000 cm^{-3}, TICE little changes the peak position in small droplet radius but decreases the number of small droplets considerably. Moreover, TICE creates another peak position in large drop radius at the upper levels; the drop size distribution has a bimodal form due to TICE. On the other hand, the drop size distribution tends to remain unimodal when TICE is not considered. It is noted that the effects of aerosol concentration on the drop size distribution appear to shift the peak position in small drop radius and the form of the drop size distribution remains unimodal. Therefore, the effects of TICE on the drop size distribution contrast with the effects of aerosol concentration, although the effects of TICE and those of decreasing aerosol concentration appear similarly in the cloud macroproperties (Figs. 5.2 and 5.3; Benmoshe et al., 2012; Section 3 of this study).

5.3. Cloud dynamics and morphology

As previously stated, the basic effect of TICE on the clouds is to increase the mean drop radius by reducing the number of small droplets and increasing the number of large drops. The effect is expected to induce changes in cloud dynamical properties by altering latent heat release and buoyancy.

Figure 5.5 shows the vertical profiles of condensational heating and evaporative cooling rates. The condensational heating is generally larger than the evaporative cooling at almost all levels, but the effects of TICE on condensational heating are relatively small and are not consistent across all cases. When N_0 = 3000 cm^{-3}, TICE generally enhances the condensational heating in most of the cloud layer and reduces it near the cloud top, whereas the effects of TICE on the

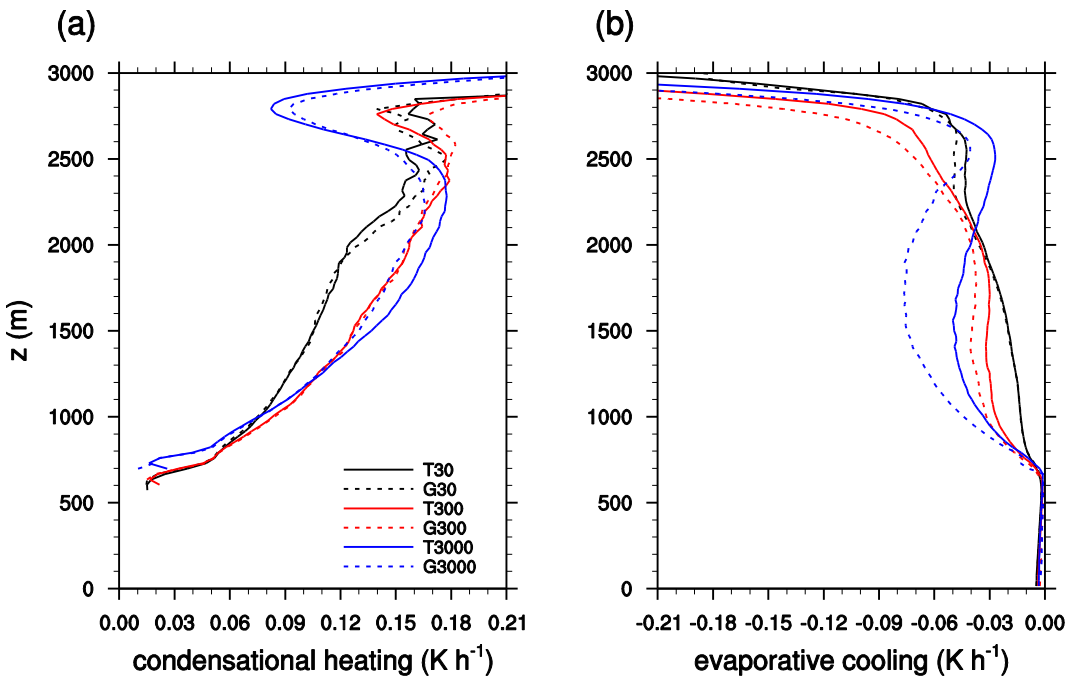

Figure 5.5 Vertical profiles of (a) condensational heating rate and (b) evaporative cooling rate averaged over the cloudy grids and the last 3 h.

condensational heating are not distinct when N_0 = 30 and 300 cm^{-3}. On the other hand, the effects of TICE on the evaporative cooling appear consistently in all aerosol concentrations. The evaporative cooling decreases due to TICE, particularly in the cloud layer. This decrease is mainly due to the increased mean drop radius. If the total liquid water content is constant, the large mean drop radius reduces the sum of the drop radii. Therefore, the evaporative cooling, which is proportional to the sum of the drop radii, decreases due to TICE. In the sub-cloud layer, the evaporative cooling and its decrease due to TICE are not distinct.

This decrease in evaporative cooling results in an increase in cloud size because most evaporation occurs near the cloud edges (e.g., Xue and Feingold, 2006). Figure 5.6a shows the time series of cloud fraction. TICE increases cloud fraction, and this increase is more distinct as the aerosol concentration increases. It is also possible that TICE may decrease cloud fraction because of the increased downward flux of raindrops and precipitation (Figs. 5.2 and 5.3). However, the decrease in evaporation dominates over the increase in precipitation for the changes in cloud fraction.

Figures 5.6b–d show the time series of mean vertical velocity, maximum vertical velocity, and cloud top height. It is possible that the decrease in evaporative cooling due to the increased mean drop radius can affect cloud dynamics, such as the vertical velocity or cloud top height. In these figures, however, only the mean vertical velocity for relatively high aerosol concentrations is affected by TICE. The mean vertical velocity is positive in all cases (Fig. 5.6b), and the mean vertical velocity decreases due to TICE for N_0 = 300 cm^{-3} and 3000

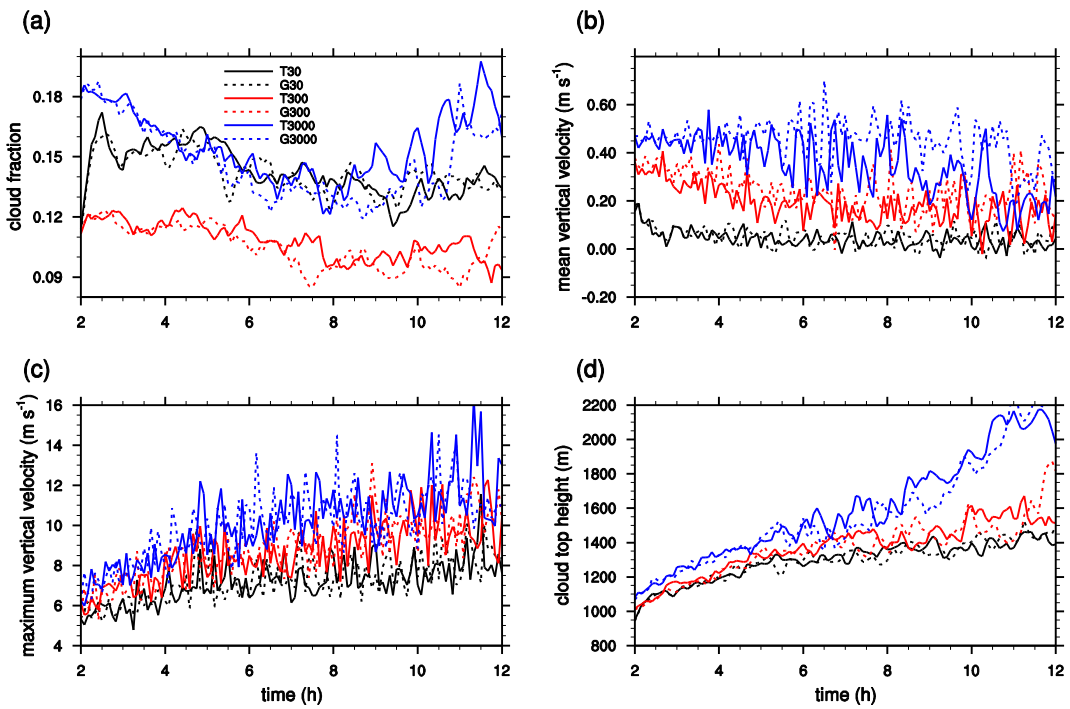

Figure 5.6 Time series of (a) cloud fraction, (b) mean vertical velocity in the domain, (c) maximum vertical velocity, and (d) cloud top height. (b) and (d) are obtained from the average over the cloudy grids and the cloudy columns, respectively.

cm^{-3}. This decrease is mainly due to the decrease in evaporative cooling. The decreased evaporative cooling occurs mainly in the cloud layer, and it is hardly seen in the sub-cloud layer (Fig. 5.5b). Therefore, the atmosphere becomes more stable, so the mean vertical velocity is reduced. However, the maximum vertical velocity and the cloud top height are hardly affected by TICE, partially due to small changes in condensational heating (Fig. 5.5a). Wyszogrodzki et al. (2013) and Grabowski et al. (2015) noted that the cloud top height is raised by TICE due to the decreased hydrometeor drag in relatively shallow (cloud depth of ~ 1 km) warm clouds developing in the inversion-free atmosphere. However, Franklin (2014) showed that the increase in cloud top height is comparatively small (less than 10 m in average) in relatively deep (cloud depth of ~ 2 km) warm clouds. In this study, the cloud depth is approximately 2 km (Fig. 5.1), and the change in cloud top height is also small.

Figure 5.7 shows the vertical profiles of the variance of vertical velocity, the third moment of vertical velocity (w^3), turbulent kinetic energy (TKE), and buoyancy (the value of buoyancy term in the TKE equation) averaged over the entire domain. While the variance of vertical velocity, TKE, and buoyancy profiles show shapes overall similar to those of Franklin (2014), certain differences also exist. In this study, it is shown that TICE decreases TKE; therefore, the effects of TICE produce a negative feedback. This result is similar to that of Franklin (2014) and is different from that of Wyszogrodzki et al. (2013) which reported a positive feedback of turbulence effects. Unlike the case of Franklin (2014), the decrease in buoyancy is not the reason for the decrease in TKE because the buoyancy increases due to TICE in this study. Therefore, the

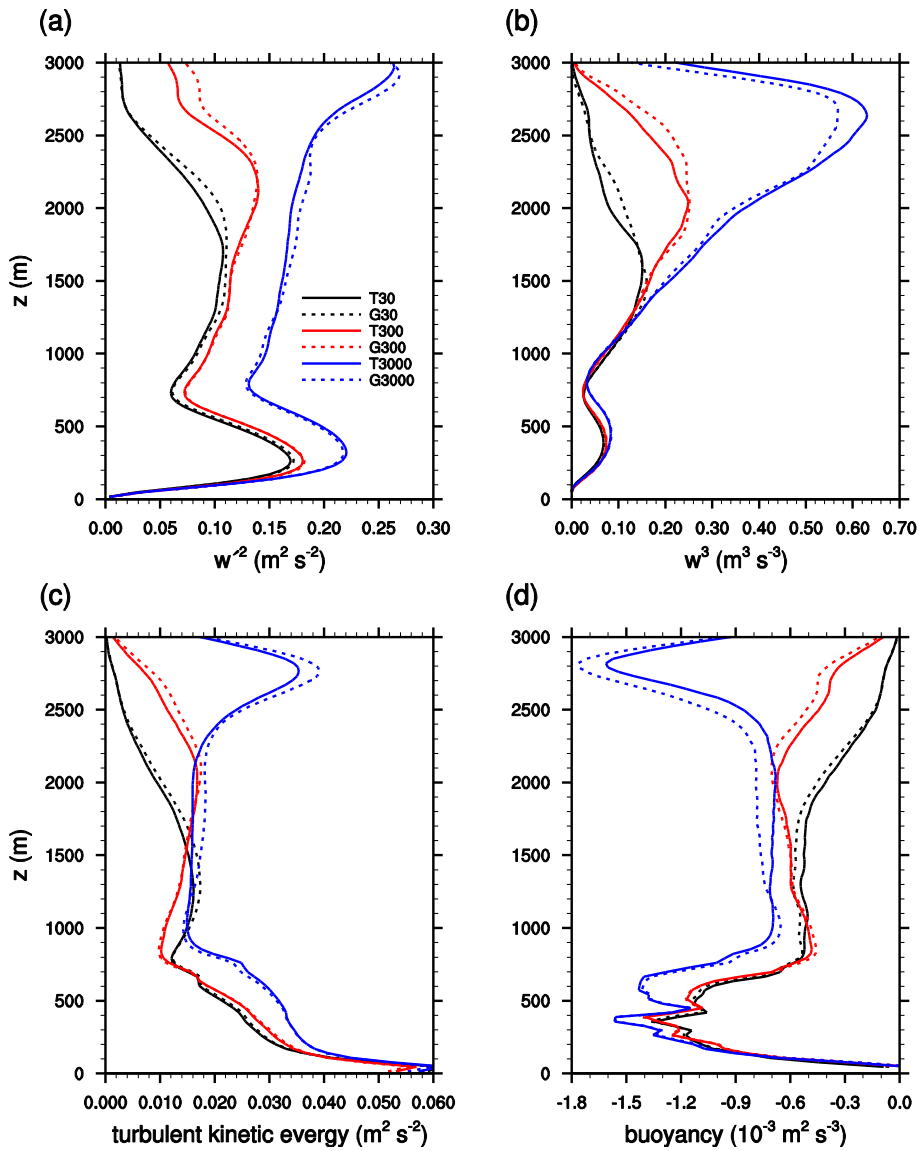

Figure 5.7 Time series of (a) the variance of vertical velocity, (b) the third moment of vertical velocity, (c) turbulent kinetic energy, and (d) buoyancy (the value of buoyancy term in the turbulent kinetic energy equation) averaged over the entire domain and the last 3 h.

decrease in TKE is due to a decrease in the variance of winds, resulting from the more stabilized atmosphere and the resultant decrease in shear production (Fig. 5.7a). The buoyancy increases due to TICE (Fig. 5.7d). Wyszogrodzki et al. (2013) also reported the increase in buoyancy tendency due to the decreased liquid water loading. However, the differences in TKE, the variance of vertical velocity, and the buoyancy are small in this study, which is also true in Franklin (2014). Therefore, careful interpretation and more studies are needed to clarify the effects of TICE on the dynamic properties and feedback direction. It is noted that w^3 has positive values, which reflects small but strong updrafts and large but weak downdrafts. The changes in w^3 vary with aerosol concentration. The changes become less positive when N_0 = 30 and 300 cm^{-3} and become more positive when N_0 = 3000 cm^{-3}. Franklin (2014) reported that w^3 is always positive and always becomes more positive as TICE is considered because of the increased latent heat release. The increase in latent heat release is not distinct in this study, and it might explain the different results.

Figure 5.8 depicts the time series of cloud albedo averaged over the cloudy columns and over the entire domain. The cloud albedo is calculated using the formula suggested by Zhang et al. (2005) with the difference that this study explicitly calculates the cloud optical depth using the predicted number concentration of each drop bin rather than parameterizes it using LWP. The effects of TICE are shown clearly in the cloud-averaged albedo (Fig. 5.8a). TICE decreases the cloud albedo when N_0 = 300 and 3000 cm^{-3}. The cloud albedo decreases because of the increased drop radius but decreased drop number concentration (Fig. 5.3). It reduces the total sum of drop cross section and

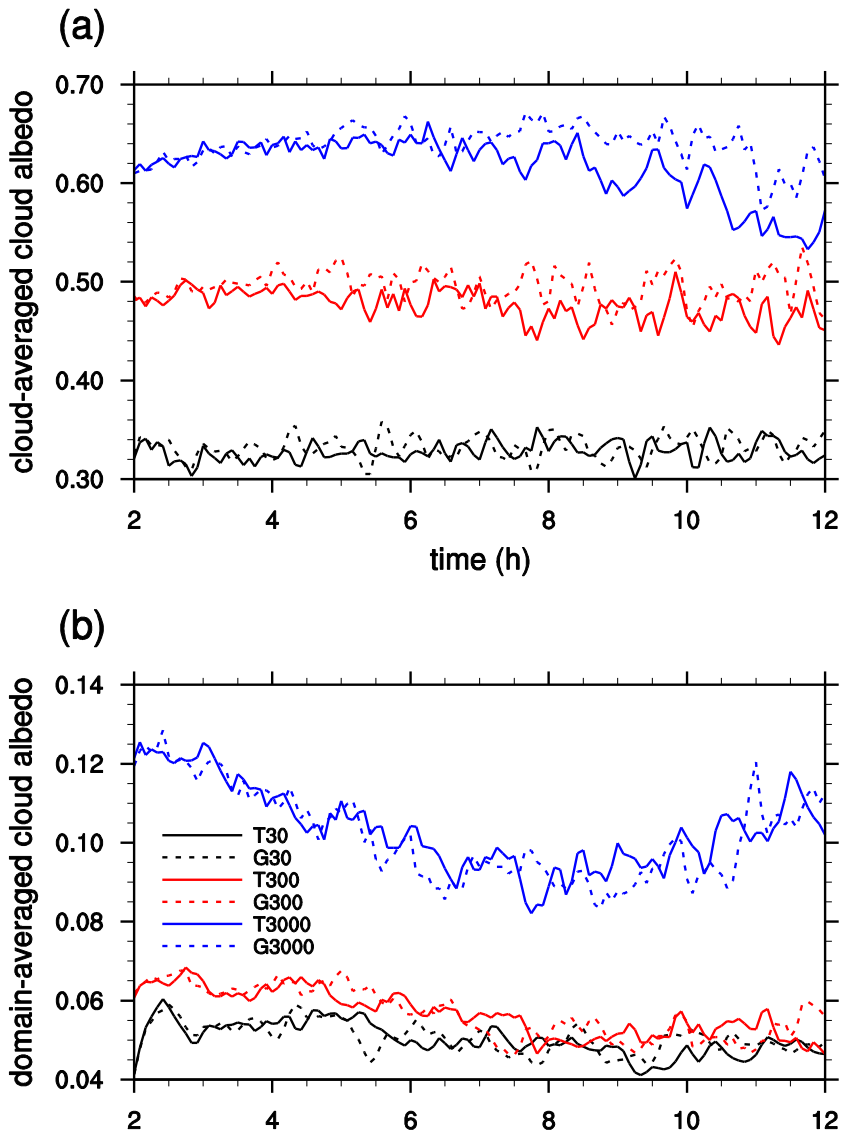

Figure 5.8 Time series of cloud albedo averaged over (a) the cloudy columns and (b) the entire domain.

resultant cloud optical depth. The difference in cloud albedo is not distinct when N_0 = 30 cm^{-3} because the changes in drop radius and drop number concentration are not large. In contrast to the cloud-averaged albedo, the effects of TICE on the domain-averaged cloud albedo are not clear in all simulation cases (Fig. 5.8b). Moreover, a slight increase in the domain-averaged cloud albedo can be seen when N_0 = 3000 cm^{-3}. This is mainly due to the increased cloud fraction (Fig. 5.6a). The increased drop radius due to TICE induces the increased cloud area and the decreased cloud optical depth. The increased cloud area and the decreased cloud optical depth largely cancel each other so that there is little change in the domain-averaged cloud albedo.

5.4. Precipitation effects on cloud morphology

Aerosol-cloud-precipitation interactions comprise important problems in shallow convection (e.g., Xue et al., 2008; Feingold et al., 2010; Koren and Feingold, 2011). Recent modeling studies have shown that precipitation organizes an open cellular structure and induces a new convection around the precipitating area (e.g., Xue et al., 2008). Because TICE increases the surface precipitation (Fig. 5.2c), it is expected that this increased precipitation may affect the cloud development.

Figure 5.9 shows the snapshots of low-level vertical velocity, cloud albedo, and surface precipitation rate at t = 9 h. It is clearly seen that precipitation induces downdrafts and that a wide cloud-free area forms, which is centered at the downdraft and surrounded by the ring-type updrafts, which are similar to the results of previous studies (e.g., Xue et al., 2008; Wang and Feingold, 2009). However, unlike the results of previous studies, the destabilization induced by the

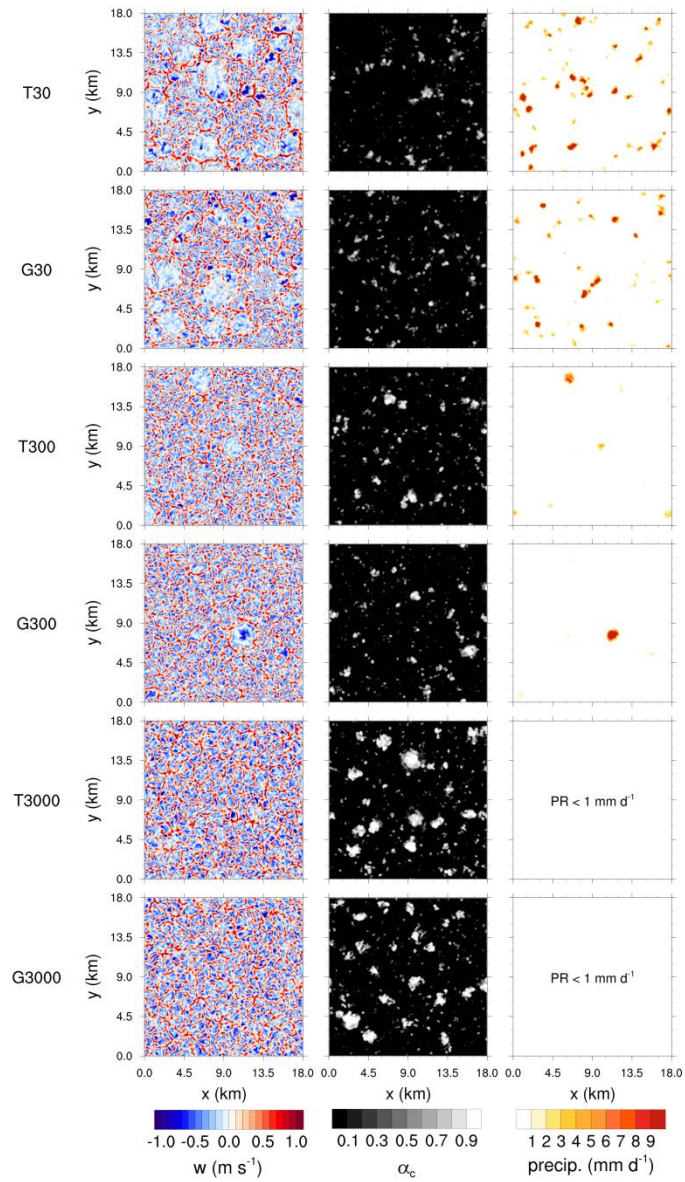

Figure 5.9 Snapshots of (left) the vertical velocity at z = 180 m, (middle) cloud albedo, and (right) surface precipitation rate at t = 9 h for each simulation case. The precipitation rate in T3000 and G3000. at t = 9 h is weaker than 1 mm d^{-1} everywhere.

evaporative cooling and the increase in TKE in the sub-cloud layer (e.g., Xue et al., 2008; Franklin, 2014) do not appear in this study (Fig. 5.7c). In addition, when the time evolution of the low-level vertical velocity and surface precipitation rate fields are analyzed, the TICE-induced increased precipitation hardly affects the cloud structure and morphology (not shown). The ring-type updrafts form around the cold pool induced by precipitation, but those updrafts do not seem to develop enough to produce secondary convection and precipitation when N_0 = 300 or 3000 cm^{-3}.

One possible reason for these small changes is related to the precipitation intensity. The average precipitation rates in the aforementioned studies are of the order of a few millimeters per day, while the rates in this study have orders of 10^{-1} and 10^{-3}–10^{-2} millimeter per day when N_0 = 300 and 3000 cm^{-3}, respectively. Therefore, the precipitation intensity with these aerosol concentrations is weak compared to precipitation intensities of previous studies, and the continuous reactions (secondary convection and precipitation) might be rarely observed. The precipitation intensity when N_0 = 30 cm^{-3} has an order similar to that of previous studies, but the differences in precipitation induced by TICE are so small that the differences can hardly produce the differences in cloud structure and morphology. As a result, TICE-induced increased precipitation affects minimally the development of the clouds in this study.

6. Effects of turbulence on a heavy precipitation case observed in the Korean Peninsula

6.1. Case description and experimental setup

A heavy precipitation event occurred on 21 September 2010 over the middle Korean Peninsula. The maximum 24-h accumulated precipitation amount recorded by the Automatic Weather Station (AWS) operated by the Korea Meteorological Administration is 293 mm, and many AWSs in the middle Korean Peninsula showed accumulated precipitation amounts of more than 200 mm. The surface precipitation was concentrated over a relatively short period (approximately 4–5 h), and the maximum precipitation rate reached as high as 100 mm h^{-1}. Thermodynamic conditions for this case were somewhat different from typical heavy precipitation conditions: convective available potential energy was almost zero around the heavy precipitation area during the precipitation period. Instead, synoptic conditions were the key to the production of this heavy precipitation. A tropical depression transported abundant water vapor from the south, and two different high pressure systems made a convergence zone near the middle Korean Peninsula. The transported water vapor was supplied to the convergence zone, and the heavy precipitation occurred in the convergence zone. A detailed description of the synoptic and mesoscale conditions of this event was provided in Jung and Lee (2013).

To examine this event and investigate the effects of turbulence on this

heavy precipitation case, the WRF model version 3.6.1 coupled with the bin microphysics scheme is adopted. The model domain configuration and selected physics schemes are shown in Fig. 6.1 and Table 6.1, respectively. Three domains are used with one-way nesting, with horizontal grid sizes of 25, 5, and 1.667 km, respectively. TKE that is needed to calculate turbulent parameters is obtained from the Meller-Yamada-Janjic planetary boundary layer (PBL) scheme (Janjic 2002). NCEP (National Centers for Environmental Prediction) final analysis data ($1^o \times 1^o$, 6-h intervals) are used to provide initial and boundary conditions at the outermost domain. The model top is 50 hPa, which is approximately 20 km. The number of vertical layers is 33, and the vertical grid size is ~30 m in the lowest layer and increases up to ~800 m with height. Model integrations are performed for 24 h, from 12 UTC 20 September to 12 UTC 21 September (from 21 LST 20 September to 21 LST 21 September).

The initial aerosol size distribution is set to follow the Twomey equation (Twomey 1959), which is the same as that of Khain et al. (2000) and Section 3. The initial aerosol number concentration is set for the cloud condensation nuclei (CCN) number concentration at 1% supersaturation to be 100 cm^{-3} below z = 2 km and decreases exponentially above z = 2 km with an e-folding depth of 2 km. The aerosol replenishment scheme provided in Jiang and Wang (2014) is employed to restore the aerosol concentration to the value at the initial state.

6.2. Validation

First of all, to validate the model, the observed and simulated synoptic-scale weather patterns are compared. Figure 6.2 shows the observed weather chart at

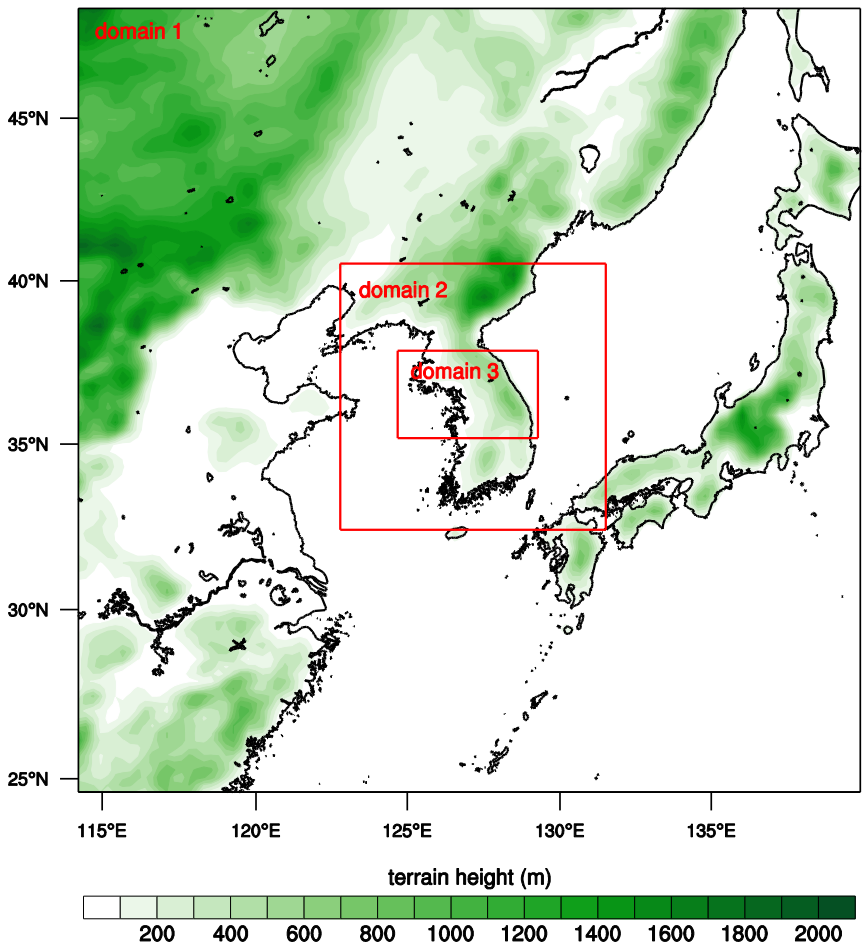

Figure 6.1 Illustration of three nested model domains with terrain height.

Table 6.1 Model domain configuration and list of physics schemes in the WRF model used in this study.

	domain 1	domain 2	domain 3
horizontal grid size	25 km	5 km	1.667 km
horizontal grid numbers	108 × 108	181 × 181	286 × 178
PBL scheme	Mellor-Yamada-Janjic (Janjic 2002)		
cumulus scheme	Kain-Fritsch (Kain 2004)	none	
radiation scheme	longwave: RRTM (Mlawer et al. 1997) shortwave: MM5 (Dudhia 1989)		
land surface scheme	Noah (Chen and Dudhia 2001)		
surface-layer scheme	Eta similarity (Janjic 2002)		

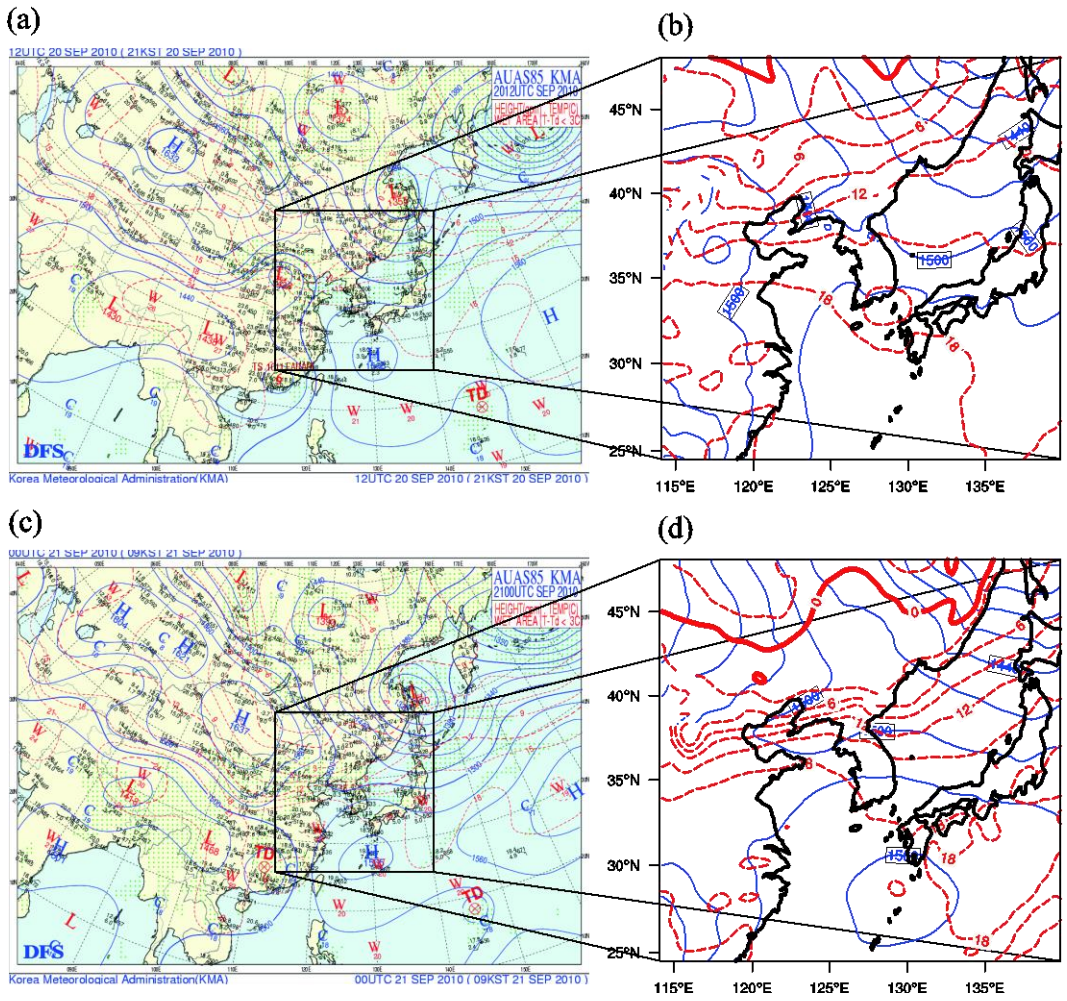

Figure 6.2 Synoptic weather charts at 850 hPa level (a) provided by the Korea Meteorological Administration and (b) depicted using NCEP final analysis data at 21 LST 20 September 2010. Intervals for geopotential height (blue solid line) and isotherm (red dashed line) are 30 m and 3^{o}C, respectively. In (b), the 0^{o}C isotherm line is represented by the red solid line. (c) is the same as (a) but at 09 LST 21 September 2010, and (d) is the same as (b) but simulated at 09 LST 21 September 2010.

850 hPa level and the corresponding model initial data at 21 LST 20 September, and the observed weather chart at 850 hPa level and the corresponding model simulation result at 09 LST 21 September. The synoptic-scale weather conditions were in favor of the heavy precipitation event. At 09 LST 21 September, a tropical depression had moved to the northwest in the northern Pacific, and the northern Pacific high had moved toward the Korean Peninsula. At this time, a continental high had also expanded with cold air from the northwest of the Korean Peninsula. Therefore, a narrow convergence zone with a high temperature gradient formed and mesoscale convective systems developed in the convergence zone. Moreover, another tropical depression had landed on southern China, which provided a plenty of water vapor in the convergence zone through southwesterly winds.

The features mentioned above are well simulated in the WRF model (Fig. 6.2d). It is shown in Fig. 6.2d that the 0℃ isotherm line moves toward south considerably as the continental high expands. At the same time, as the northern Pacific high expands toward the Korean Peninsula, a frontal zone (the convergence zone with large temperature gradient) forms between ~38°N and ~40°N before a few hours of heavy precipitation. Moreover, a tropical depression landing on southern China is seen in the simulation. Overall, the important features of the weather system that caused the heavy precipitation event are reproduced well in the simulation.

The fields of surface precipitation amount accumulated over 00–21 LST 21 September simulated in this study and observed by the Tropical Rainfall Measuring Mission (TRMM, Huffman et al. 2007) are plotted in Fig. 6.3. Compared to the TRMM observation, the simulation tends to underestimate the

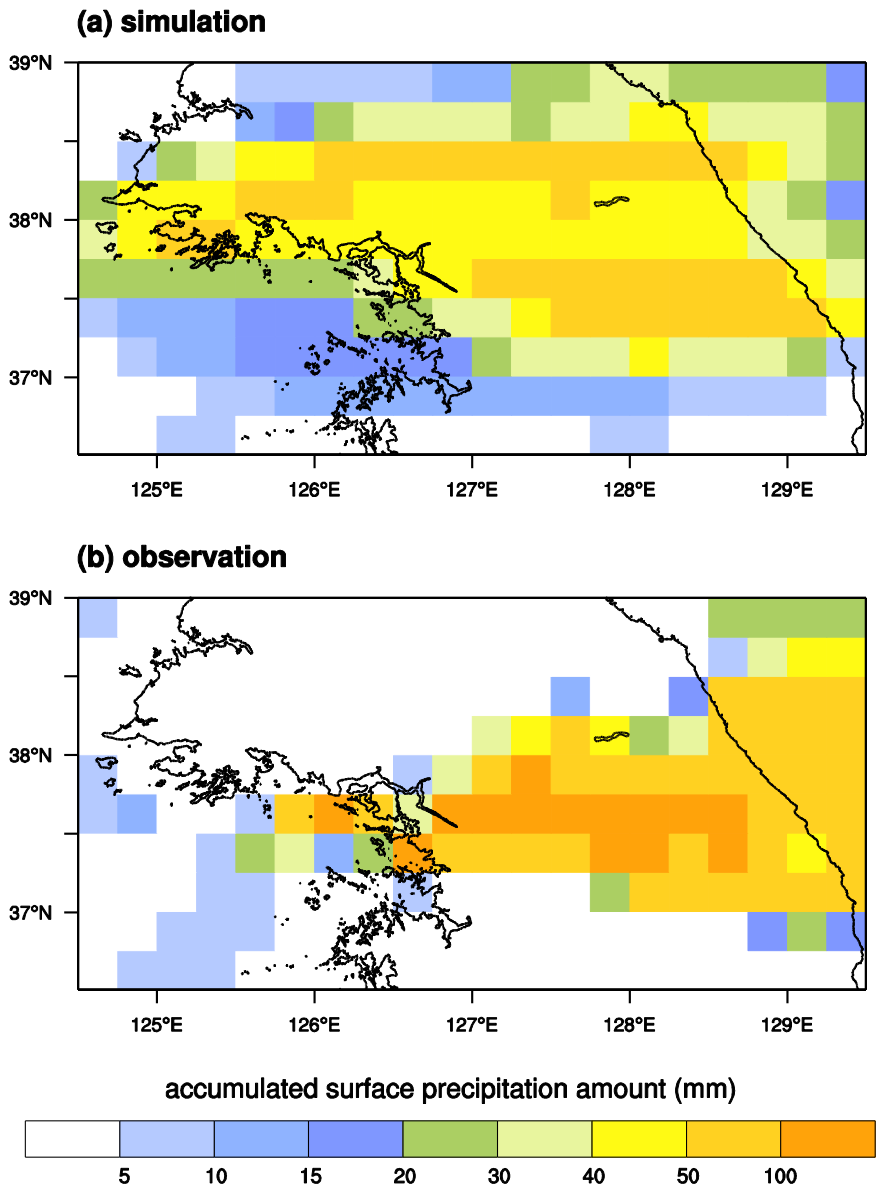

Figure 6.3 Surface precipitation amount accumulated over 00–21 LST 21 September (a) in the simulation case with TICE and (b) in the observation by TRMM.

surface precipitation amount and the simulated surface precipitation is spread over a larger area. However, the simulation is generally similar to the TRMM observation in that the strong band-type precipitation is concentrated in the middle Korean Peninsula and the spatial deviation of surface precipitation amount is large. It is noted that the simulated surface precipitation amount is partially concentrated southwest of the precipitation area, whereas the observed surface precipitation amount is relatively small there.

The time evolution of radar reflectivity fields for 10–17 LST 21 September from the simulation and observation is shown in Fig. 6.4. Strong precipitation echoes are seen northwest of Seoul at 10 LST in both the simulation and observation. Seoul is depicted by a closed curve near the center of each figure in Fig. 6.4b. While a part of the strong precipitation echoes move from northwest of Seoul to northeast of Seoul, another narrow and strong (> 40 dBZ) band-type precipitation echoes affect Seoul and its nearby area for approximately 4–5 h, from 13 LST to 17–18 LST. These features are also found well in the simulated radar reflectivity fields. Although the radar reflectivity in Seoul and its nearby area is somewhat underestimated in the simulation compared to the observed radar reflectivity, general features are well reproduced in the simulation.

6.3. Turbulent structures and precipitation

By including and excluding TICE, the effects of turbulence on cloud development are investigated focusing on the surface precipitation. Firstly, whether the turbulent structure is well simulated is examined because it directly affects the effects of turbulence on cloud development. Figure 6.5 shows the time series and

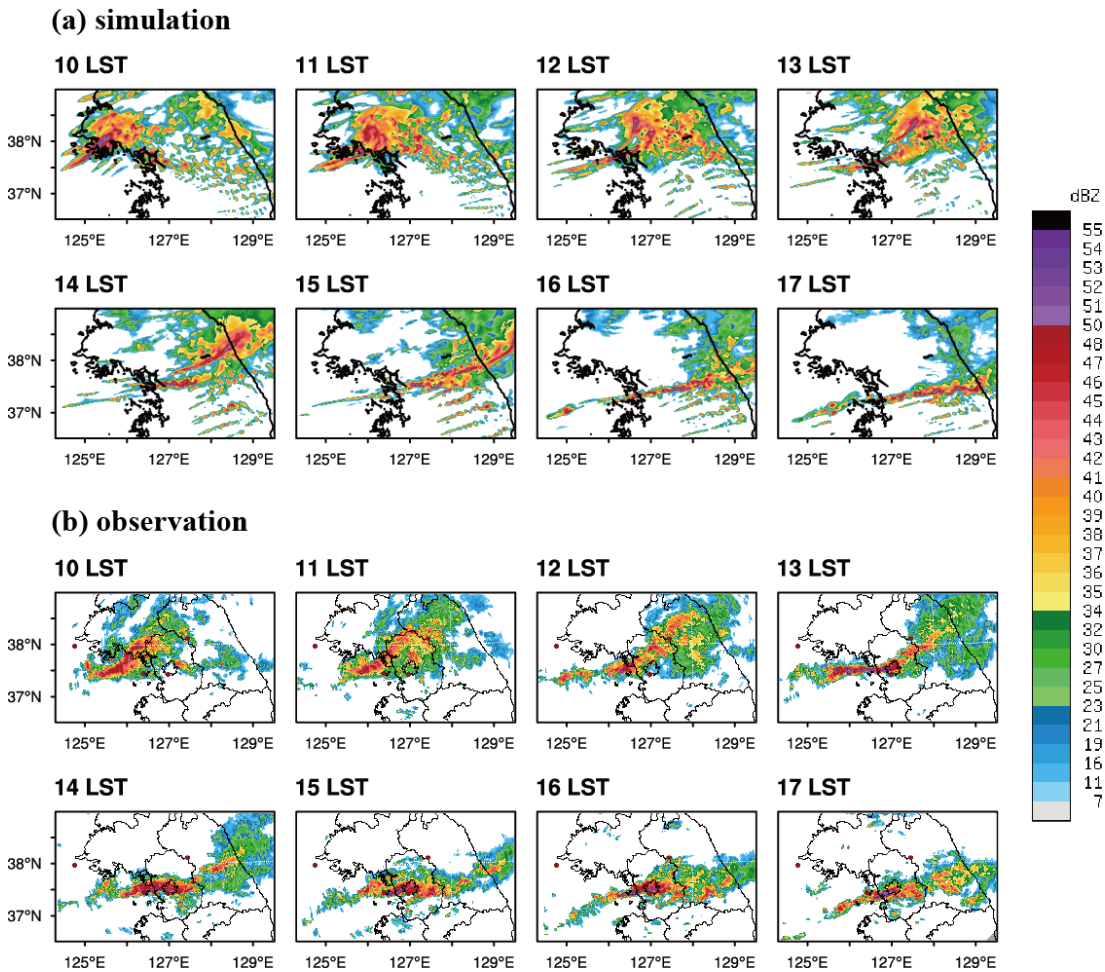

Figure 6.4 Fields of radar reflectivity (CAPPI at z = 1.5 km) for 10–17 LST 21 September (a) in the simulation case with TICE and (b) in the observation by radars operated by the Korea Meteorological Administration. Seoul is depicted in (b) with a small closed curve near the center of each figure (~37.5°N, ~127°E). Red dots in (b) correspond to the radar observation sites.

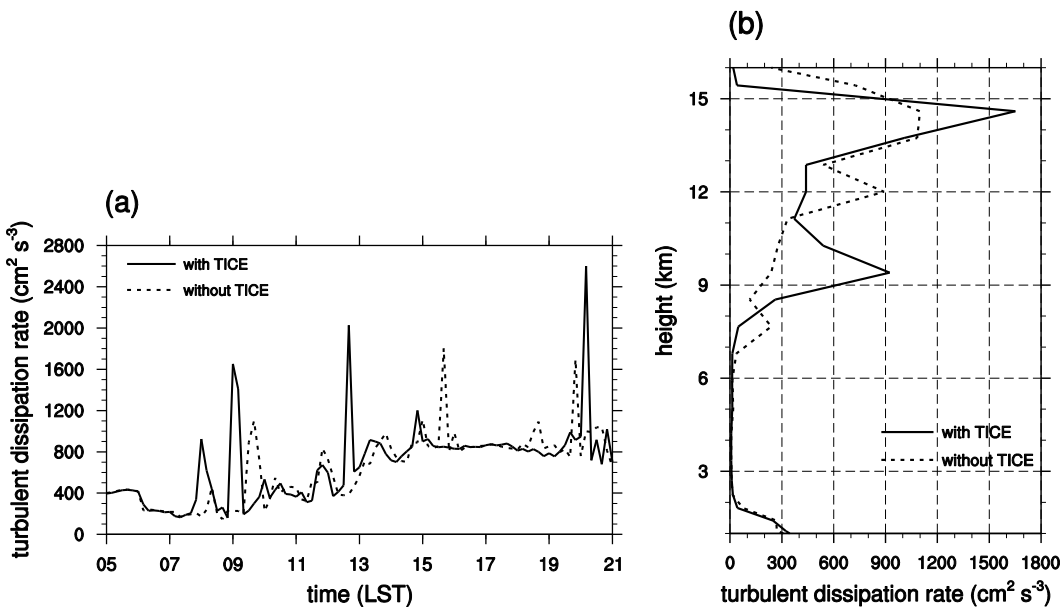

Figure 6.5 (a) Time series of the maximum turbulent dissipation rate in the clouds and (b) vertical profiles of the maximum turbulent dissipation rate in the clouds averaged over 07–13 LST in the cases with and without TICE. Cloudy point is defined using a total hydrometeor content threshold of 0.01 g kg^{-1}.

vertical profiles of the maximum turbulent dissipation rate in the cases with and without TICE. The time series of the maximum turbulent dissipation rate show that strong turbulence appears intermittently, particularly in the cloud developing stage (07–13 LST 21 September). The maximum turbulent dissipation rate during this period reaches approximately 2000 cm^2 s^{-3} in the case with TICE, which is in the simulated ranges in Benmoshe and Khain (2014) and Lee et al. (2014) that numerically investigated an isolated deep convective cloud using a two-dimensional model with finer grid resolutions. The vertical distributions of the maximum turbulent dissipation rates show that strong turbulent motion mainly appears at high altitudes ($z > 7$ km), which is also in good agreement with the result of Benmoshe and Khain (2014). Therefore, it is concluded that although the grid size is somewhat large (1.667 km in the horizontal, ~0.8 km in the vertical), the simulated turbulent intensity is similar to that of the studies using higher spatial resolutions. Hence, the effects of turbulence can be examined in the present experimental settings. It is noted that the turbulent intensity is generally stronger in the case with TICE than in the case without TICE, which is possibly due to increased latent heating in the case with TICE (Benmoshe and Khain 2014).

Figure 6.6 shows the fields of surface precipitation amount accumulated over 00–21 LST 21 September. In Seoul and its nearby area (indicated as area A), in which the observed surface precipitation amount is largest, the surface precipitation amount is larger in the case with TICE than in the case without TICE. In addition to area A, although there are spatial shifts in the surface precipitation amount, the precipitation averaged over the entire innermost model domain also increases by ~5.7% due to TICE. Overall, the surface precipitation amount in the

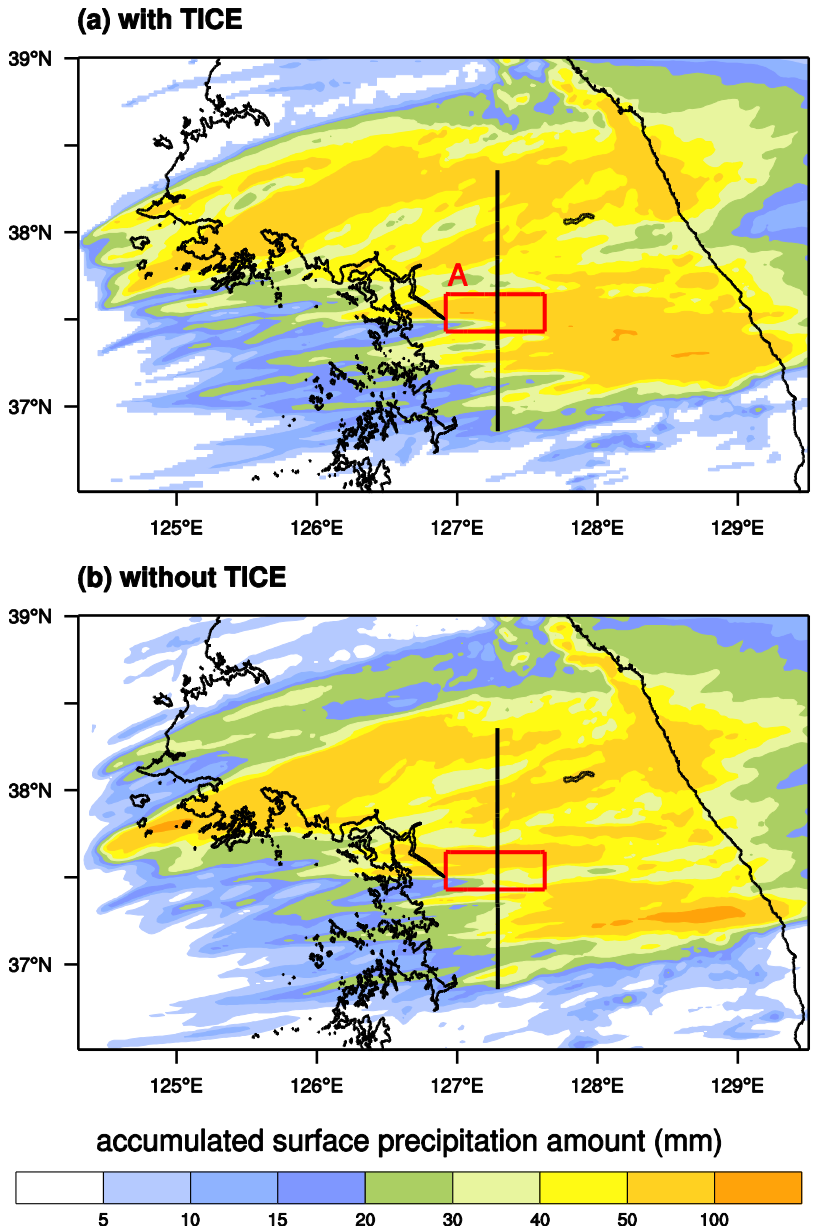

Figure 6.6 Surface precipitation amount accumulated over 00–21 LST in the cases (a) with TICE and (b) without TICE. The red rectangle indicates the area of interest.

case with TICE is larger and is closer to the observation than that in the case without TICE.

Figure 6.7 shows the time series of surface precipitation rate averaged over the entire innermost domain and area A indicated in Fig. 6.6. The time series support the above analysis. The increase in surface precipitation rate due to TICE is distinct in area A: the maximum surface precipitation rate averaged over area A is approximately 35% larger in the case with TICE than in the case without TICE. The increase in the maximum surface precipitation rate is mainly due to the increase in precipitation itself, and the contribution of shift in precipitation is small. The increase in the maximum surface precipitation rate is still ~30% even in the extended area enlarged by ~80% (not shown).

Figure 6.8 shows the contoured frequency-altitude diagram (CFAD) for radar reflectivity averaged over the entire innermost domain for 14–15 LST. A relatively simple bulk approach proposed by Stoelinga (2005) is used to calculate the radar reflectivity. There is little change in frequency at high altitudes in the case with TICE compared to the case without TICE. An extended tail near the surface caused by TICE is observed: the probability of ~50 dBZ is 0.2–0.5% in the case with TICE but 0.1–0.2% in the case without TICE. This reveals that the relative frequency of strong radar reflectivity increases in the case with TICE, which is related to the increased surface precipitation amount. Moreover, CFAD in the case with TICE shows that the high frequency zone (approximately between 20–40 dBZ) has an upright structure, whereas the high frequency zone in the case without TICE has a tilted structure.

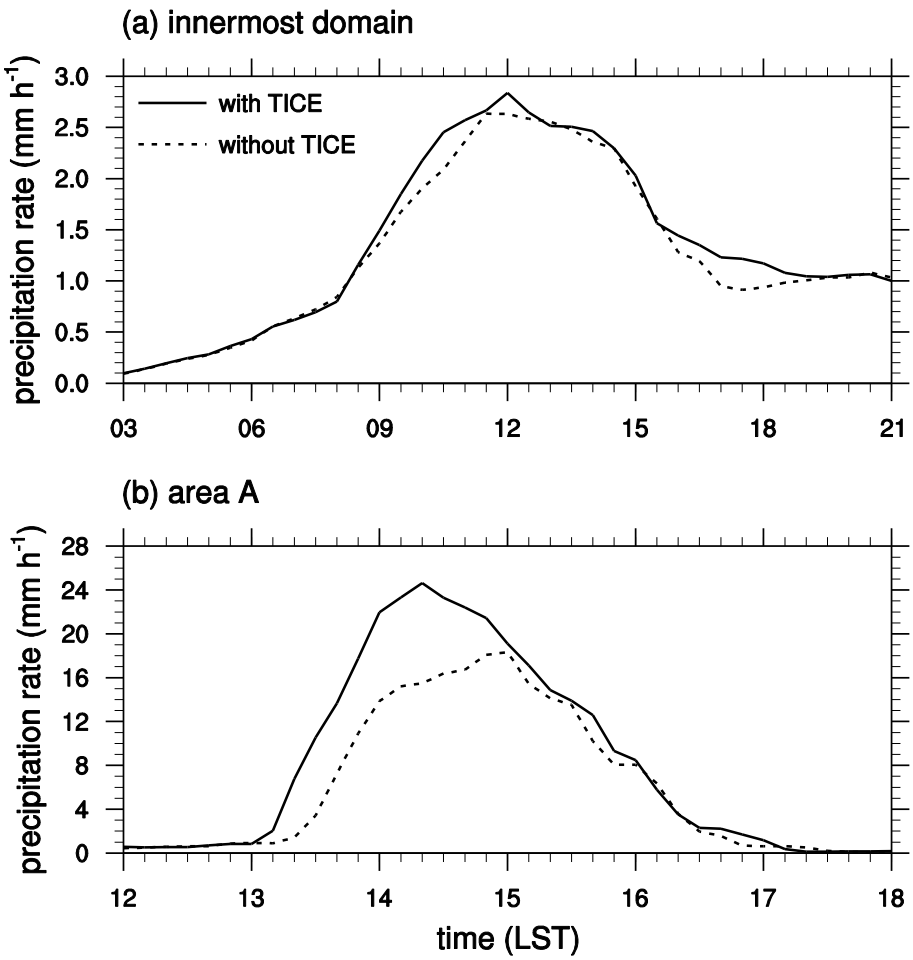

Figure 6.7 Time series of area-averaged surface precipitation rate over (a) the entire innermost domain and (b) area A in the cases with and without TICE.

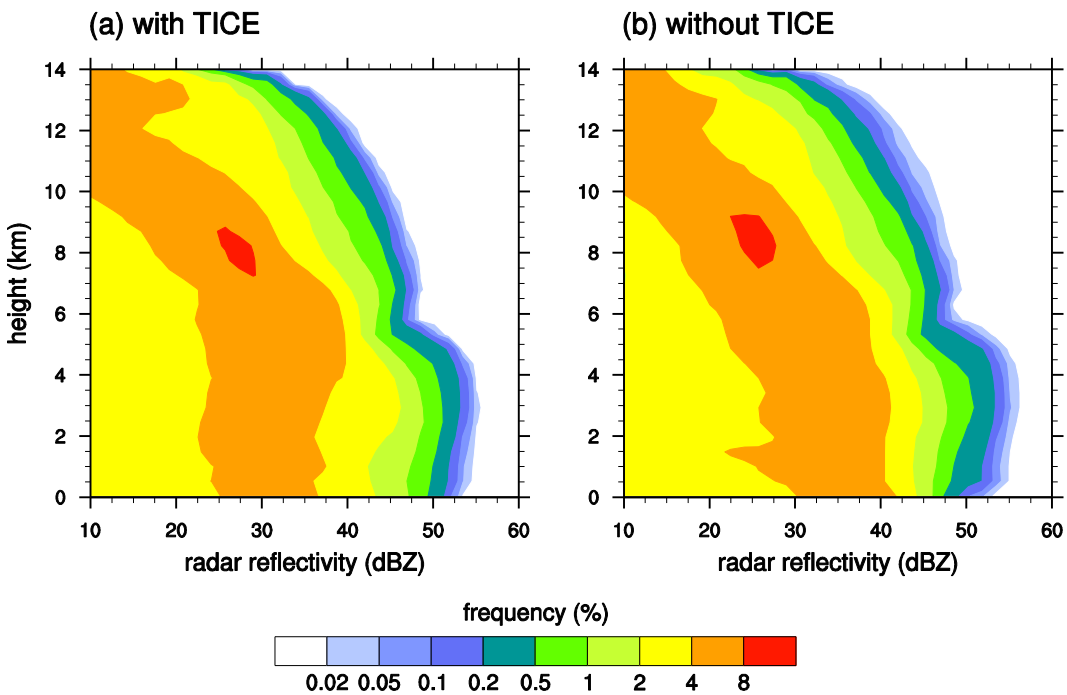

Figure 6.8 Contoured frequency-altitude diagram (CFAD) for radar reflectivity averaged over the innermost domain for 14–15 LST in the cases (a) with TICE and (b) without TICE.

6.4. Microphysical structures

To investigate mechanisms for the increase in surface precipitation amount due to TICE, cloud microphysical structures are analyzed focusing on area A. Figure 6.9 shows the vertical profiles of each hydrometeor content averaged over area A at t = 13, 14, 15, and 16 LST in the cases with and without TICE. It is clear that snow particles comprise the most of cloud mass, followed by graupel particles. In Section 4, graupel particles comprise the most of cloud mass in the uniform basic-state wind case and the portion of snow particles in cloud mass increases in the sheared basic-state wind case because the strong wind shear transports cloud droplets in the cloud-free area, hence increasing the evaporation of cloud droplets and decreasing riming. In this study, vertical wind shear is very strong (horizontal wind speed of ~30 m s^{-1} at z = 6 km), so this strong vertical wind shear might be a reason for the high snow content. In Fig. 6.9, the maximum snow content at t = 13 LST is seen at z ~ 10 km. This implies that a main mechanism for the production of snow and the increase in snow mass in this case is the depositional growth of ice crystal and snow particles because the supercooled drop mass is rarely seen at the altitude at this time. At t = 13–14 LST, the snow mass increases due to TICE and this increase in snow mass induces the increase in rainwater amount. At t = 15 LST, the snow mass in the case without TICE becomes larger than that in the case with TICE, but it affects little the surface precipitation amount because the clouds have been weakened after that time.

To examine the reasons for the changes in snow mass due to TICE, the vertical cross sections (following the black line that passes area A in Fig. 6.6) of

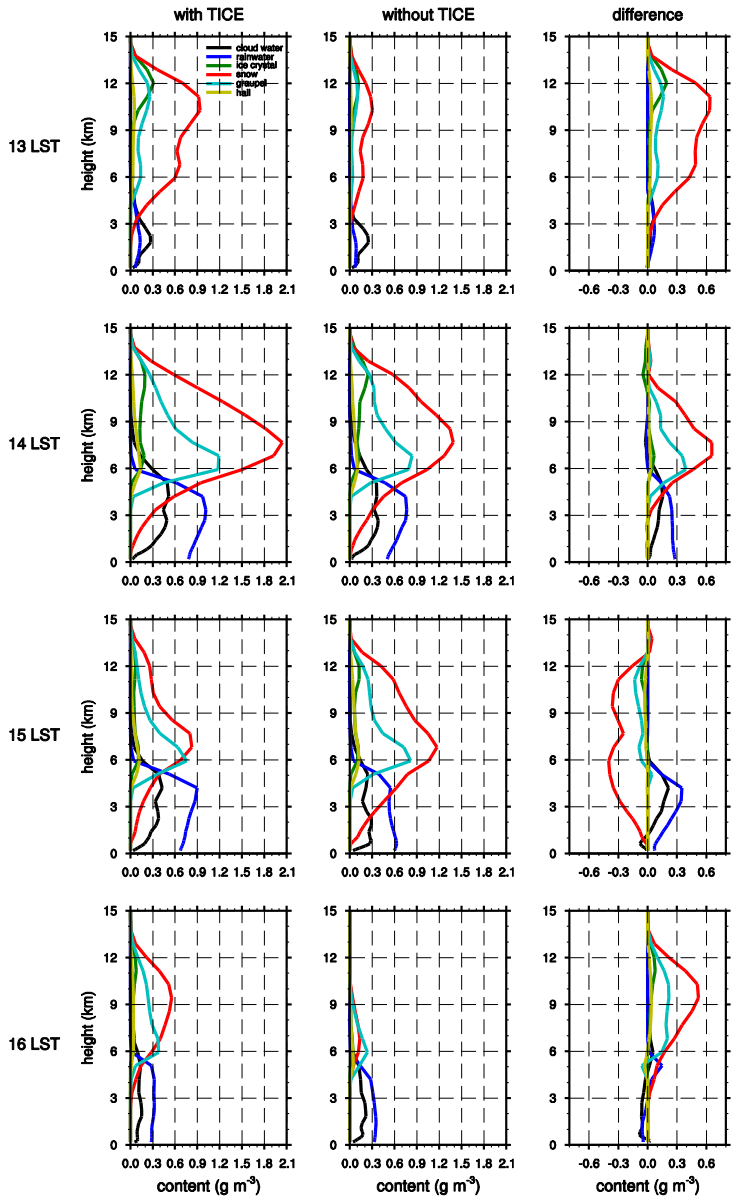

Figure 6.9 Vertical profiles of each hydrometeor content averaged over area A at *t* = (from top to bottom) 13, 14, 15, and 16 LST in the case (left) with TICE and (middle) without TICE. The rightmost column shows the difference between the cases with and without TICE.

relative humidity with respect to ice and wind at t = 12, 13, and 14 LST are shown in Fig. 6.10. The development process of clouds is reflected in these cross sections. At t = 12 LST, there is a front roughly near the boundary between the moist air and the dry air (Fig. 6.10a). Relative humidity in the air parcel that is about to move up following the front is higher in the case with TICE than in the case without TICE. The early coalescence between small cloud droplets induces a decrease in the sum of drop surface areas. Because the condensation rate is expressed by the product of drop surface area (proportional to the square of drop radius) and water vapor density near the drop surface (inversely proportional to drop radius), the decrease in the sum of drop surface areas causes a decrease in condensation (Section 3). Therefore, more water vapor can be transported upward in the case with TICE. At t = 13 LST, dry air comes from the northwest and the clouds show an upright structure. Relative humidity with respect to ice in the clouds is higher in the case with TICE than in the case without TICE because of the increase in water vapor transport. This humid environment favors the growth of ice crystal and snow particles. Although relative humidity in the case without TICE becomes higher at t = 14 LST, as the dry air comes more from the northwest, the frontal zone becomes narrower and the clouds weaken. Hence, the effects of these clouds on the total surface precipitation amount are small.

Figure 6.11 shows the vertical cross sections of snow mass distribution. At t = 12 LST, snow starts to be produced in the frontal zone. The snow mass in the air parcel transported upward following the front is larger in the case with TICE than in the case without TICE. At t = 13 and 14 LST, while the snow mass north of area A little affects the cloud development in area A (see the eastward-moving

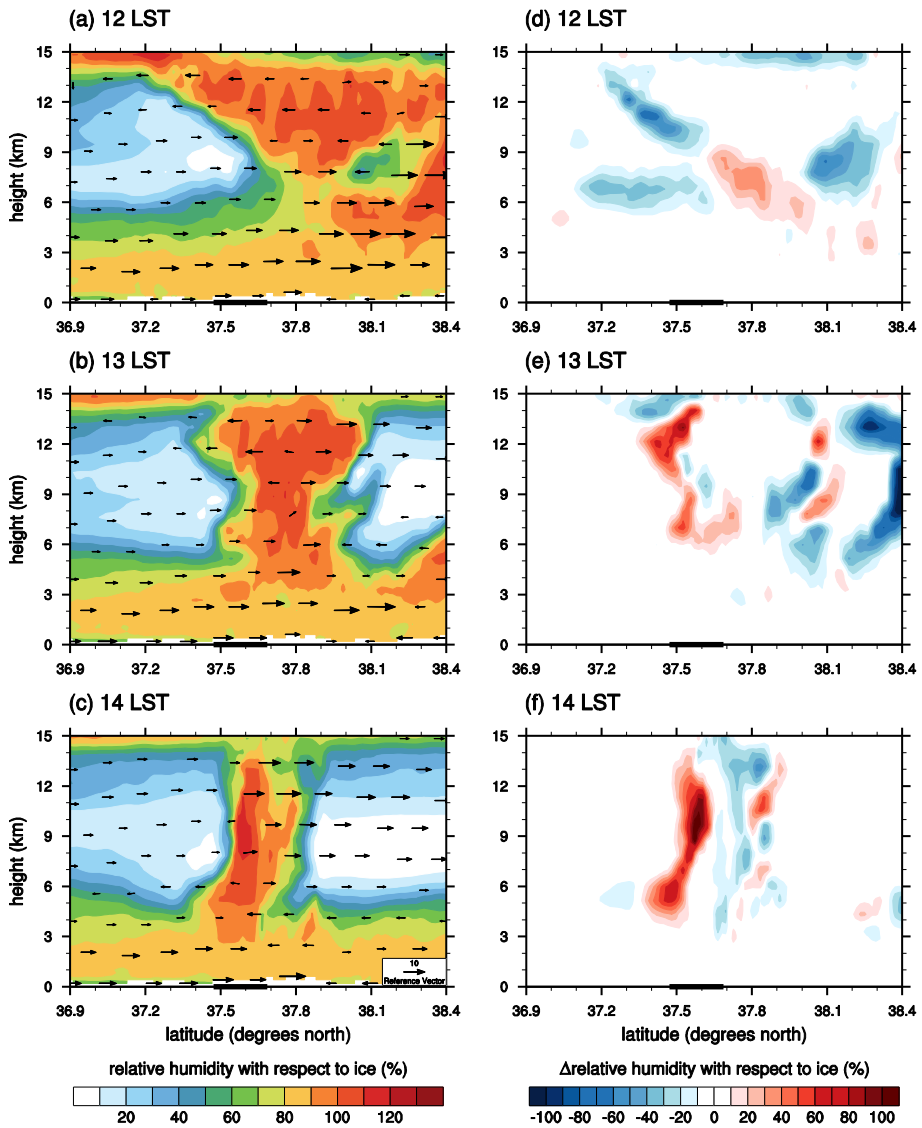

Figure 6.10 Vertical cross sections of relative humidity with respect to ice and wind along the black line in Fig. 6 at *t* = (a) 12 LST, (b) 13 LST, and (c) 14 LST in the case with TICE. Thick black lines correspond to area A. (d)–(f) are the same as (a)–(c) but for the difference in relative humidity with respect to ice caused by TICE.

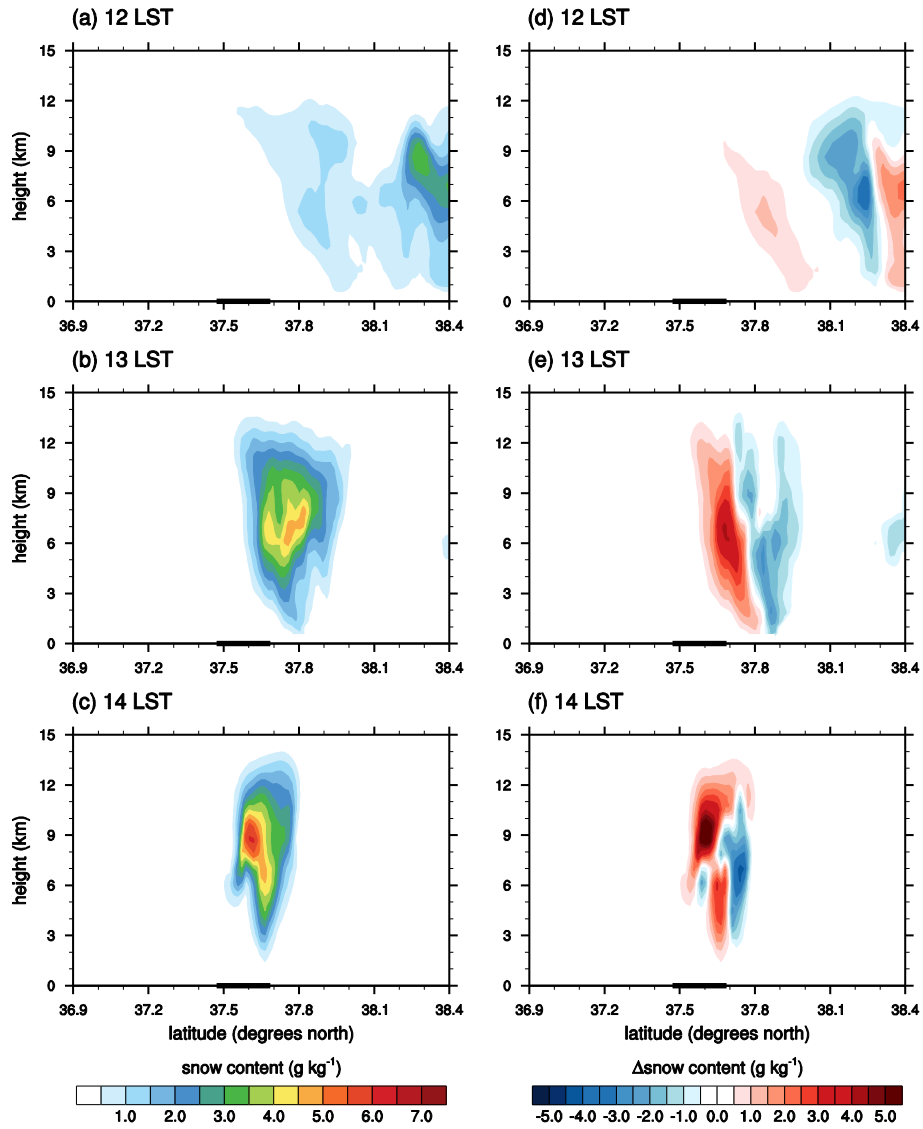

Figure 6.11 As in Fig. 6.10 but for snow mass.

precipitation echoes along the north of Seoul in Fig. 6.4), the snow mass in the clouds in the frontal zone is larger in the case with TICE than in the case without TICE due to the increased relative humidity with respect to ice. The increase in snow mass due to the increased excess water vapor at high altitudes induces the increase in surface precipitation amount. It is noted that the increase in snow mass in the frontal zone is seen to be delayed in the case without TICE but the effects of these clouds on the total surface precipitation amount are small (Figs. 6.9 and 6.10).

It is possible that the growth of snow particles by riming is reduced due to TICE because coalescence between small droplets is accelerated and resultant large drops fall out to the ground at earlier times. In addition, the rimed snow particle has a larger terminal velocity than the pristine snow particle of the same mass. Therefore, the decreased riming can induce a decrease in snow mass in the lower layer of the clouds by decreasing both snow mass and terminal velocity. However, it is also possible that TICE can increase riming because of the increased snow mass due to depositional growth.

Figure 6.12 shows the field of the rimed fraction of snow in both cases. At first, the rimed fraction of snow does not generally exceed 10% because if the density of snow exceeds 200 kg m^{-3} the particle is regarded as graupel. In addition, the rimed fraction of snow exhibits a maximum near $z \sim 6$ km. This is because the number of supercooled drops decreases significantly with increasing altitude over the freezing level ($z \sim 5$ km). At t = 12 LST, the rimed fraction of snow in the clouds that are in the north of area A is larger in the case with TICE than in the case without TICE. However, the larger rimed fraction of snow little affects the

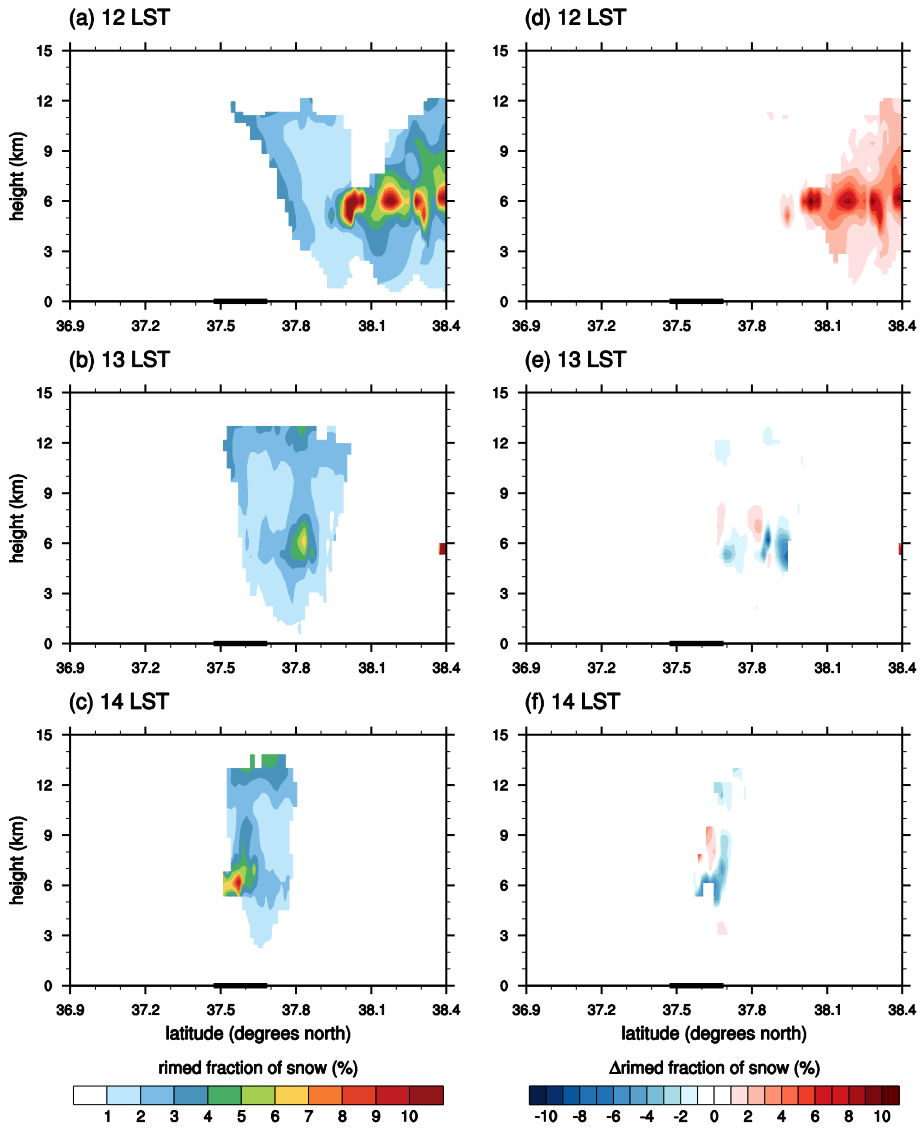

Figure 6.12 As in Fig. 6.10 but for the rimed fraction of snow.

rimed fraction of snow in the clouds that form in the frontal zone, which is the same as in Fig. 6.11. It is shown that TICE reduces the rimed fraction of snow in the clouds in the frontal zone due to the reduced droplets aloft at t = 13 and 14 LST, as expected above. However, the large rimed fraction in this cloud is concentrated only at small part and the value of rimed fraction and the difference in rimed fraction are generally small.

Figure 6.13 shows the vertical profiles of temperature change rate (i.e., latent heat release or absorption rate) due to some ice microphysical processes. It is seen that the growth of ice particles due to riming is also larger in the case with TICE than in the case without TICE although the rimed fraction of snow decreases due to TICE (Fig. 6.12). This is because TICE increases ice mass by increasing depositional growth so the increase in ice mass due to riming is also larger in the case with TICE than that in the case without TICE although TICE decreases the rimed fraction of snow by decreasing supercooled drops. This increase in ice mass induced by TICE causes an increase in rainwater and precipitation by increasing melting of ice particles. It is noted that riming is the most dominant process in increasing the ice mass, although the temperature change rate due to deposition is highest. This is because the latent heat rate from vapor to ice per unit mass is approximately eight times the latent heat rate from water to ice per unit mass, but the temperature change rate due to deposition is only approximately three times that due to riming.

Figure 6.14 shows the size distributions of snow at z = 4, 7, and 10 km at t = 13 LST and 14 LST in the cases with and without TICE. From 13 to 14 LST, the snow mass at z = 4 and 7 km increases, which reflects the sedimentation of snow

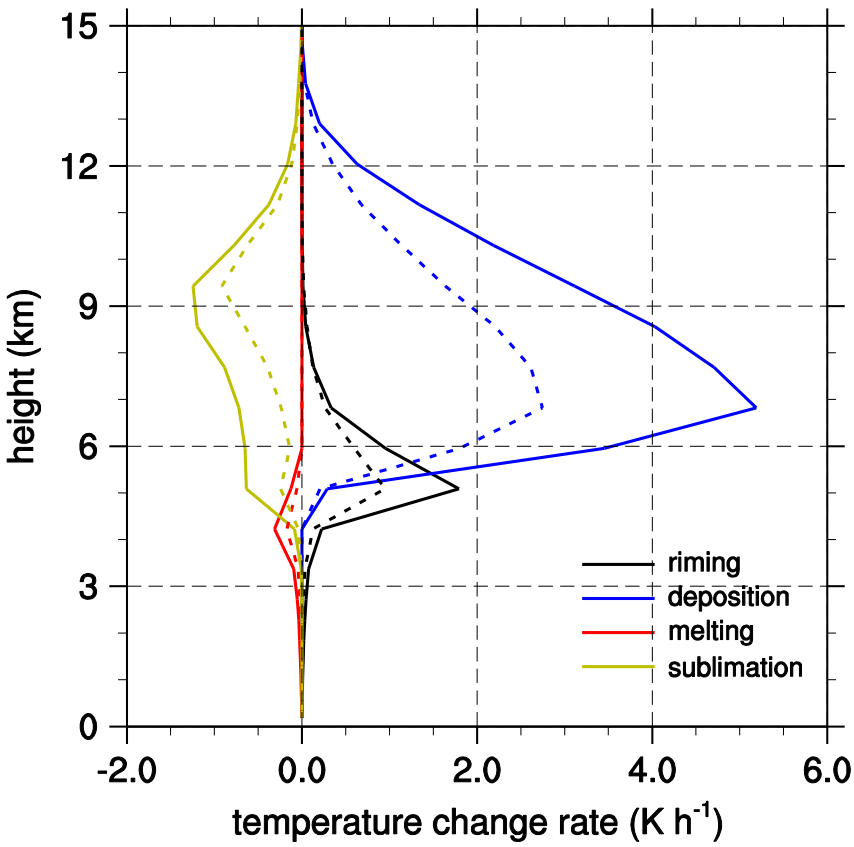

Figure 6.13 Vertical profiles of temperature change rate due to riming, deposition, melting, and sublimation averaged over area A for 12–14 LST in the case with TICE (solid lines) and without TICE (dashed lines).

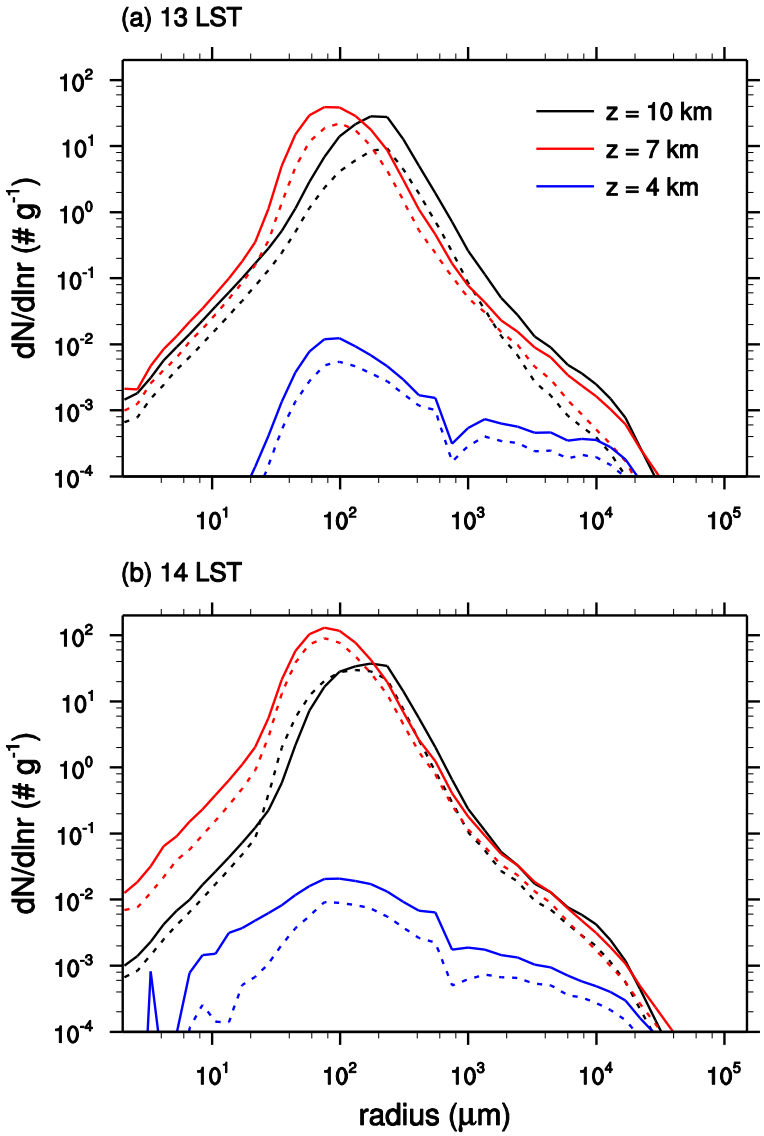

Figure 6.14 Size distributions of snow at z = 4, 7, and 10 km averaged over area A at t = (a) 13 LST and (b) 14 LST in the case with TICE (solid lines) and without TICE (dashed lines).

and the increase in snow mass by riming (Figs. 6.9 and 6.12). At all altitudes, the maximum number concentration of snow appears near the radius of ~100 μm regardless of TICE, so TICE little changes peak snow radius. Instead, TICE increases the snow number concentration in almost the entire range of snow radius, which is similar to the graupel size distribution in the sheared basic-state wind case of Section 4. It is seen in Fig. 6.14 that the intercept parameter of snow size distribution function varies significantly. This suggests that bulk microphysics schemes that represent a snow size distribution using a simple function need to employ at least two moments to represent the snow size distribution more appropriately. It is expected that the results of the bin microphysics scheme with TICE are utilized to improve bulk microphysics schemes.

7. Development of a new autoconversion parameterization with inclusion of the turbulence effects

7.1. Parameterization of the autoconversion process

The well-known stochastic collection equation that deals with the change in the cloud particle number concentration due to the collision and collection process is given as follows:

$$\frac{\partial g(m)}{\partial t} = \int_0^{m/2} g(m-m')K(m-m',m')g(m')dm' - \int_0^{\infty} g(m)K(m,m')g(m')dm', \tag{7.1}$$

where $g(m)dm$ is the number concentration of cloud particles within the mass interval of (m, $m+dm$) and K is the collection kernel. The first term of R.H.S. of Eq. (7.1) represents the formation of the cloud particle with the mass of m due to the collision of the cloud particles whose masses are $m–m'$ and m', while the second term represents the elimination of the cloud particle whose mass is m due to the collision with other cloud particle. The upper limit of the first term of R.H.S. of Eq. (7.1) is set to $m/2$ to avoid the duplication. The collection kernel K is expressed by the product of swept volume of the two cloud particles and the collection efficiency, as follows:

$$K(r,r') = \pi\left(r + r'\right)\left|v_t(r) - v_t(r')\right|\eta, \tag{7.2}$$

where r and r' are the radii of the two particles, v_t is the terminal velocity of the cloud particle, and η is the collection efficiency that is the product of the collision efficiency and coalescence efficiency.

Because the autoconversion process considers the production of raindrop via the collision between cloud droplets, the second term of R.H.S. of Eq. (7.1) does not needed to evaluate to consider the autoconversion process. Therefore, if $g(m)$ is the size distribution function of cloud droplet, the autoconversion rate can be expressed using the stochastic collection equation as:

$$\begin{aligned}\left.\frac{\partial q_r}{\partial t}\right|_{\text{au}} &= \int_{m^*}^{\infty} mg(m)dm \\ &= \int_{m^*}^{\infty}\int_{0}^{m/2} mg(m')K(m', m-m')g(m-m')dm'dm.\end{aligned} \tag{7.3}$$

Here, q_r is the mass concentration of raindrop, m^* is the threshold mass between cloud droplet and raindrop, 2.68×10^{-10} kg (corresponding drop radius of 40 μm). By changing the integration order, Eq. (7.3) can be expressed as:

$$\begin{aligned}\left.\frac{\partial q_r}{\partial t}\right|_{\text{au}} &= \int_{0}^{\infty}\int_{2m'}^{\infty} mg(m')K(m', m-m')g(m-m')dmdm' \\ &\quad - \int_{0}^{m^*/2}\int_{2m'}^{m^*} mg(m')K(m', m-m')g(m-m')dmdm'.\end{aligned} \tag{7.4}$$

The second term of the R.H.S. of Eq. (7.4) represents the self-collection of cloud droplets. By introducing change of variables, Eq. (7.4) is approximated and rearranged after some manipulation as:

$$\left.\frac{\partial q_r}{\partial t}\right|_{au} \approx \int_0^{\infty}\int_o^{M}(M+m)g(m)K(m,M)g(M)dmdM - \alpha\int_0^{m^*}\int_0^{M}(M+m)g(m)K(m,M)g(M)dmdM. \tag{7.5}$$

A new constant α is introduced because the approximation applied above results in an overestimated self-collection of cloud droplets. α, which is less than but should be close to 1, would be determined using the detailed bin model results. In this study, α = 0.88.

By changing the variables from the mass quantities to radius quantities, Eq. (7.5) is rewritten as:

$$\left.\frac{\partial q_r}{\partial t}\right|_{au} = \rho_w\frac{4}{3}\pi\int_0^{\infty}\int_0^{R}(R^3+r^3)f(r)K(r,R)f(R)drdR - \alpha\rho_w\frac{4}{3}\pi\int_0^{r^*}\int_0^{R}(R^3+r^3)f(r)K(r,R)f(R)drdR. \tag{7.6}$$

Here, $f(r)dr$ is the number concentration of cloud droplet within the radius interval of (r, r+dr), ρ_w is the density of liquid water, and r^* is 40 μm.

Eq. (7.6) can be evaluated if $f(r)$ and $K(r, R)$ are appropriately given. To

express $f(r)$ using an analytic function form in bulk microphysics schemes, it is usual to use the gamma function as:

$$f(r) = N_0 r^{\mu} \exp(-\lambda r), \tag{7.7}$$

where N_0, μ, and λ are the intercept, dispersion, and slope parameters of the gamma function, respectively. Because double-moment cloud microphysics scheme can only predict the mass and number concentration, many schemes predict the intercept and slope parameters and set the dispersion parameter as a constant (e.g., Cohard and Pinty 2000; Seifert and Beheng 2001; Milbrandt and Yau 2005; Lim and Hong 2010). Some schemes diagnose the dispersion parameter rather than set it as a constant (e.g., Thompson et al. 2008; Morrison et al. 2009), thereby obtaining more degree of freedom and reality to represent the cloud drop size distribution. In this study, the method proposed by Thompson et al. (2008), which diagnose the dispersion parameter $\mu = \min[\text{nint}(10^9/N_c), 15]$, where N_c is the number concentration of cloud droplet in m^{-3} and nint(x) returns the nearest integer of x, is used.

Therefore, if $K(r, R)$ can be expressed as the polynomial or the gamma function of r and R with a integer dispersion parameter, Eq. (7.6) can be integrated analytically using the incomplete gamma function integration. In this study, the polynomial function form is adopted to represent $K(r, R)$.

To represent $K(r, R)$ with the polynomial function, the terminal velocity v_t and the collection efficiency η should be fitted to the polynomial function. At first, the result of Beard (1976) is used to determine the parameterization of v_t. It is

usual to use $v_t = v_0 r^{\gamma}$ with a real number of γ to parameterize the terminal velocity of liquid water drop in many previous studies. However, the fitted result shows that γ is very close to 2 if r is restricted to be smaller than 40 μm. Therefore, in this study, γ is set to 2 and the resultant $v_0 = 1.09734 \times 10^8$ (v_t in m s^{-1}, r in m) with R^2 of more than 0.99.

The result of Pinsky et al. (2001), which used a particle model to obtain collection efficiency between small drops, is used to determine the parameterization of η. By observing η of Pinsky et al. (2001), a polynomial function is used as follows:

$$\eta = k \frac{r}{R}\left(1-\frac{r}{R}\right)\left(\frac{r}{R}+a\right)\left(R^3+bR^4\right), \tag{7.8}$$

where k, a, and b are the constants to be used to fit Eq. (7.6) to the result of Pinsky et al. (2001). The obtained k, a, and b are 1.3543×10^8, 2.1421×10^{-1}, and -1.1135×10^2 (r and R in m) with R^2 of ~0.8, which is depicted in Fig. 7.1.

Using the parameterized v_t and η, now Eq. (7.8) can be expressed as the polynomial function of r and R. The fitted K in this study and that is obtained in Long (1974) are compared in Fig. 7.2. It is easily seen that the overall distribution of K is close to that of η, in other words, to determine η in an appropriate form is important to obtain more accurate approximation of K. Because the fitted K in this study is much closer to the collection kernel used in the bin microphysics scheme (e.g., Pinsky et al. 2001) that that in previous studies, it may not be necessary to introduce an additional artificial function, such as Seifert and Beheng (2001).

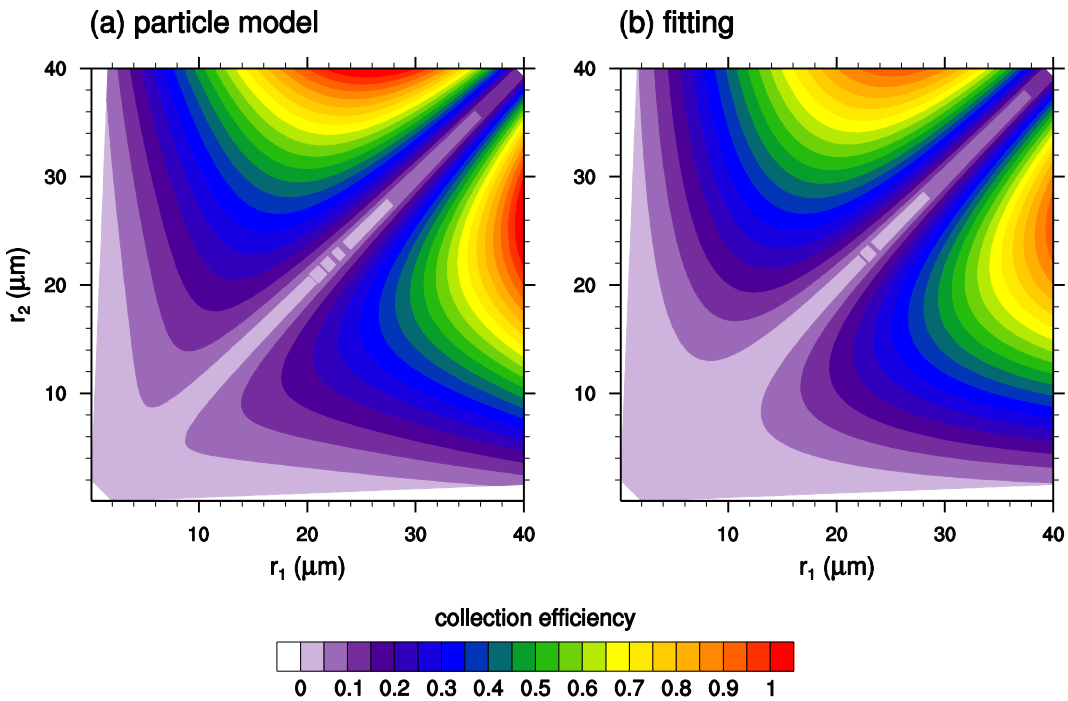

Figure 7.1 Collection efficiency between drops (a) derived from the particle model (Pinsky et al. 2001) and (b) calculated with the fitting function.

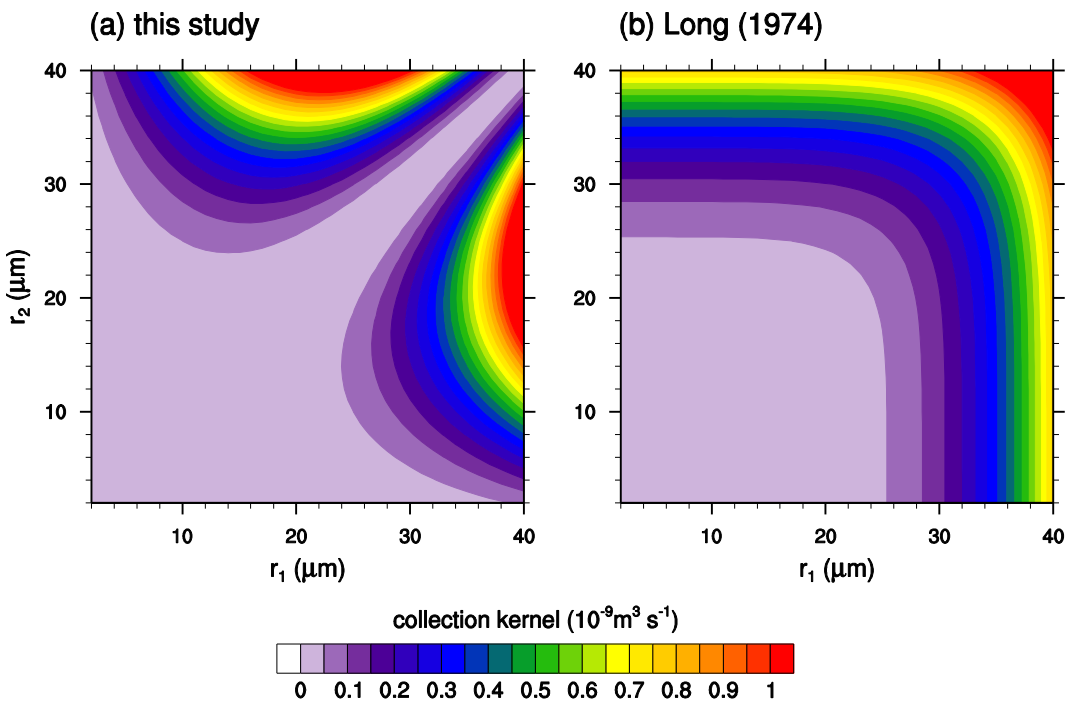

Figure 7.2 Collection kernel between drops (a) calculated in this study and (b) in Long (1974).

The fitted K and $f(r)$ are used to evaluate the autoconversion rate using Eq. (7.6), which yields:

$$\left.\frac{\partial q_r}{\partial t}\right|_{\text{au}} = \rho_w \frac{4}{3}\pi^2 N_0^2 v_0 k\left(m_1 - \alpha m_2\right), \tag{7.9}$$

where

$$m_1 = \sum_{n_1=1}^{10} a_i \frac{(\mu+n_1)!}{\lambda^{\mu+n_1+1}} \left[\begin{array}{l} \left(\dfrac{(\mu+10-n_1)!}{\lambda^{\mu+11-n_1}} \right) - \displaystyle\sum_{n_2=0}^{\mu+n_1} \frac{\lambda^{n_2}}{n_2!} \frac{(\mu+10-n_1+n_2)!}{(2\lambda)^{\mu+11-n_1+n_2}} \\ +b\left(\dfrac{(\mu+11-n_1)!}{\lambda^{\mu+12-n_1}} \right) - \displaystyle\sum_{n_2=0}^{\mu+n_1} \frac{\lambda^{n_2}}{n_2!} \frac{(\mu+11-n_1+n_2)!}{(2\lambda)^{\mu+12-n_1+n_2}} \end{array} \right], \tag{7.10}$$

$$m_2 = \sum_{n_1=1}^{10} a_i \frac{(\mu+n_1)!}{\lambda^{\mu+n_1+1}} \left[\begin{array}{l} \left(\dfrac{(\mu+10-n_1)!}{\lambda^{\mu+11-n_1}} \left(1 - e^{-\lambda r^*} \displaystyle\sum_{n_3=0}^{\mu+10-n_1} \frac{(\lambda r^*)^{n_3}}{n_3!} \right) \right) \\ -\displaystyle\sum_{n_2=0}^{\mu+n_1} \frac{\lambda^{n_2}}{n_2!} \frac{(\mu+10-n_1+n_2)!}{(2\lambda)^{\mu+11-n_1+n_2}} \left(1 - e^{-2\lambda r^*} \displaystyle\sum_{n_3=0}^{\mu+10-n_1+n_2} \frac{(2\lambda r^*)^{n_3}}{n_3!} \right) \\ +b\left(\dfrac{(\mu+11-n_1)!}{\lambda^{\mu+12-n_1}} \left(1 - e^{-\lambda r^*} \displaystyle\sum_{n_3=0}^{\mu+11-n_1} \frac{(\lambda r^*)^{n_3}}{n_3!} \right) \right) \\ -b\displaystyle\sum_{n_2=0}^{\mu+n_1} \frac{\lambda^{n_2}}{n_2!} \frac{(\mu+11-n_1+n_2)!}{(2\lambda)^{\mu+12-n_1+n_2}} \left(1 - e^{-2\lambda r^*} \displaystyle\sum_{n_3=0}^{\mu+11-n_1+n_2} \frac{(2\lambda r^*)^{n_3}}{n_3!} \right) \end{array} \right]. \tag{7.11}$$

Here a_i ($1 \le i \le 10$) is given as (a, 1+a, 1–2a, –2+a, –1+2a, 2–a, –1–2a, –2+a, 1+a, 1). $\partial q_c/\partial t|_{\text{au}}$ is simply given as $-\partial q_r/\partial t|_{\text{au}}$.

The collision between two cloud droplets reduces the number of cloud droplet by two and increases the number of raindrop by one. However, the self-collection of cloud droplets compensates one cloud droplets and there is no change in the number of raindrop. Therefore, the change in cloud droplet number concentration and raindrop number concentration can be evaluated in a very similar way to the change in cloud droplet mass concentration, which is expressed as follows:

$$\left.\frac{\partial N_c}{\partial t}\right|_{\text{au}} = -\pi N_0^2 v_0 k\left(2N_1 - \alpha N_2\right), \tag{7.11}$$

$$\left.\frac{\partial N_r}{\partial t}\right|_{\text{au}} = \pi N_0^2 v_0 k\left(N_1 - \alpha N_2\right), \tag{7.13}$$

where

$$N_1 = \sum_{n_1=1}^{7} a_i' \frac{(\mu+n_1)!}{\lambda^{\mu+n_1+1}} \left[\begin{array}{c} \left(\frac{(\mu+7-n_1)!}{\lambda^{\mu+8-n_1}} \right) - \sum_{n_2=0}^{\mu+n_1} \frac{\lambda^{n_2}}{n_2!} \frac{(\mu+7-n_1+n_2)!}{(2\lambda)^{\mu+8-n_1+n_2}} \\ +b\left(\frac{(\mu+8-n_1)!}{\lambda^{\mu+9-n_1}} \right) - \sum_{n_2=0}^{\mu+n_1} \frac{\lambda^{n_2}}{n_2!} \frac{(\mu+8-n_1+n_2)!}{(2\lambda)^{\mu+9-n_1+n_2}} \end{array} \right], \tag{7.14}$$

$$N_2 = \sum_{n_1=1}^{7} a_i' \frac{(\mu+n_1)!}{\lambda^{\mu+n_1+1}} \left[\begin{array}{l} \left(\frac{(\mu+7-n_1)!}{\lambda^{\mu+8-n_1}} \left(1 - e^{-\lambda r^*} \sum_{n_3=0}^{\mu+7-n_1} \frac{(\lambda r^*)^{n_3}}{n_3!} \right) \right) \\ -\sum_{n_2=0}^{\mu+n_1} \frac{\lambda^{n_2}}{n_2!} \frac{(\mu+7-n_1+n_2)!}{(2\lambda)^{\mu+8-n_1+n_2}} \left(1 - e^{-2\lambda r^*} \sum_{n_3=0}^{\mu+7-n_1+n_2} \frac{(2\lambda r^*)^{n_3}}{n_3!} \right) \\ +b \left(\frac{(\mu+8-n_1)!}{\lambda^{\mu+9-n_1}} \left(1 - e^{-\lambda r^*} \sum_{n_3=0}^{\mu+8-n_1} \frac{(\lambda r^*)^{n_3}}{n_3!} \right) \right) \\ -b \sum_{n_2=0}^{\mu+n_1} \frac{\lambda^{n_2}}{n_2!} \frac{(\mu+8-n_1+n_2)!}{(2\lambda)^{\mu+9-n_1+n_2}} \left(1 - e^{-2\lambda r^*} \sum_{n_3=0}^{\mu+8-n_1+n_2} \frac{(2\lambda r^*)^{n_3}}{n_3!} \right) \end{array} \right]. \quad (7.15)$$

Here a'_i $(1 \le i \le 7)$ is given as $(a, 1+a, 1-2a, -2-2a, -2+a, 1+a, 1)$.

The solution form of the autoconversion parameterization in this study is much more complex than that in previous studies. However, because many parts of the calculation are repeated, the total increase in run time of the microphysics scheme with this developed autoconversion parameterization is no more than 5% compared to other traditional parameterization.

7.2. Turbulence-induced collision enhancement on autoconversion process

The turbulence statistical model developed by Pinsky et al. (2006) is used to consider the turbulence effects on autoconversion process. The model can consider relatively high turbulence intensity compared to the DNS models. The model treats the motion of drops using statistically calculated Lagrangian acceleration and turbulent shears. A detailed description on the model is given in

Pinsky et al. (2006).

The turbulence statistical model use turbulence dissipation rate and Taylor-microscale Reynolds number as turbulence intensity measures. Nine turbulence dissipation rates (from 10 to 2560 cm^2 s^{-3}) and five Taylor-microscale Reynolds numbers (from 3500 to 56000) are considered in this study; therefore, 45 experiments are conducted. The calculated turbulence-induced collision enhancement (TICE) for each given pair of turbulence dissipation rate and Taylor-microscale Reynolds number is depicted in Fig. 7.3. It is noted that because the model can only validated with drops whose radii are less than 20 μm (Pinsky et al. 2006), TICE of cloud droplets whose radii are larger than 20 μm is extrapolated assumed that TICE of cloud droplets whose radii are 40 μm is 1. It is easily seen that TICE depends stronger on turbulence dissipation rate than on Taylor-microscale Reynolds number, which agrees with the results of previous studies.

After the calculation, TICE is multiplied to the collection efficiency of Pinsky et al. (2001). This results in the collection efficiency in a turbulent flow with wide ranges of turbulence dissipation rate and Taylor-microscale Reynolds number. Then the resulted collection efficiency is again fitted to Eq. (7.8), hence acquiring *k*, *a*, and *b* with various turbulence dissipation rates and Taylor-microscale Reynolds numbers, and the obtained *k*, *a*, and *b* are fitted to a specific function by inspection, which results in as:

$$k = k_0 + k_1\left[1 - \exp\left(-\frac{\varepsilon^{k_2}}{k_3\,\mathrm{Re}_\lambda^{k_4}}\right)\right], \tag{7.16}$$

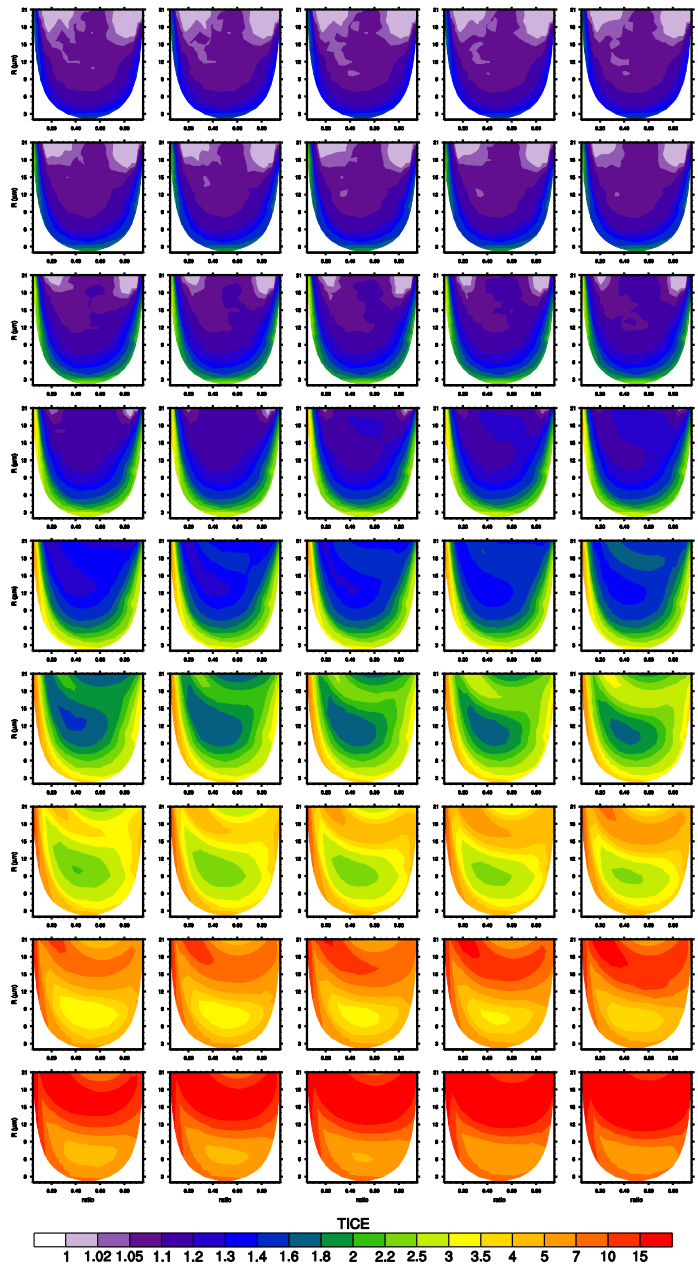

Figure 7.3 TICE calculated using the turbulence statistical model (Pinsky et al. 2006) as a function of turbulence dissipation rate, Taylor-microscale Reynolds number, and drop size.

$$a = a_0 + (a_1 \mathrm{Re}_\lambda + a_2)[\varepsilon - (a_3 \mathrm{Re}_\lambda + a_4)]^2, \tag{7.17}$$

$$b = b_0 + \frac{b_3 + b_4 \mathrm{Re}_\lambda}{b_1 + b_2 \varepsilon}, \tag{7.18}$$

where the coefficients are given in Table 7.1. Figure 7.4 shows the fitting results of *k*, *a*, and *b*. All the fittings show very close to the discretized values, with R^2 of more than 0.99.

7.3. Validation

The developed autoconversion parameterization is validated with a simple box model. In the box, only the mass and number concentration of cloud droplet is predicted, and only the autoconversion process is allowed. Therefore, the mass and number concentration of cloud droplet decreases with time in the box by the autoconversion process.

Time for the mass concentration of cloud droplet to decreases by 90% (t_{10}) is compared to the results of a traditional autoconversion process and a bin microphysics scheme. t_{10} is compared because the autoconversion process is important particularly at the early formation of raindrop (e.g., Onishi et al. 2015). The traditional autoconversion scheme compared in this study is that proposed in Berry and Reinhardt (1974) (hereafter BR74) and used in Cohard and Pinty (2000), Thompson et al. (2008), and Lim and Hong (2010). The bin microphysics scheme consider drops whose radii are less than 40 μm as cloud droplets and solves the stochastic collection equation in the cloud droplet regime using the

Table 7.1 Coefficients as a result of the regression for η given by Eq. (7.8). All coefficients are calculated using the MKS unit.

	$i = 0$	$i = 1$	$i = 2$	$i = 3$	$i = 4$
k_i	1.4091×10^{14}	1.0175×10^{15}	1.4366	1.4843×10^{5}	-2.0119×10^{-1}
a_i	1.9452×10^{-1}	3.3844×10^{-12}	6.6145×10^{-8}	7.0×10^{-3}	-1.7730×10^{2}
b_i	-2.5444×10^{4}	6.4938	2.0370×10^{-2}	9.6914×10^{4}	-1.0×10^{-1}

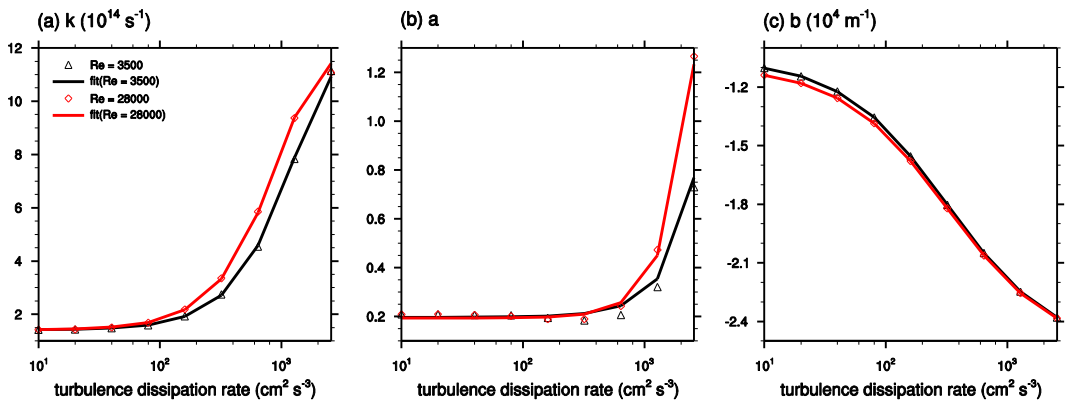

Figure 7.4 Coefficients in Eq. (7.16)–(7.18) calculated using the turbulence statistical model results for Re_λ = 3500 (black triangle) and 28000 (red rectangle). Black and red lines correspond to the fitted coefficients for Re_λ = 3500 and 28000, respectively.

exponential flux method proposed in Bott (2000).

Figure 7.5 shows t_{10} and the cloud droplet number concentration at $t = t_{10}$ with various initial cloud droplet number concentration from 50 cm^{-3} to 1000 cm^{-3}. The initial cloud droplet mass concentration is set to 1 g m^{-3}. The result shows that t_{10} from BR74 is relatively similar to that from the bin microphysics scheme when the initial cloud droplet number concentration is small. However, as the initial cloud droplet number concentration increases, t_{10} from BR74 significantly increases, which means that BR74 significantly underestimates the autoconversion rate compared to the bin microphysics scheme. The cloud droplet number concentration at $t = t_{10}$ is also overestimated in BR74.

The result from the developed autoconversion parameterization shows the considerably improved result, particularly for predicting t_{10}. Although the developed autoconversion parameterization predicts slightly shorter t_{10} and slightly larger cloud droplet number concentration compared to the bin microphysics scheme, the differences to the results of bin microphysics scheme are smaller than the differences between the results of BR74 and the bin microphysics scheme.

7.4. Results

7.4.1. Idealized 2-D cloud case

The developed autoconversion parameterization is implemented to the Thompson microphysics scheme (Thompson and Eidhammer 2014) that is included in the Weather Research and Forecasting (WRF) model v.3.7.1. Using the developed

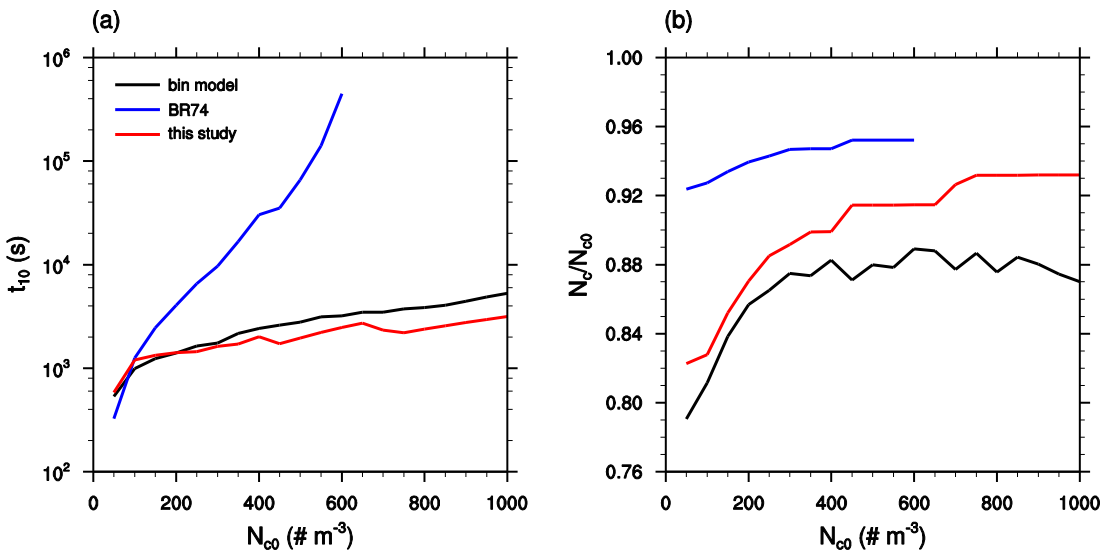

Figure 7.5 (a) t_{10} (time to 10% of the initial cloud water content to become rainwater content) and (b) ratio of the remaining CDNC to the initial CDNC at t = t_{10} as a function of the initial CDNC. The initial cloud water content is 1 g m^{-3}. It is noted that when the initial CDNC > 600 cm^{-3}, it is not possible to convert 10% of the initial cloud water content into rainwater content via the autoconversion process in BR74.

parameterization with the base of Thompson microphysics scheme and the WRF model, an isolated deep convective cloud is numerically simulated under idealized environmental conditions. Thermodynamic sounding of Weisman and Klemp (1982) is used without basic-state wind. The domain is two-dimensional, with horizontal and vertical domain size of 50 km and 18 km, respectively. The grid size is 250 m in the horizontal direction and 125 m in the vertical direction. Uppermost 4 km is set to the sponge layer to prevent the reflection of gravity waves. The experimental conditions are almost the same as those of Section 4.

Figure 7.6 shows the time series of hydrometeor contents and surface precipitation averaged near the domain center. The analysis is concentrated around the domain center because the secondary convection is continuously induced off the domain center due to the compensating downward motion and cold outflow, which is out of interest in this study. At first, the developed autoconversion parameterization does not induce quite large changes in hydrometer contents. It is mainly due to the very high cloud water mixing ratio at and near the cloud core area (larger than 2 g kg^{-1}) and relatively smaller cloud water number concentration (generally smaller than 100 cm^{-3}), which might induces similar or smaller autoconversion rate from the developed autoconversion parameterization than that from BR74 (Fig. 7.5). Cloud water mixing ratio slightly increases in the developed autoconversion parameterization particularly at the early cloud developing stage (t < 20 min). Rainwater mixing ratio decreases at this stage mainly due to the increased cloud water mixing ratio. Increased cloud water mixing ratio provides increased chances for ice crystals to collide with cloud droplets, hence inducing a decrease in ice crystal mixing ratio and an increase in

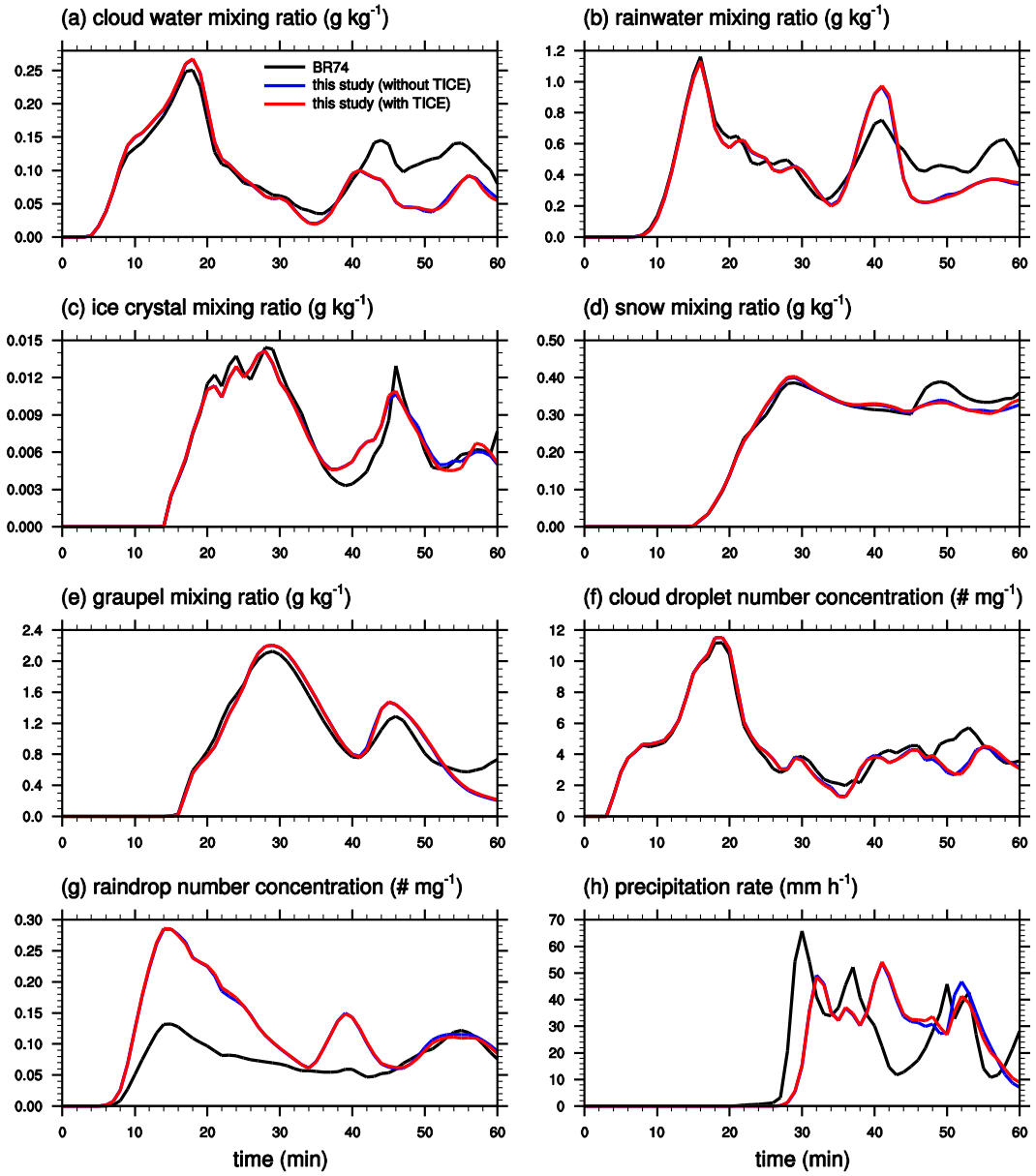

Figure 7.6 Time series of (a) cloud water, (b) rainwater, (c) ice crystal (d) snow, (e) graupel mixing ratio, (f) cloud droplet (g) raindrop number concentration, and (h) surface precipitation rate averaged near the domain center (x = –2.5 km – 2.5 km).

snow mixing ratio.

Although the differences in hydrometer mixing ratio are relatively small, the difference in rainwater number concentration is quite large. The developed autoconversion parameterization produces much larger raindrop number concentration than BR74, which causes a delay and a decrease in surface precipitation. BR74 produces too large cloud droplet number concentration compared to the bin microphysics scheme and to the developed autoconversion parameterization even though t_{10} is similar. This might cause for BR74 to underestimate raindrop number concentration. The effects of TICE are very small in this case. The small effects might be come from the relatively small aerosol concentration dependence on the cloud development in this case; the cloud development is almost unchanged even with 10-fold aerosol number concentration increases.

As in Section 4, the spatial distribution of graupel mass is depicted in Fig. 7.7. In Fig. 7.6g, the time series of graupel mixing ratio averaged over the whole vertical layers shows a small difference. However, the spatial distribution of graupel mass shows a relatively clear difference. With the developed autoconversion parameterization, the graupel mass in the upper layers increases but the graupel mass in the cloud center and in the lower layer decreases. Due to the increased cloud water mixing ratio, ice crystals have more chances to grow snow or graupel via the collision with the cloud droplets. This increases the graupel mass in the upper layer, but the number of graupel particles also increases and the mean size of the graupel particles decreases. Therefore, relatively large graupel mass remains in the upper layer and the graupel mass in the cloud core

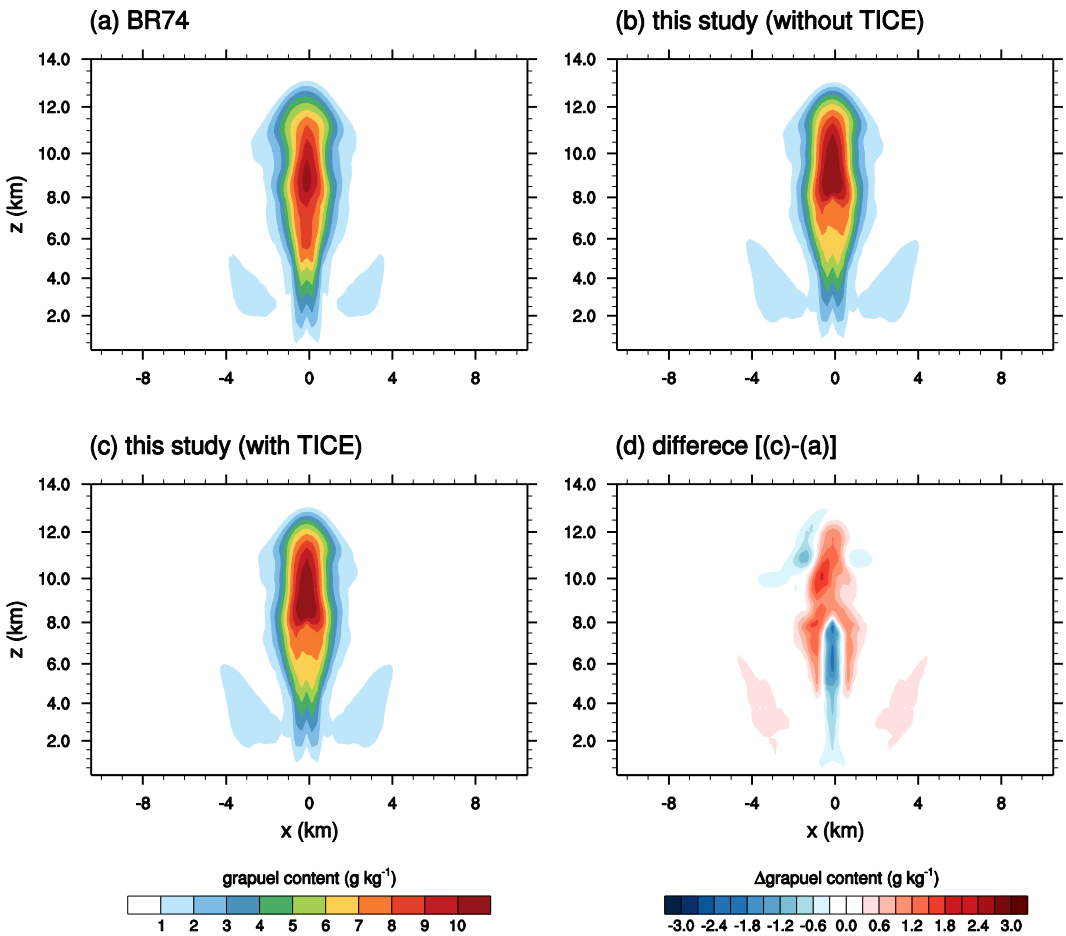

Figure 7.7 Spatial distributions of graupel mass averaged for t = 25 – 35 min using the autoconversion scheme of (a) BR74, (b) this study (without TICE), and (c) this study (with TICE). (d) shows the difference between (c) and (a).

area decreases due to the decrease mean size and mean terminal velocity, which results in the decrease in surface precipitation.

Figure 7.8 shows the time series of autoconversion and accretion rates averaged near the domain center. Autoconversion rate slightly decreases and accretion rate slightly increases with the developed autoconversion parameterization, which is causative of the increase in cloud water mixing ratio at the initial stage (Fig. 7.6a). Because the drop number concentration is generally less than 100 cm^{-3}, particularly at the cloud core, it is expected from Fig. 7.5 that the difference in autoconversion rate is not large. More detailed experiments with various aerosol number concentrations as well as with appropriate cloud microphysics schemes and thermodynamic soundings are needed to clarify the impacts of the developed autoconversion parameterization.

7.4.2. Heavy precipitation case

A heavy precipitation event that occurred on 21 September 2010, which is the same as the case in Section 6, is simulated using the WRF model with the developed autoconversion parameterization. All the experimental setup is the same as in Section 6 but the cloud microphysics scheme used here is Thompson bulk microphysics scheme.

The surface precipitation amount accumulated over the 00–21 LST 21 September 2010 is shown in Fig. 7.9. At first, the accumulated surface precipitation is generally less than the half of the observed precipitation and approximately 60–70% of the simulated surface precipitation using the bin microphysics scheme. In addition, the differences induced by the changes in

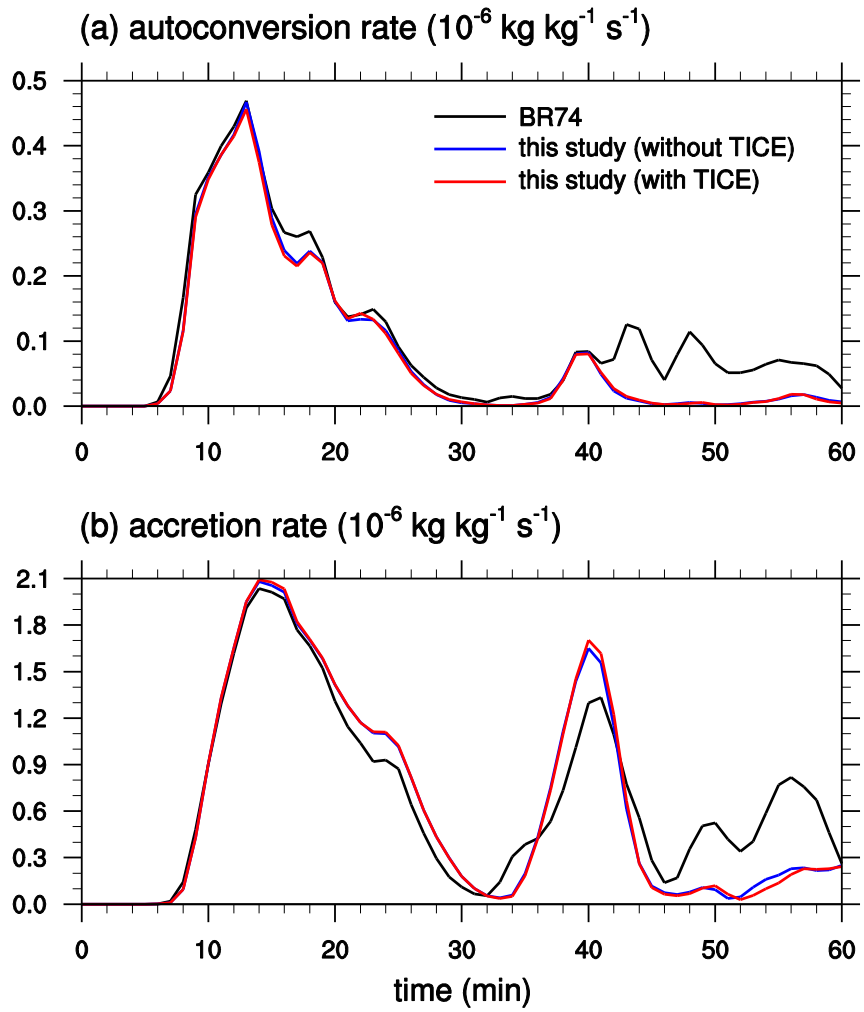

Figure 7.8 Time series of autoconversion rate and accretion rate averaged near the domain center (x = –2.5 km – 2.5 km).

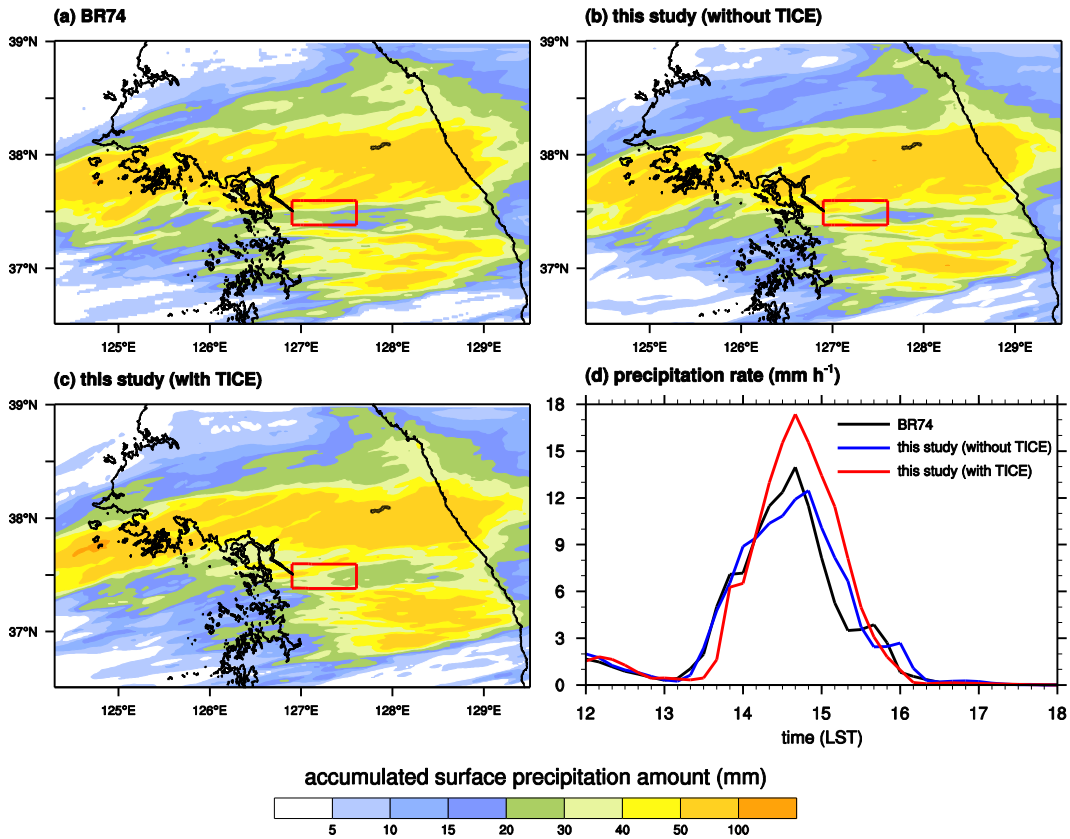

Figure 7.9 Accumulated surface precipitation amount for 00–21 LST 21 September 2010 using the autoconversion parameterization of (a) BR74, (b) this study (without TICE), and (c) this study (with TICE). (d) shows the time series of surface precipitation rate averaged over the rectangle in each figure of (a)–(c).

autoconversion parameterization and TICE are not large. In addition, the surface precipitation averaged over the area of interest (Seoul and its nearby area) is also little changed due to the autoconversion scheme (Fig. 7.9d), mainly due to the large liquid water content but small drop number concentration. However, TICE clearly increases the surface precipitation at that area, which is the same trend as in the experiments with the bin microphysics scheme. To investigate the reason, spatial distribution of relative humidity with respect to ice is examined and seen in Fig. 7.10. In the case with TICE, relative humidity with respect to ice is higher than in the case with BR74 in the lower layer of the front. This large humidity is caused by the early drop coalescence due to TICE that results in a decrease in condensation of drops. The excess vapor is transported upward following the front, and it increases the ice particle mixing ratio, resulting in the increase in surface precipitation.

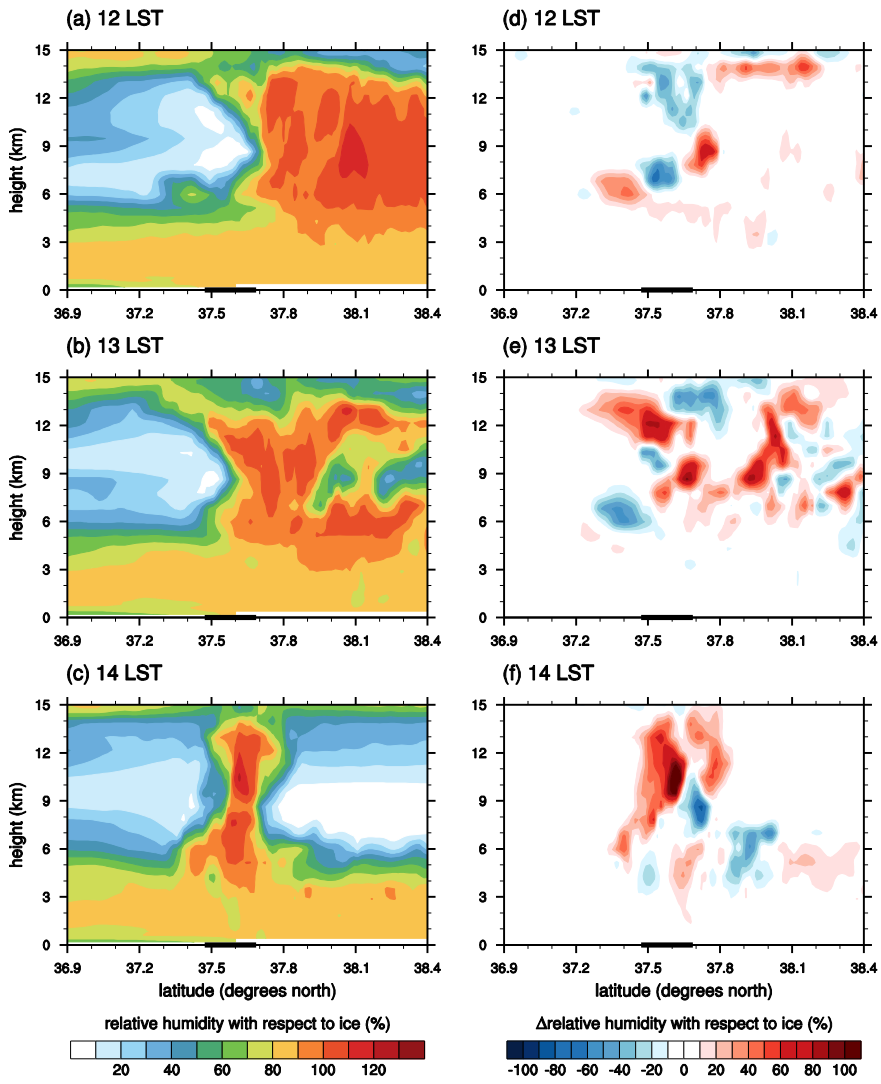

Figure 7.10 Vertical cross sections of relative humidity with respect to ice along the black line in Fig. 7.9 at t = (a) 12 LST, (b) 13 LST, and (c) 14 LST using the autoconversion scheme in this study with TICE. Thick black lines correspond to the box in Fig. 7.9. (d)–(f) are the same as (a)–(c) but for the difference in relative humidity with respect to ice to the results using the BR74 autoconversion parameterization.

8. Summary and Conclusions

This study investigated the effects of turbulence on warm clouds and the resulting precipitation. Numerical experiments were conducted using various aerosol concentrations with a 2-D dynamic model that incorporates bin microphysics. The cloud model takes turbulence-induced collision enhancement (TICE) into consideration. The Taylor microscale Reynolds number and the turbulent dissipation rate, which are used to determine TICE, are calculated using the turbulent kinetic energy (TKE) that is predicted in the model.

In all simulations, TICE enhances coalescence between small droplets, which accelerates the onset of surface precipitation and reduces the liquid water path during the early stage of cloud development. This effect is larger for high cloud condensation nuclei (CCN) concentrations because it is less likely for small droplets to grow into large drops under high CCN concentrations without the assistance of TICE. The cloud microstructure, such as the drop effective radius and cloud drop number concentration, are also affected by TICE. Although TICE is expected to increase the mean effective radius and decrease the mean cloud drop number concentration via enhanced coalescence, such results are found only for high CCN concentrations. This result is because the growth of droplets via vapor diffusion is sufficiently vigorous in low CCN concentration and high humidity environments to allow the droplets to grow to sizes at which they can coalesce efficiently. Therefore, the effect of TICE on the amount of surface precipitation depends on the CCN concentration. For high CCN concentrations,

TICE substantially increases the amount of surface precipitation, because TICE enhances the coalescence of cloud droplets into raindrops. However, for low CCN concentrations, TICE slightly decreases the amount of surface precipitation because the early coalescence of small droplets due to TICE decreases the total condensation. These results are summarized in a schematic diagram in Fig. 8.1.

The effects of TICE on mixed-phase deep convective clouds were investigated using a 2-D bin microphysics cloud model. This study considered TICE for drop-drop collisions and drop-graupel collisions. Two types of basic-state winds and two aerosol concentrations were considered to examine the effects of TICE with different basic-state winds and aerosol concentrations.

In the cases that consider TICE, graupel particles with small sizes occupy some portion of the total graupel mass in the cloud core area. On the other hand, in the cases that do not consider TICE, graupel particles with large sizes occupy almost all the total graupel mass. TICE accelerates the growth of ice crystals in the high altitudes into small graupel particles. Graupel particles with small sizes have slower terminal velocities than those with large sizes. Thus, graupel particles in the high altitudes are distributed across a wider area, and the downward flux of graupel mass decreases when TICE is considered. The increased sublimation of ice particles by TICE also decreases the amount of surface precipitation, despite its limited role. The effects of TICE in the sheared basic-state wind cases are comparatively small. This is because strong wind shear diminishes cloud development in the early stage, so the number of ice crystals, which is the key to the difference by TICE, decreases significantly.

The effects of TICE on various properties of precipitating warm clouds

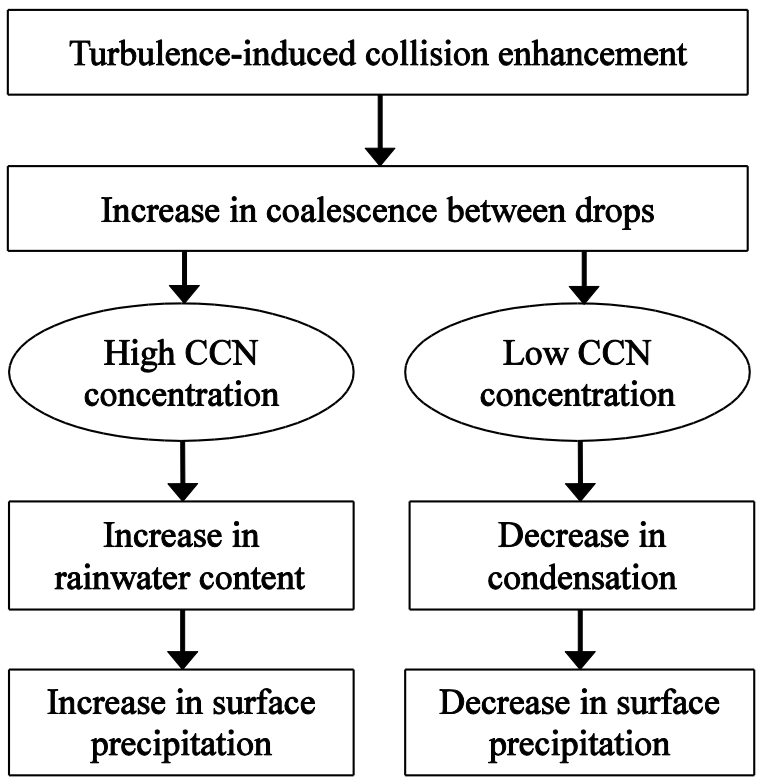

Figure 8.1 Schematic diagram that shows the different effects of TICE on the amount of surface precipitation for high and low CCN concentrations.

were numerically investigated using a community mesoscale model coupled with a bin microphysics scheme. A series of large-eddy simulations with a wide range of aerosol concentrations were conducted using a horizontal grid size of 100 m.

This study shows that the rainwater path increases due to TICE, although the liquid water path remains at a similar level. As in previous studies, TICE induces earlier and stronger surface precipitation. The stronger surface precipitation is not merely due to the increased rainwater amount but also due to the increased raindrop terminal velocity. The increase in surface precipitation becomes more enhanced as the aerosol concentration increases. The drop size distributions at certain selected levels showed that TICE tends to decrease the number of small droplets and induce another peak position in large drop radius, while a decrease in aerosol concentration tends to increase the peak position in small droplet radius toward the larger ones.

The increased mean drop radius due to TICE results in a decreased sum of the drop radii and, hence, a decrease in evaporation. This decrease in evaporation in turn increases the cloud fraction because most of the evaporation occurs near the cloud edges. Moreover, the averaged vertical velocity and variance of vertical velocity decrease due to TICE mainly because the reduced evaporative cooling in the cloud layer induces more stable atmosphere. The decrease in the variance of vertical velocity induces a decrease in TKE despite an increase in buoyancy. Therefore, the effects of TICE produce a negative feedback. The cloud top height is little affected by TICE, despite the increased buoyancy. However, as in the previous studies, because the differences in cloud top height, TKE, and other properties related to TKE induced by TICE are comparatively small in this study,

more careful approaches are needed.

The cloud albedo averaged over the clouds clearly decreases due to TICE. This is caused by the increase in mean drop radius and the resultant decrease in the sum of the drop cross section. However, the cloud albedo averaged over the entire domain is little affected due to TICE because the decrease in cloud albedo averaged over the clouds is largely cancelled out by the increase in cloud fraction.

It has been known that complex interactions among aerosols, clouds, and precipitation are important in understanding the development of shallow warm clouds. Particularly, aerosol-induced changes in precipitation are known to affect the evolution of cloud structures. It seems that turbulence-induced changes in precipitation have relatively small effects on the changes in cloud structure, mainly because large changes in precipitation due to TICE are observed when the precipitation amount is too small and only small changes in precipitation due to TICE are observed when the precipitation amount is moderate.

Overall, the effects of turbulence are clearly observed in precipitation, and the effects tend to be larger as the aerosol concentration increases. However, the effects are not great in other quantities and seem to be smaller than those from the ten-fold changes in aerosol number concentration. These relatively small changes are partially due to offsetting or negative feedback among numerous processes that affect the cloud properties in various ways. However, these changes certainly depend on various environmental conditions. In addition, the turbulence-induced entrainment/detrainment around the cloud edges remains poorly understood. More careful approaches are required to investigate the effects of turbulence more distinctly.

Using the community mesoscale model coupled with the updated bin microphysics scheme, the heavy precipitation event that occurred on 21 September 2010 over the Korean Peninsula was numerically simulated and the effects of turbulence-induced collision enhancement (TICE) on the precipitation event were investigated. This heavy precipitation event was driven by the convergence of two different high pressure systems and the formation of a convergence zone with large moisture. The numerical simulations captured well the important features of the observed surface precipitation and radar reflectivity as well as the synoptic conditions.

In the case with TICE, surface precipitation amount increases, particularly in the areas that the heavy precipitation event starts and that the heaviest precipitation is concentrated, being closer to the observation than in the case without TICE. Radar reflectivity shows the higher frequency of high radar reflectivity near the surface in the case with TICE. TICE accelerates the coalescence between small droplets, which induces a decrease in condensation and an increase in water vapor transported upward following the front. This causes an increase in relative humidity with respect to ice in high altitudes, hence strengthening the depositional growth of ice crystal and snow particles. Therefore, the snow mass in the clouds increases due to TICE and this increase results in the increase in surface precipitation amount. Although rimed fraction is reduced by TICE because of the decreased supercooled drops aloft, the total increase amount of ice mass by riming is enhanced due to TICE because of the increased ice mass due to the depositional growth. Snow size distribution shows that TICE little changes peak snow radius but the snow number concentration increases in almost

the entire radius range.

A new autoconversion parameterization is derived based on the analytic integration and the collection efficiencies obtained by a particle model and a turbulence statistical model. The solution is much more complex than those in traditional autoconversion parameterizations. However, the increase in total calculation time is insignificant; hence the efficiency of bulk microphysics scheme is not vitiated.

The box model results show that the traditional autoconversion parameterization significantly underestimates the autoconversion rate particularly with small cloud droplet content and large cloud droplet number concentration. In addition, the traditional autoconversion parameterization always predicts too small decrease in cloud droplet number concentration. The developed autoconversion parameterization improves the calculation accuracy of the process considerably, both for the time to convert cloud droplet to raindrop and the number concentration of cloud droplet.

The developed autoconversion parameterization is implemented into the Thompson microphysics scheme and the WRF model and examined with an idealized deep convective cloud case and a real heavy precipitation case. In the idealized deep convective cloud case, while the averaged hydrometer mixing ratio is little affected, the number concentration of raindrops is much larger with the developed autoconversion parameterization than that with the traditional autoconversion parameterization, which causes a delay of the surface precipitation onset and a decrease in surface precipitation amount. The effects of turbulence are very small in this case, mainly due to the characteristics of this cloud system

and/or the used cloud microphysics scheme that is insensitive to the aerosol number concentration.

In the real heavy precipitation case, the effects of developed autoconversion parameterization are limited. However, turbulence clearly increases the surface precipitation at the particular area of interest. This is because the turbulence accelerates the coalescence of small droplets and this accelerated growth of droplets decreases the condensation. More water vapor induced by this decrease in condensation is transported upward and increases the ice particle mixing ratio, hence increasing surface precipitation via melting.

REFERENCES

Albrecht, B.A., 1989: Aerosols, cloud microphysics, and fractional cloudiness. *Science,* **245**, 1227–1230.

Arabas, S., and S.-I. Shima, 2013: Large eddy simulations of trade-wind cumuli using particle-based microphysics with Monte-Carlo coalescence. *J. Atmos. Sci.*, **70**, 2768–2777.

Arakawa, A., 1966: Computational design for long-term numerical integration of the equations of fluid motion: Two-dimensional incompressible flow. *J. Comp. Phys.*, **1**, 119–143.

Arenberg D., 1939: Turbulence as a major factor in the growth of cloud droplets. *Bull. Am. Meteorol. Soc.*, **20**, 444–445.

Ayala, O., B. Rosa, and L.-P. Wang, 2008: Effects of turbulence on the geometric collision rate of sedimenting droplets. Part II: Theory and parameterization. *New J. Phys.*, **10**, 075016.

Baker, B., Q. Mo, R. Lawson, D. O'Connor, and A. Korolev, 2009: Drop size distributions and the lack of small drops in RICO rain shafts. *J. Appl. Meteorol. Climatol.*, **48**, 616–623.

Beard, K. V., 1976: Terminal velocity and shape of cloud and precipitation drops aloft. *J. Atmos. Sci.*, **33**, 851–864.

Benmoshe, N., M. Pinsky, A. Pokrovsky, and A. Khain, 2012: Turbulent effects on the microphysics and initiation of warm rain in deep convective clouds: 2-D simulations by a spectral mixed-phase microphysics cloud model. *J.*

Geophys. Res., **117**, D06220.

Benmoshe, N., and A. P. Khain, 2014: The effects of turbulence on the microphysics of mixed-phase deep convective clouds investigated with a 2-D cloud model with spectral bin microphysics. *J. Geophys. Res. Atmos.*, **119**, 207–221.

Berry, E. X., and R. L. Reinhardt, 1974: An analysis of cloud drop growth by collection: Part II. Single initial distributions. *J. Atmos. Sci.*, **31**, 1825–1831.

Bott, A., 2000: A flux method for the numerical solution of the stochastic collection equation: Extension to two-dimensional particle distributions. *J. Atmos. Sci.*, **57**, 284–294.

Brenguier, J.-L., T. Bourrianne, A. Coelho, J. Isbert, R. Peytavi, D. Trevarin, and P. Weschler, 1998: Improvements of droplet size distribution measurements with the Fast-FSSP (forward scattering spectrometer probe). *J. Atmos. Ocean. Technol.*, **15**, 1077–1090.

Carrió, G. G., and W. R. Cotton, 2011: Urban growth and aerosol effects on convection over Houston. Part II: Dependence of aerosol effects on instability. *Atmos. Res.*, **102**, 167–174.

Carrió, G. G., W. R. Cotton, and W. Y. Y. Cheng, 2010: Urban growth and aerosol effects on convection over Houston. Part I: the August 2000 case. *Atmos. Res.*, **96**, 560–574.

Chen, F., and J. Dudhia, 2001: Coupling an advanced land-surface/ hydrology model with the Penn State/ NCAR MM5 modeling system. Part I: Model description and implementation. *Mon. Wea. Rev.*, **129**, 569–585.

Cohard, J.-M., and J.-P. Pinty, 2000: A comprehensive two-moment warm microphysical bulk scheme. I: Description and test. *Q. J. R. Meteorol. Soc.*, **126**, 1815–1842.

Devenish, B. J., P. Bartello, J. L. Brenguier, L. R. Collins, W. W. Grabowski, R. H. A. IJzermans, S. P. Malinowski, M. W. Reeks, J. C. Vassilicos, L.-P. Wang, and Z. Warhaft, 2012: Droplet growth in warm turbulent clouds. *Q. J. R. Meteorol. Soc.*, **138**, 1401–1429.

Dudhia, J., 1989: Numerical study of convection observed during the winter monsoon experiment using a mesoscale two-dimensional model. *J. Atmos. Sci.*, **46**, 3077–3107.

Fan, J., T. Yuan, J. M. Comstock, S. Ghan, A. Khain, L. R. Leung, Z. Li, V. J. Martins, and M. Ovchinnikov, 2009: Dominant role by vertical wind shear in regulating aerosol effects on deep convective clouds. *J. Geophys. Res.*, **114**, D22206.

Feingold, G., I. Koren, H. Wang, H. Xue, and Wm. A. Brewer, 2010: Precipitation-generated oscillations in open cellular cloud fields. *Nature*, **466**, 849–852.

Franklin, C. N., 2008: A warm rain microphysics parameterization that includes the effect of turbulence. *J. Atmos. Sci.* **65**, 1795–1816.

Franklin, C. N., 2014: The effects of turbulent collision-coalescence on precipitation formation and precipitation-dynamical feedbacks in simulations of stratocumulus and shallow cumulus convection. *Atmos. Chem, Phys.*, **14**, 6557–6570.

Franklin, C. N., P. A. Vaillancourt, M. K. Yau, and P. Bartello, 2005: Collision

rates of cloud droplets in turbulent flows. *J. Atmos. Sci.*, **62**, 2451–2466.

Frisch, U., 1995: *Turbulence*. Cambridge University Press, 258 pp.

Gerber, H. E., G. M. Frick, J. B. Jensen, and J. G. Hudson, 2008: Entrainment, mixing, and microphysics in trade-wind cumulus. *J. Meteorol. Soc. Jpn.*, **86A**, 87–106.

Givati, A., and D. Rosenfeld, 2004: Quantifying precipitation suppression due to air pollution. *J. Appl. Meteorol.*, **43**, 1038–1056.

Grabowski, W. W., and L.-P. Wang, 2013: Growth of cloud droplets in a turbulent environment. *Annu. Rev. Fluid Mech.*, **45**, 293–324.

Grabowski, W. W., L.-P. Wang, and T. V. Prabha, 2015: Macroscopic impacts of cloud and precipitation processes on maritime shallow convection as simulated by a large eddy simulation model with bin microphysics. *Atmos. Chem. Phys.*, **15**, 913–926.

Han, J.-Y., J.-J. Baik, and A. P. Khain, 2012: A numerical study of urban aerosol impacts on clouds and precipitation. *J. Atmos. Sci.*, **69**, 504–520.

Hill, R. J., 2002: Scaling of acceleration in locally isotropic turbulence. *J. Fluid Mech.*, **452**, 361–370.

Iguchi, T., and Coauthors, 2014: WRF–SBM simulations of melting-layer structure in mixed-phase precipitation events observed during LPVEx. *J. Appl. Meteor. Climatol.*, **53**, 2710–2731.

Janjic, Z. I., 2002: *Nonsingular implementation of the Mellor–Yamada level 2.5 scheme in the NCEP meso model*. NCEP Office Note, No. 437, NCEP.

Jonas, P. R., 1996: Turbulence and cloud microphysics. *Atmos. Res.*, **40**, 283–306.

Jung, W., and T.-Y. Lee, 2013: Formation and evolution of mesoscale convective

systems that brought the heavy rainfall over Seoul on September 21, 2010. *Asia-Pacific J. Atmos. Sci.*, **49**, 635–647.

Kain, J. S., 2004: The Kain-Fritsch convective parameterization: An update. *J. Appl. Meteor.*, **43**, 170–181.

Khain, A. P., 2009: Note on state-of-the-art investigations of aerosol effects on precipitation: A critical review. *Environ. Res. Lett.*, **4**, 015004.

Khain, A. P., and I. Sednev, 1996: Simulation of precipitation formation in the Eastern Mediterranean coastal zone using a spectral microphysics cloud ensemble model. *Atmos. Res.*, **43**, 77–110.

Khain, A. P., M. Ovtchinnikov, M. Pinsky, A. Pokrovsky, and H. Krugliak, 2000: Notes on the state-of-the-art numerical modeling of cloud microphysics. *Atmos. Res.*, **55**, 159–224.

Khain, A. P., A. Pokrovsky, M. Pinsky, A. Seifert, and V. Phillips, 2004: Simulation of effects of atmospheric aerosols on deep turbulent convective clouds using a spectral microphysics mixed-phase cumulus cloud model. Part I: Model description and possible applications. *J. Atmos. Sci.*, **61**, 2963–2982.

Khain, A. P., M. Pinsky, T. Elperin, N. Kleeorin, I. Rogachevskii, and A. Kostinski, 2007: Critical comments to results of investigations of drop collisions in turbulent clouds. *Atmos. Res.*, **86**, 1–20.

Khain, A. P., N. BenMoshe, and A. Pokrovsky, 2008: Factors determining the impact of aerosols on surface precipitation from clouds: An attempt at classification. *J. Atmos. Sci.*, **65**, 1721–1748.

Khain, A., D. Rosenfeld, A. Pokrovsky, U. Blahak, and A. Ryzhkov, 2011: The

role of CCN in precipitation and hail in a mid-latitude storm as seen in simulations using a spectral (bin) microphysics model in a 2D dynamic frame. *Atmos. Res.*, **99**, 129–146.

Khain, A. P., T. V. Prabha, N. Benmoshe, G. Pandithurai, and M. Ovchinnikov, 2013: The mechanism of first raindrops formation in deep convective clouds. *J. Geophys. Res. Atmos.*, **118**, 9123–9140.

Koren, I., and G. Feingold, 2011: Aerosol-cloud-precipitation system as a predator-prey problem. *Proc. Natl. Acad. Sci. USA*, **108**, 12227–12232.

Korolev, A., M. Pinsky, and A. Khain. 2013: A new mechanism of droplet size distribution broadening during diffusional growth. *J. Atmos. Sci.*, **70**, 2051–2071.

Kunnen, R. P. J., C. Siewert, M. Meinke, W. Schröder, and K. D. Beheng, 2013: Numerically determined geometric collision kernels in spatially evolving isotropic turbulence relevant for droplets in clouds. *Atmos. Res.*, **127**, 8–21.

Köhler, H., 1936: The nucleus in and the growth of hygroscopic droplets. *Trans. Faraday Soc.*, **32**, 1152–1161.

Lakshmana, R. V., S. S. V. S. R. Krishna, and K. P. R. V. Murty, 2012: A comprehensive study of aerosols around Visakhapatnam, a coastal region, India. *Ecol. Environ. Conserv.*, **18**, 53–59.

Lanotte, A. S., A. Seminara, and F. Toschi, 2009: Cloud droplet growth by condensation in homogeneous isotropic turbulence. *J. Atmos. Sci.*, **66**, 1685–1697.

La Porta, A., G. A. Voth, A. M. Crawford, J. Alexander, and E. Bodenschatz, 2001: Fluid particle accelerations in fully developed turbulence. *Nature*, **409**,

1017–1019.

Lee. J., Y. Noh, S. Raasch, T. Riechelmann, and L.-P. Wang, 2014: Investigation of droplet dynamics in a convective cloud using a Lagrangian cloud model. *Meteorol. Atmos. Phys.*, **124**, 1–21.

Lee, S. S., and G. Feingold, 2013: Aerosol effects on the cloud-field properties of tropical convective clouds. *Atmos. Chem. Phys.*, **13**, 6713–6726.

Lee, S. S., L. J. Donner, and J. E. Penner, 2010: Thunderstorm and stratocumulus: how does their contrasting morphology affect their interactions with aerosols? *Atmos. Chem. Phys.*, **10**, 6819–6837.

Lim, K.-S. S., and S.-Y. Hong, 2010: Development of an effective double-moment cloud microphysics scheme with prognostic cloud condensation nuclei (CCN) for weather and climate models. *Mon. Wea. Rev.*, **138**, 1587–1612.

Long, A. B., 1974: Solutions to the droplet collection equation for polynomial kernels. *J. Atmos. Sci.*, **31**, 1040–1052.

Meyer, M. P., P. J. DeMott, and W. R. Cotton, 1992: New primary ice-nucleation parameterizations in an explicit cloud model. *J. Appl. Meteorol.*, **31**, 708–721.

Milbrandt, J. A., and M. K. Yau, 2005: A multimoment bulk microphysics parameterization. Part II: A proposed three-moment closure and scheme description. *J. Atmos. Sci.*, **62**, 3065–3081.

Monin, A. S., and A. M. Yaglom, 1975: *Statistical fluid mechanics: Mechanics of turbulence*. 2nd ed., MIT Press.

Morrison, H., G. Thompson, and V. Tatarskii, 2009: Impact of cloud microphysics on the development of trailing stratiform precipitation in a simulated

squall line: Comparison of one- and two-moment schemes. *Mon. Wea. Rev.*, **137**, 991–1007.

Mlawer, E. J., S. J. Taubman, P. D. Brown, M. J. Iacono, and S. A. Clough, 1997: Radiative transfer for inhomogeneous atmosphere: RRTM, a validated correlated-k model for the longwave. *J. Geophys. Res.*, **102**, 16663–16682.

Ogura, Y., and T. Takahashi, 1973: The development of warm rain in a cumulus cloud. *J. Atmos. Sci.*, **30**, 262–277.

Onishi, R., K. Matsuda, and K. Takahashi, 2015: Lagrangian tracking simulation of droplet growth in turbulence–Turbulence enhancement of autoconversion rate. *J. Atmos. Sci.*, **72**, 2591–2607.

Phillips, V. T. J., A. Pokrovsky, and A. Khain, 2007: The influence of time-dependent melting on the dynamics and precipitation production in maritime and continental storm clouds. *J. Atmos. Sci.*, **64**, 338–359.

Pinsky, M. B., and A. P. Khain, 1998: Some effects of cloud turbulence on water–ice and ice–ice collisions. *Atmos. Res.*, **47–48**, 69–86.

Pinsky, M., A. Khain, D. Rosenfeld, and A. Pokrovsky, 1998: Comparison of collision velocity differences of drops and graupel particles in a very turbulent cloud. *Atmos. Res.*, **49**, 99–113.

Pinsky, M. A. Khain, and M. Shapiro, 2001: Collision efficiency of drops in a wide range of Reynolds number: Effects of pressure on spectrum evolution. *J. Atmos. Sci.*, **58**, 742–764.

Pinsky, M. M. Shapiro, A. Khain, and H. Wirzberger, 2004: A statistical model of strains in homogeneous and isopropic turbulence. *Phys. D*, **191**, 297–313.

Pinsky M. B., A. P. Khain, B. Grits, and M. Shapiro, 2006: Collisions of small

drops in a turbulent flow. Part III: Relative droplet fluxes and swept volumes. *J. Atmos. Sci.*, **63**, 2123–2139.

Pinsky, M., A. P. Khain, and H. Krugliak, 2008: Collisions of cloud droplets in a turbulent flow. Part V: Application of detailed tables of turbulent collision rate enhancement to simulation of droplet spectra evolution. *J. Atmos. Sci.*, **65**, 357–374.

Pope, B., 2000: *Turbulent flows*. Cambridge Univ. Press, 771 pp.

Pruppacher, H. R., and J. D. Klett, 1997: *Microphysics of clouds and precipitation*, 2nd ed. Kluwer Academic Publishers, 954pp.

Reuter, G. W., R. De Villiers, and Y. Yavin, 1988: The collection kernel for two falling cloud drops subjected to random perturbations in a turbulent air flow: A stochastic model. *J. Atmos. Sci.*, 45, 765–773

Riechelmann, T., Y. Noh, and S. Raasch, 2012: A new method for large-eddy simulations of clouds with Lagrangian droplets including the effects of turbulent collision. *New J. Phys.*, **14**, 065008.

Rosenfeld, D., 1999: TRMM observed first direct evidence of smoke from forest fires inhibiting rainfall. *Geophys. Res. Lett.*, **26**, 3105–3108.

Ryu, Y.-H., J.-J. Baik, and S.-H. Lee, 2011: A new single-layer urban canopy model for use in mesoscale atmospheric models. *J. Appl. Meteorol. Climatol.*, **50**, 1773–1794.

Saffman, P. G., and J. S. Turner, 1956: On the collision of drops in turbulent clouds. *J. Fluid Mech.*, **1**, 16–30.

Seifert, A., and K. Beheng, 2001: A double-moment parameterization for simulating autoconversion, accretion, and selfcollection. *Atmos. Res.*, **59–**

60, 265–281.

Seifert, A., and K. Beheng, 2006: A two-moment cloud microphysics parameterization for mixed-phase clouds. Part II: Maritime vs. continental deep convective storms. *Meteorol. Atmos. Phys.*, **92**, 67–82.

Seifert, A., L. Nuijens, and B. Stevens, 2010: Turbulence effects on warm-rain autoconversion in precipitating shallow convection. *Q. J. R. Meteorol. Soc.*, **136**, 1753–1762.

Shaw, R. A., 2003: Particle-turbulence interactions in atmospheric clouds. *Annu. Rev. Fluid Mech.*, **35**, 183–227.

Siebert, H., K. Lehmann, and M. Wendisch, 2006: Observations of small-scale turbulence and energy dissipation rates in the cloudy boundary layer. *J. Atmos. Sci.*, **61**, 1451–1466.

Siebert, H., R. A. Shaw, and Z. Warhaft, 2010: Statistics of small-scale velocity fluctuations and internal intermittency in marine stratocumulus clouds. *J. Atmos. Sci.*, **67**, 262–273.

Skamarock, W. C., J. B. Klemp, J. Dudhia, D. O. Gill, D. M. Barker, M. G. Duda, X.-Y. Huang, W. Wang, and J. G. Powers, 2008: *A description of the advanced research WRF version 3*. NCAR Technical Note, NCAR/TN–475+STR, NCAR.

Stoelinga, M. T., 2005: Simulated equivalent reflectivity factor as currently formulated in RIP: Description and possible improvements. Accessed on 4 Jan 2015. [Available online at http://www.atmos.washington.edu/~stoelin-g/RIP_sim_ref.pdf.]

Takahashi, T., T. Endoh, and G. Wakahama, 1991: Vapor diffusional growth of

free falling snow crystals between –3℃ and –23℃. *J. Meteorol. Soc. Jpn*, **69**, 15–30.

Thompson, G., and T. Eidhammer, 2014: A study of aerosol impacts on clouds and precipitation development in a large winter cyclone. *J. Atmos. Sci.*, **71**, 3636–3658.

Thompson, G., P. R. Field, R. M. Rasmussen, and W. D. Hall, 2008: Explicit forecasts of winter precipitation using an improved bulk microphysics scheme. Part II: Implementation of a new snow parameterization. *Mon. Wea. Rev.*, **136**, 5095–5115.

Twomey, S., 1959: The nuclei of natural cloud formation. Part II: The supersaturation in natural clouds and the variation of cloud droplet concentration. *Pure Appl. Geophys.* **43**, 243–249.

Vaillancourt, P. A., M. K. Yau, P. Bartello, and W. W. Grabowski, 2002: Microscopic approach to cloud droplet growth by condensation. Part II: Turbulence, clustering, and condensational growth. *J. Atmos. Sci.*, **59**, 3421–3435.

vanZanten, M.C., B. Stevens, L. Nuijens, A. P. Siebesma, A. S. Ackerman, F. Burnet, A. Cheng, F. Couvreux, H. Jiang, M. Khairoutdinov, Y. Kogan, D. C. Lewellen, D. Mechem, K. Nakamura, A. Noda, B. J. Shipway, J. Slawinska, S. Wang, and A. Wyszogrodzki, 2011: Controls on precipitation and cloudiness in simulations of trade-wind cumulus as observed during RICO. *J. Adv. Model. Earth Syst.* **3**, M06001.

Wang, H., and G. Feingold, 2009: Modeling mesoscale cellular structures and drizzle in marine stratocumulus. Part I: Impact of drizzle on the formation

and evolution of open cells. *J. Atmos. Sci.*, **66**, 3237–3256.

Weisman, M. L., and J. B. Klemp, 1982: The dependence of numerically simulated convective storms on vertical wind shear and buoyancy. *Mon. Wea. Rev.*, **110**, 504–520.

Wyszogrodzki, A. A., W. W. Grabowski, L.-P. Wang, and O. Ayala, 2013: Turbulent collision-coalescence in maritime shallow convection. *Atmos. Chem. Phys.*, **13**, 8471–8487.

Xue, H., and G. Feingold, 2006: Large-eddy simulations of trade wind cumuli: Investigation of aerosol indirect effects. *J. Atmos. Sci.*, **63**, 1605–1622.

Xue, H., G. Feingold, and B. Stevens, 2008: Aerosol effects on clouds, precipitation, and the organization of shallow cumulus convection. *J. Atmos. Sci.*, **65**, 392–406.

Zhang, Y., B. Stevens, and M. Ghil, 2005: On the diurnal cycle and susceptibility to aerosol concentration in a stratocumulus-topped mixed layer. *Q. J. R. Meteorol. Soc.*, **131**, 1567–1583.

Zhou, Y., A. S. Wexler, and L.-P. Wang, 2001: Modelling turbulent collision of bidisperse inertial particles. *J. Fluid Mech.*, **433**, 77–104.

초 록

최근 수십 년 동안의 연구를 통해 구름 내에 존재하는 난류가 구름과 강수의 발달, 특히 구름 입자들 사이의 충돌에 상당한 영향을 끼침이 알려졌다. 2차원 상세 구름 미세물리 모형을 이용하여 구름 응결핵(CCN) 수농도를 바꾸어가며 난류가 유도하는 충돌 향상(TICE)이 온난 구름과 강수에 미치는 효과를 조사하였다. TICE는 테일러 마이크로 규모의 레이놀즈 수와 난류 소실률에 따라 결정된다. 이 연구에 사용된 열역학적 탐측 자료는 착모역전층이 존재하는 온난하고 습윤한 대기 조건으로 온난 구름을 모의하기에 적절하다. 모든 CCN 수농도에서 TICE에 의해 구름 발달 초기의 액체수 경로가 감소하였고 지표 강수가 일찍 출현하였다. 그러나 TICE에 의한 우수 경로와 지표 강수량의 변화는 CCN 수농도에 따라 다르게 나타났다. CCN 수농도가 높을 때에는 TICE에 의해 평균 구름 물방울 수농도(CDNC)가 감소하고 평균 유효 반지름이 증가하였는데, 이러한 변화는 지표 강수량의 증가를 야기하였다. 그러나 CCN 수농도가 낮을 때에는 TICE에 의한 평균 CDNC와 평균 유효 반지름의 변화가 작았고 지표 강수량은 조금 감소하였다. 가속된 물방울 사이의 병합에 의한 응결량의 감소로 지표 강수량의 감소를 설명할 수 있었다. 또한 CCN 수농도가 증가함에 따라 지표 강수량이 증가하는 구간이 있었는데, TICE는 이러한 CCN 수농도와 지표 강수량 사이의 관계에 영향을 끼쳤다. 이 관계는 대기의 상대습도에 따라 크게 좌우되었다.

TICE가 깊은 대류 혼합 구름에 미치는 영향을 물방울–물방울, 물방울–얼음 충돌에 대한 TICE가 고려된 2차원 상세 구름 미세물리 모형을 이용하고 두 종류의 기본 바람 배경류와 두 종류의 에어로졸 농도를 고려하여 수치적으로 조사하였다. 모든 모의 결과에서 싸락눈 입자가 구름 질량에서 가장 큰 부분을 차지하였다. 균일한 배경류 사례에서는 TICE가 반영되었을 때에는 중간 크기의 싸락눈 입자가 전체 싸락눈 질량의 일정 부분을 차지하였으나 TICE가 반영되지 않았을 때에는 큰 크기의 싸락눈 입자가 전체 싸락눈 질량의 상당 부분을 차지하였다. 이것은 TICE에 의해 얼음 결정이 작은 싸락눈으로 보다

빨리 성장하였기 때문이다. 이러한 난류에 의한 싸락눈 입자의 크기 분포 변화는 질량 평균된 싸락눈 입자의 종단 속도의 감소를 불러 일으켰다. 따라서 TICE에 의해 싸락눈 질량의 하강 플럭스와 싸락눈 입자의 용융이 감소하였고 이로 인해 지표 강수량이 감소하였다. 또한 에어로졸 수농도가 낮을 때에는 TICE에 의해 얼음 입자의 승화도 증가하였는데 이 또한 지표 강수량의 감소에 일정 부분 기여하였다. 시어가 있는 배경류의 경우에서는 균일한 배경류의 경우에 비해 TICE 효과가 두드러지게 나타나지 않았는데 이는 얼음 결정의 수가 균일한 배경류의 경우보다 훨씬 감소하여 TICE가 반영된 경우와 그렇지 않은 경우에서 싸락눈 입자의 크기 분포가 크게 달라지지 않았기 때문이다.

상세 구름 미세물리 모형이 결합된 Weather Research and Forecasting(WRF) 모형의 큰 에디 모사(LES) 버전을 이용하여 강수를 유발하는 온난 구름에서의 지표 강수, 구름 비율, 구름의 광학 두께, 구름의 반사도와 같은 구름의 성질에 TICE 효과가 미치는 영향을 조사하였다. 선행 연구에서와 마찬가지로 물방울 간의 충돌 향상으로 인해 평균 물방울 크기가 증가하였고 이로 인해 지표 강수의 시작이 앞당겨지고 지표 강수량이 증가하였다. 초기에 단봉분포였던 물방울 크기 분포는 TICE에 의해 쌍봉분포가 되고, 이는 물방울의 단봉분포에서 극값의 위치를 이동시키는 에어로졸에 의한 효과와는 달랐다. 물방울 크기가 증가함에 따라 증발이 감소하여 이로 인해 구름이 차지하는 면적이 증가하였다. 또한 감소한 증발 냉각으로 인해 대기가 보다 안정화되면서 연직 운동의 평균과 변동이 감소하였고, 이러한 감소는 시어에 의한 난류 운동 에너지(TKE)의 생성을 감소시켜 TKE의 감소를 야기하였다. TICE에 의한 TKE의 감소는 비록 그 변화 정도가 일반적으로 작았지만 음되먹임으로 해석될 수 있다. 평균 물방울 크기의 증가는 구름의 황학 두께와 구름 영역에서 평균된 구름 반사도의 감소를 야기하였다. 하지만 이는 증가한 구름이 차지한 면적과 서로 상쇄되어 계산 영역에서 평균된 구름 반사도는 거의 변화가 없었다. 난류에 의해 유도된 강수량의 변화는 구름의 구조에 상대적으로 작은 영향을 끼쳤는데, 이는 지표 강수량의 차이가 적거나, 지표 강수량이 적어서였다.

TICE가 2010년 9월 21일 한반도 중부 지역에 발생한 집중호우에 미치는 영향을 상세 구름 미세물리 모형이 결합된 WRF 모형을 이용하여 조사하였다. 수치 실험은 종관 대기 조건뿐 아니라 관측된 지표 강수와 레이더 반사도의 중요한 특징을 잘 모의하였다.

TICE에 의해 한반도 중부 지역에서 평균된 지표 강수량은 증가하였는데, 특히 서울과 그 주변 지역에서의 최대 강수율은 TICE에 의해 약 35%까지 증가하였다. TICE에 의해 지표 부근에서 강한 레이더 반사도의 출현 비율 역시 증가하였다. TICE는 작은 구름 물방울 사이의 충돌을 가속시키는데, 이로 인해 응결이 감소하여 전선을 따라 상층으로 수송되는 수증기의 양이 증가하였다. 이는 상층에서 얼음에 대한 상대습도 증가를 야기하였고 이로 인해 얼음 결정과 눈송이의 수증기 침착에 의한 성장도 증가하였다. 따라서 TICE에 의해 눈송이의 질량이 증가하였고 이러한 증가는 지표 강수량의 증가를 불러 일으켰다. TICE에 의해 부유하는 작은 구름 물방울이 감소하여 눈송이의 결착률은 감소하였지만, TICE에 의해 유도되는 얼음 입자의 수증기 침착에 의한 성장이 증가하여 전체 결착량은 증가하였다. 눈송이 크기 분포에서의 극값의 위치는 거의 변하지 않은 대신 눈송이의 수농도는 거의 모든 눈송이 크기 범위에서 증가하였다.

해석적 적분과 입자 모형, 난류 통계 모형을 이용하여 계산한 충돌 효율에 기반하여 TICE를 고려하는 새로운 자동변환 과정 모수화를 개발하였다. 상자 모형 결과는 개발된 자동변환 모수화가 구름 물방울이 빗방울로 전환되는데 걸리는 시간과 구름 물방울의 수농도 예측에 대한 계산 과정의 정확도를 이전의 자동변환 모수화 과정에 비해 상당히 향상시켰음을 보여 주었다. 개발된 자동변환 모수화를 WRF 모형과 Thompson 미세물리 모형에 결합하여 이상화된 깊은 대류 구름의 사례와 집중호우 사례를 조사하였다. 이상화된 깊은 대류 구름 사례에 개발된 자동변환 모수화를 이용할 경우 기존에 사용된 자동변환 모수화 과정에 비해 훨씬 많은 빗방울 수농도가 예측되었고 이로 인해 지표 강수 출현의 지연과 지표 강수량의 감소가 야기되었다. 집중호우 사례에 대한 수치 실험에서 개발된 자동변환 모수화의 영향은 제한적이었다. 하지만 TICE에 의해 관심 지역에서의 지표 강수량이 뚜렷이 증가하였고 이는 TICE에 의해 작은 물방울의 병합이 가속되어 응결이 감소하였기 때문이다. 이러한 응결의 감소로 인해 더 많은 수증기가 상층으로 수송되고, 이로 인해 얼음 입자의 혼합비가 증가하여 용융에 의한 지표 강수량이 증가하였다.

주요어: 구름 미세물리, 난류 효과, 상세 구름 미세물리 모형, 구름, 강수, 자동변환 과정

학번: 2011-30119